Experimental Investigation of Plasma-Electrode Interactions on the ZaP-HD Flow Z-Pinch Device

Amierul Aqil bin Khairi

A dissertation
submitted in partial fulfillment of the
requirements for the degree of

Doctor of Philosophy

University of Washington

2025

Reading Committee:

Uri Shumlak, Chair

Eric Meier

Justin Little

Program Authorized to Offer Degree:
Aeronautics & Astronautics

University of Washington

Abstract

Experimental Investigation of Plasma-Electrode Interactions on the ZaP-HD Flow Z-Pinch Device

Amierul Aqil bin Khairi

Chair of the Supervisory Committee:
Professor Uri Shumlak
Aeronautics & Astronautics

The electrodes of sheared-flow-stabilized (SFS) Z-pinch devices directly face the core plasma and supply the pinch current. The high temperature, high density plasma environment produces intense particle and heat fluxes, leading to concerns of electrode erosion that limit durability and contaminate the plasma. An improved understanding of these plasma-electrode interactions is required, especially at the high temperatures and current densities required for fusion applications. An experimental investigation is conducted on the ZaP-HD SFS Z-pinch device, which produces plasma temperatures up to 1 keV, densities of 10^{23} m^{-3}, and drives pinch currents up to 150 kA. In-situ measurements of the gross carbon erosion flux from the graphite electrode are obtained with S/XB spectroscopy. The measured fluxes exceed the theoretical values from physical sputtering, but are comparable with the expected sublimation flux. An analysis of the ionization mean free paths of neutrals produced by both erosion processes indicates that ionization of sublimated carbon occurs within the electrode sheath, while sputtered neutrals are ionized outside of the sheath. This suggests significant redeposition of sublimated carbon, leading to a process of carbon recycling. The sputtered carbon is therefore primarily responsible for the net erosion. Initial

measurements of the electrode surface temperature with a two-color pyrometer are also presented. Ex-situ analysis of electrode material is enabled by the design of a removable coupon. Three different plasma exposure cases were tested that involved varying the pinch current and the particle fluence to the electrode. Net mass loss measurements imply net erosion fluxes far smaller than indicated by spectroscopic measurements of total erosion, which supports the theory of high redeposition rates. Erosion rates range from 0.01 to 0.1 mg/C, which are comparable to existing arc discharge devices. Measurements of the microscopic surface morphology and roughness indicate substantial material rearrangement and general smoothing except at high plasma exposure conditions. The granular matrix of graphite is mostly replaced by larger consolidated structures that reduce the number of visible voids. Crack formation is apparent, possibly due to thermal cycling, which suggests the importance of surface heating and possible phase change of graphite. Definitive features of sputtering such as pitting and cratering are absent, and further study is needed to attribute the observed morphology to other physical processes. Overall, these results indicate some alignment with erosion and recycling processes in high-current arc discharges, which have successfully operated with solid electrodes in extreme environments. Further investigation into these similarities may yield useful understanding that can be applied to the management of erosion on SFS Z-pinch electrodes.

TABLE OF CONTENTS

LIST OF FIGURES

ACKNOWLEDGMENTS

I have many to thank for their support in this long journey. First and foremost, I thank my adviser, Professor Uri Shumlak, who has placed his trust and support in me ever since I joined his group as a fledgling undergraduate researcher. It has been an honor and a privilege to learn from him, and I wish to highlight his dedication to teaching that is delivered with patience, kindness, and humor. I also thank Dr. Brian Nelson, Dr. Raymond Golingo, Dr. Yue Zhang, and Dr. Tobin Weber, who guided many of my first steps in the lab. Special recognition goes to Dzung Tran, Eliot George, Sean Krewson, and Colin Baxter for their guidance and expertise in the ways of machining.

I have been fortunate to work with many wonderful students in the ZaP Lab. Thank you to my good friends Dr. Eleanor Forbes and Dr. Elliot Claveau, who were my first mentors, and who I continue to look up to in many ways. I thank the many graduate students who have toiled with me on ZaP-HD, and have helped me in countless instances: Timothy Lloyd, Bennett Diamond, Zhangsheng Lian, Aria Johansen, Harry Furey-Soper, Shane Murray, Jared Smythe, and Jeff Peachman. I also thank the undergraduates that have supported my research; they taught me just as much as I have taught them.

Last but not least, I am blessed to have the support of my friends and family. Whether in my communities in Seattle, Kuala Lumpur, or Saigon, their love and encouragement know no bounds of distance or time.

DEDICATION

To my mother, whose strength and sacrifices will always be remembered, and to my youngest brother, who will always be in our hearts.

Chapter 1
INTRODUCTION

Plasmas are the most abundant form of ordinary matter in the universe, comprising the stars and the vast interstellar and intergalactic medium. However, at the modest temperatures and densities of everyday human life, we generally observe matter in its solid, liquid, or gaseous phase. Sustaining artificial plasmas must therefore occur at specific conditions within some type of vessel, which involves contact with solid walls or the solid electrodes that supply the plasma current. In fact, these plasma-material interactions (PMI) are at the foundation of our modern world. For example, the late 19th century saw the first wide-scale use of electrical lighting in the form of carbon arc lamps such as the Yablochkov candle [6] in Europe and Brush lights [7] in North America. The arc sustained by the ionization of eroded atoms from two solid carbon rods produced a bright, if somewhat precarious, light source. Contemporary fluorescent lighting involves PMI as well; low-pressure gas discharge tubes sustain ultraviolet emission from mercury that then interacts with a phosphor coating to produce visible light. Furthermore, an impressive array of plasma processing techniques [8] have enabled highly controlled material surface modification, revolutionizing the manufacture of products in many industries, though perhaps most consequentially in semiconductors. Modern digital systems and computational advancements owe much to the fundamental understanding of PMI.

The influential role of PMI persists at the cusp of several future technological

advancements. Carbon nanotubes [9], touted for their exceptional electrical and mechanical properties, are among various nanomaterials that may be synthesized in the cathode deposits of carbon arc discharges [10]. Carbon erosion and redeposition form part of a self-organized system that affects the quality and yield of nanomaterial synthesis, which are important parameters for scaling to industrial production. In aerospace applications, electrodes and other solid components in plasma-based thrusters are subject to long durations of intense plasma exposure [11, 12]. Thruster lifetime and performance are critically linked to the erosion damage sustained by these components.

Back on Earth, amid the looming crisis of climate change and the urgent need for low-carbon energy sources, there has been a resurgence in nuclear fusion energy research. No longer exclusively the domain of public research institutions and governments, an array of aspiring private companies are exploring a diverse set of approaches to commercialize fusion energy. The revival of the Z pinch as a leading concept in this nascent industry is a result of foundational work at the University of Washington on sheared-flow-stabilization [13, 14, 15, 16, 1], leading to the incorporation of Zap Energy and its mission to develop the concept for commercial fusion [17]. However, critical challenges still remain on the path to commercialization, not least among them the problem of PMI. The sheared-flow-stabilized (SFS) Z-pinch configuration places a solid electrode in direct contact with a fusion-grade plasma, therefore exposing it to extreme particle and heat fluxes. The electrode must also supply several hundred kiloamperes of current to sustain and compress the Z pinch to these high energy density conditions. The resulting plasma-electrode interactions are not fully understood, especially at the high current densities and heat fluxes necessary for a Z-pinch fusion power plant, where their importance is expected to increase [18]. In particular, electrode erosion limits the component lifetime and operational capacity

of the device, which are critical factors in the development of a fusion power plant [19]. This motivates an investigation into the physical processes that govern electrode erosion, which will inform the design of more robust electrodes and the optimization of operational parameters to improve electrode durability.

This dissertation is structured as follows: the remainder of Chapter 1 introduces the SFS Z-pinch configuration. In Chapter 2, relevant theory for plasma-material interactions is presented in the context of magnetic fusion devices, along with a discussion of existing experimental testbeds. In Chapter 3, the ZaP-HD device, diagnostic suite, electrode coupons, and experimental parameters for the investigation are presented. The methodology and results for spectroscopic measurements of erosion are presented in Chapter 4. Initial pyrometry measurements of the surface temperature are reported in Chapter 5. Based on these measurements, a physical picture for electrode erosion is presented in Chapter 6, which describes recycling of carbon at the electrode surface. Ex-situ analysis of the graphite electrode coupons is presented in Chapter 7, including mass-loss measurements, net erosion rates, and changes in surface morphology and topography. Finally, a summary and discussion of the implications for operating solid electrodes in fusion devices is provided in Chapter 8, along with suggestions for future work in Chapter 9.

These findings represent the first experimental investigation of plasma-electrode interactions on the SFS Z pinch, combining in-situ and ex-situ measurements to provide insight into the underlying physical processes for electrode erosion. Ultimately, this work will inform the design and operation of durable solid electrodes in magnetic fusion devices, supporting the development of a nuclear fusion power plant based on the SFS Z pinch.

1.1 Z-Pinch History

Not long after the work of Oliphant and Rutherford [20] at the Cavendish Laboratory produced the first artificial nuclear fusion reactions in 1933, and buoyed by Eddington's earlier speculation that fusion powered the stars [21], interest in harnessing fusion energy for electricity production led to the development of the toroidal Z pinch in 1946 [22]. The pinch effect had been observed through the compression of a copper tube acting as a lightning conductor [23], demonstrating the radially inward force arising from the interaction of an axial current and its self-generated azimuthal magnetic field. This pinch force could be used to confine a column of plasma on axis and away from the device walls. Without the need for external magnets, the Z pinch was simple, compact, and relatively inexpensive to build and operate. Furthermore, bending the Z pinch into a torus solved the issue of plasma streaming out through the ends of a linear device. Despite this initial promise, it was found that strong instabilities quickly disrupted the plasma and stymied efforts to reach high temperatures in devices such as ZETA [24] and the Perhapsatron [25]. By the 1960s, the invalidation of thermonuclear neutron production on ZETA, and the achievements of the T-3 tokamak [26] marked the eventual decline in enthusiasm for the Z pinch. Research on the Z pinch continued in the ensuing decades as an X-ray and neutron source [27], but magnetic confinement fusion research the world over has since been dominated by the tokamak.

1.2 Z-Pinch Equilibrium

In the Z pinch, radial equilibrium is achieved through the balance of the radial pressure gradient and the Lorentz force due to the axial current density j_z and azimuthal magnetic field B_θ, expressed as

$$\frac{dp}{dr} = -j_z B_\theta. \tag{1.1}$$

The full statement of equilibrium is given as

$$\frac{d}{dr}\left(n_i k_B T_i + n_e k_B T_e\right) = -\frac{B_\theta}{\mu_0 r}\frac{d}{dr}\left(r B_\theta\right), \tag{1.2}$$

where n_i and n_e are the ion and electron number densities, and T_i and T_e are the ion and electron temperatures. Integration of this equilibrium over the plasma volume gives the Bennett relation [28], which describes the increase of temperature with the pinch current I:

$$(1+Z)N_i k_B \langle T\rangle = \frac{\mu_0 I^2}{8\pi}. \tag{1.3}$$

In Equation 1.3, Z is the ionization state, N_i is the linear ion number density, k_B is the Boltzmann constant, and $\langle T\rangle$ is the average temperature assuming thermal equilibrium between ions and electrons. For an adiabatically compressed Z-pinch plasma, and using the "sharp pinch" model [29] for an equilibrium with uniform density, scaling relations [16, 1, 18] for the temperature, density, and pinch radius are derived as

$$\frac{T_2}{T_1} = \left(\frac{I_2}{I_1}\right)^2 \frac{N_1}{N_2}, \tag{1.4}$$

$$\frac{n_2}{n_1} = \left(\frac{I_2}{I_1}\right)^{\frac{2}{\gamma-1}} \left(\frac{N_1}{N_2}\right)^{\frac{1}{\gamma-1}}, \tag{1.5}$$

$$\frac{a_2}{a_1} = \left(\frac{I_1}{I_2}\right)^{\frac{1}{\gamma-1}} \left(\frac{N_2}{N_1}\right)^{\frac{\gamma}{2(\gamma-1)}}. \tag{1.6}$$

In the above expressions, N is the linear number density defined as

$$N = \int_0^a 2\pi n(r) r dr, \tag{1.7}$$

for the pinch radius a. Figure 1.1 illustrates the scaling of a 150 kA, 2×10^{23} m^{-3}, 1 keV, 3 mm radius Z pinch based on these scaling relations. These starting parameters are obtained from Ref. [1] for the ZaP-HD device, and are indicated with circles. These relations describe how increasing the pinch current leads to increased plasma

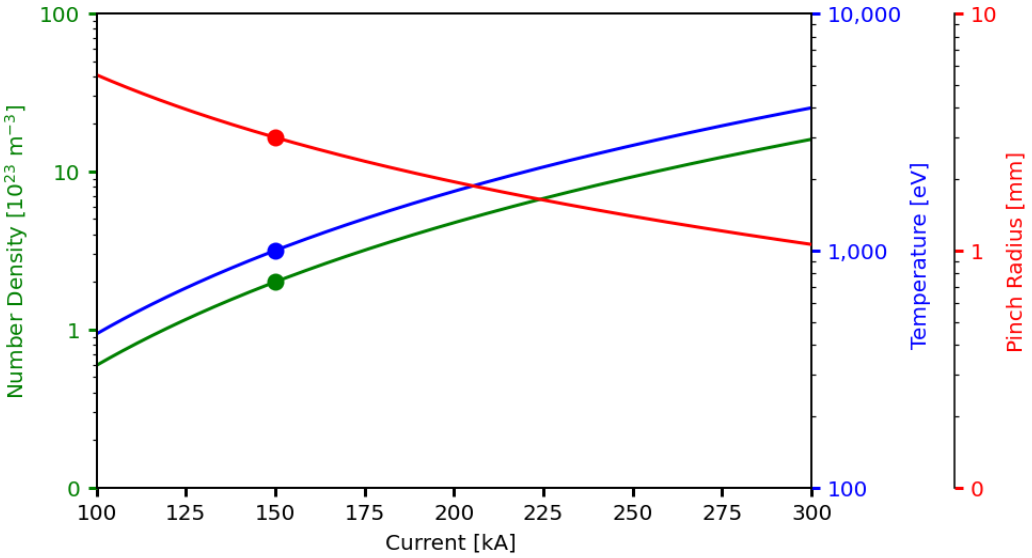

Figure 1.1: Applying the scaling relations in Sec. 1.2 to a 150 kA, 2×10^{23} m^{-3}, 1 keV, 3 mm radius Z pinch illustrates that increasing the pinch current leads to increased plasma parameters and a smaller pinch radius. These Z-pinch parameters are obtained from Ref. [1] for the ZaP-HD device. The circles indicate the starting parameters.

density and temperature and a smaller pinch radius, and therefore high plasma performance in a compact device.

Another advantage of the Z pinch is its efficient plasma confinement, quantified by having an average unity beta. Here, β is defined as the ratio of the volume averaged plasma pressure $\langle p \rangle$ to the magnetic pressure due to the azimuthal field B_θ taken at the radius of a distant outer conducting wall r_w:

$$\langle \beta \rangle \equiv \frac{\langle p \rangle}{B_\theta^2(r_w)/(2\mu_0)} = 1. \tag{1.8}$$

Because the self-generated magnetic field provides radial equilibrium, no external magnetic field coils are necessary in a Z pinch. The complexity, cost, and volume of electromagnetic coils and their associated cooling, shielding, and control systems can therefore be avoided in a Z-pinch fusion device.

1.3 Sheared-Flow Stabilization

Instabilities are a result of the growth of perturbations from the equilibrium in Eq. 1.2. The constriction and bending observed in Z-pinch plasmas are known as the $m = 0$ "sausage" and $m = 1$ "kink" modes respectively, depicted in Fig. 1.2. The $m = 0$ mode is a radial constriction of the plasma column. Initially, a slight perturbation causes a local decrease in the radius. The magnetic field at the location of the constriction must increase due to the constant current flowing through the reduced cross-section, and by its inverse relationship with radius r: $B_\theta \propto 1/r$. This results in a larger pinch force, further constricting the plasma until eventually the plasma current is disrupted. The $m = 1$ instability results from an initial perturbation that bends the plasma column, shown in the right hand side of Fig. 1.2. In this case, the instability grows due to increases in the field strength on the inside of the bend.

Several methods of stabilizing the Z pinch have been established, albeit with certain concessions in terms of their implementation. Shafranov [30] suggested an axial

field applied by external magnets. In a linear Z pinch, this is an open field line which leads to loss of confinement, and the addition of external magnets negates the advantages of an exclusively self-generated magnetic field. Controlling the radial pressure profile stabilizes the $m = 0$ mode [31], but in doing so places an artificial limit on the plasma performance. A close-fitting conducting wall [32] can mitigate instabilities, but the enhanced PMI and melting of the solid material quickly become intractable. The path to a fusion power plant based on the Z pinch relies on mitigating these instabilities, therefore allowing the pinch to exist long enough for thermonuclear fusion conditions to arise from the scaling described in Sec. 1.2. Alternatively, the application of a radial shear in the axial flow velocity has been shown to mitigate $m = 1$ instabilities for a prescribed pressure profile that is already stable against the $m = 0$ mode [33]. The equilibrium described in Eq. 1.2 is unaffected by radial variation of axial flow. Numerical stability analysis [33] indicates that the necessary radial shear is described by

$$\frac{dv_z}{dr} \geq 0.1kV_A, \tag{1.9}$$

where $\frac{dv_z}{dr}$ is the radial velocity gradient, k is the wave number, and V_A is the Alfvén speed defined by the maximum field strength B_0 and mass density ρ_0:

$$V_A = \frac{B_0}{\sqrt{\mu_0 \rho_0}}. \tag{1.10}$$

The presence of sheared velocity layers interrupts the growth of perturbations. At the inside of a kink in the plasma, faster flowing plasma fills in the displaced volume, while the plasma displaced to the outside of a kink enters a region of faster flow, spreading out the perturbation. The overall effect is a decoherence of the instability mode which prevents its growth.

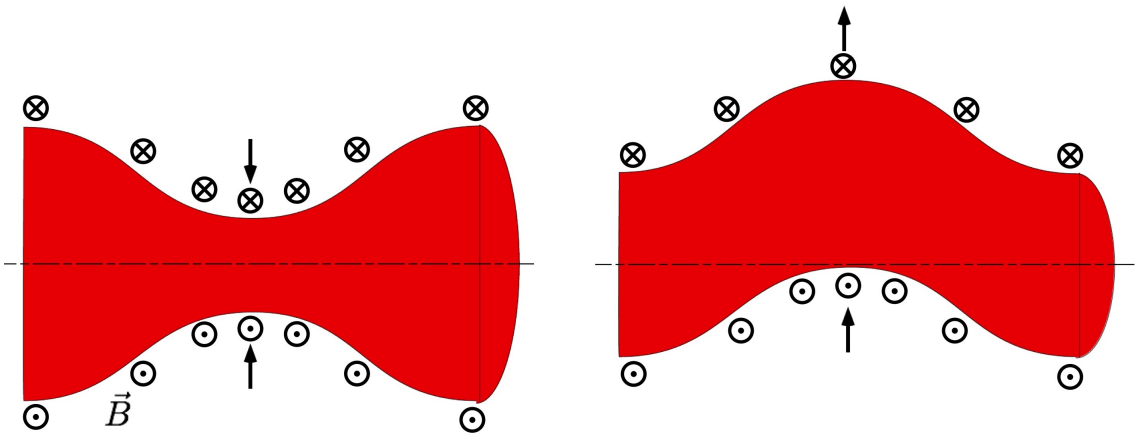

Figure 1.2: Two prevalent MHD instability modes in the Z pinch are the $m = 0$ "sausage" and $m = 1$ "kink" modes, shown on the left and right respectively. The $m = 0$ mode is a constriction of the plasma volume. At the smaller radius of the constriction, a larger magnetic field causes an increased pinching force that further constricts the plasma until eventually the current is disrupted. The relative field strengths at the constriction and adjacent axial locations is given by the density of field notation in the schematic. The $m = 1$ mode is a bending of the plasma volume that causes an increased field strength at the inside of the bend relative to the outside. This results in a net force that exacerbates the bending until disruption of the pinch current occurs.

1.4 The Flow Z-Pinch Experiments

The first SFS Z-pinch experiment at the University of Washington was the ZaP device, which sustained pinches for thousands of Alfvén wave propagation times [13]. The sheared flow was achieved with a coaxial electrode design that coupled a plasma accelerator with a downstream pinch assembly region. The ZaP-HD (High Density) experiment incorporated a third coaxial electrode. Two separate power supplies enabled decoupling of plasma acceleration and Z-pinch compression processes, allowing a larger pinch current to be driven. This enabled investigation of sheared flow stabilization at increased plasma parameters, and resulted in electron temperatures up to 1 keV and electron densities of 10^{23} m^{-3}, over a quiescent period of approximately 50 μs [1]. This motivated the investigation into the fusion performance of the concept with the Fusion Z-pinch Experiment (FuZE), which operated with deuterium and hydrogen mixtures at up to 200 kA of pinch current [34]. Evidence of neutron production concurrent with periods of pinch stability and elevated plasma parameters was obtained [35] and confirmed to be thermonuclear in nature [36]. FuZE continues to be operated by Zap Energy at increased pinch currents of up to 500 kA [17]. The latest SFS Z-pinch device is FuZE-Q, fully designed and built by Zap Energy. The objective of FuZE-Q is to demonstrate performance consistent with net fusion gain, or $Q = 1$ [17].

Chapter 2

PLASMA-MATERIAL INTERACTIONS IN MAGNETIC FUSION DEVICES

In magnetic fusion devices, contact between the solid components and the plasma is an inevitable feature of all confinement schemes. Consequently, the material surfaces exposed to a fusion plasma face extreme bombardment by both particle and heat fluxes. Many different types of particles exist in a fusion plasma. In most cases, hydrogenic ions are present either as fuel or fusion products, as shown in the following expressions for deuterium-deuterium (D-D) and deuterium-tritium (D-T) reactions:

$$\mathrm{D} + \mathrm{D} \rightarrow {}^{3}\mathrm{He}\ (0.82\ \mathrm{MeV}) + \mathrm{n}\ (2.45\ \mathrm{MeV}) \tag{2.1}$$

$$\mathrm{D} + \mathrm{D} \rightarrow \mathrm{T}\ (1.01\ \mathrm{MeV}) + \mathrm{p}\ (3.02\ \mathrm{MeV}) \tag{2.2}$$

$$\mathrm{D} + \mathrm{T} \rightarrow {}^{4}\mathrm{He}\ (3.52\ \mathrm{MeV}) + \mathrm{n}\ (14.1\ \mathrm{MeV}) \tag{2.3}$$

In many devices, protium (^{1}H) is often used in place of deuterium where a non-nuclear environment is desired. As evident in the above reactions, helium isotopes and neutrons are also produced and can be involved in plasma-material interactions. Electrons from the plasma can also pose specific challenges to the solid materials. Neutrals are also present, produced through processes such as charge-exchange or injected by neutral beams. The complex nature of PMI is partly a result of this diversity of particles, but also a result of particle energy distribution, spatial distribution, and the evolution of these characteristics during device operation.

Additionally, for fusion reactions to occur, the plasma must have a temperature on the order of 1-10 keV [37], equivalent to 10-100 million degrees Kelvin. In magnetic

confinement schemes, magnetic fields confine the hot plasma and shield the vessel from direct contact with these extreme temperatures, but this confinement is far from perfect. Therefore, the problem of how to handle such enormous amounts of heat remains. The general concerns that arise from this exposure are the deterioration of the plasma-facing components (PFCs), and the degradation of plasma temperature by radiation of impurities produced by erosion of solid components. This chapter presents the relevant theory of PMI regarding these critical aspects, the specific effects of particle and heat flux on solid materials, magnetic effects, a review of experimental PMI testbeds, and a discussion on the particular characteristics of electrodes.

2.1 The Plasma Sheath

Regardless of the configuration, magnetically confined plasmas must reside within some solid vessel. The boundary between the solid surface and the plasma is a region of particular consequence with regard to the behavior and properties of the plasma. By definition, the plasma, which occupies the majority of the space in the vessel, is electrically neutral: $n_e = n_i$. A more general statement accounts for the sum over all ion charge states:

$$n_e = \sum_{i=1} Z_i n_i. \tag{2.4}$$

Here, n_e and n_i are the electron and ion number densities, while Z_i is the charge state of ion species i. In reality, at scales smaller than the Debye length, there may be regions of net charge, hence the notion of "quasi" neutrality, or $n_e \approx n_i$. At the boundary between the plasma and the solid surface, quasineutrality is no longer satisfied due to the formation of a thin layer of net charge known as the sheath. The sheath is a transition region that regulates the flow of particles and energy from the plasma to the solid surface. In this manner, the sheath strongly influences the properties of the bulk plasma [38]. Formation of the sheath is explained for the case

of a plasma confined by electrically floating walls. Assuming thermal equilibrium between ions and electrons ($T_i = T_e = T$), the ratio of thermal velocities highlights the relative mobility of electrons compared to ions.

$$\frac{V_{th,e}}{V_{th,i}} = \frac{\left(\frac{k_B T}{m_e}\right)^{1/2}}{\left(\frac{k_B T}{m_i}\right)^{1/2}} = \left(\frac{m_i}{m_e}\right)^{1/2} \approx 43. \tag{2.5}$$

If electrons have a greater temperature than the ions, their velocity will be even greater by some factor of $\sqrt{\frac{m_i}{m_e}}$. The electrons quickly charge the walls to a negative potential relative to the plasma potential. As the wall potential becomes more negative, electrons begin to be repelled, reducing their loss rate to the wall. The wall potential adjusts itself until an equilibrium is reached such that the ion and electron fluxes are equal. This establishes an ambipolar electric field in the plasma, shown in Fig. 2.1. At this point, a sheath with net positive charge has formed with thickness on the scale of the Debye length λ_D, and a potential difference on the scale of the electron temperature T_e.

Following the procedure outlined by Stangeby [2], assuming that $n_e = n_i$, and for a particle source proportional to the number density n in an isothermal fluid model, the plasma fluid velocity is limited by the isothermal sound speed c_s,

$$c_s = \left[\frac{k_B(T_e + T_i)}{m_i}\right]^{1/2}, \tag{2.6}$$

therefore the velocity at the entrance to the sheath, or sheath edge, v_{se} must also be less than c_s:

$$v_{se} \leq c_s. \tag{2.7}$$

However, considering the sheath side results in the statement [2]:

$$v_{se} \geq c_s. \tag{2.8}$$

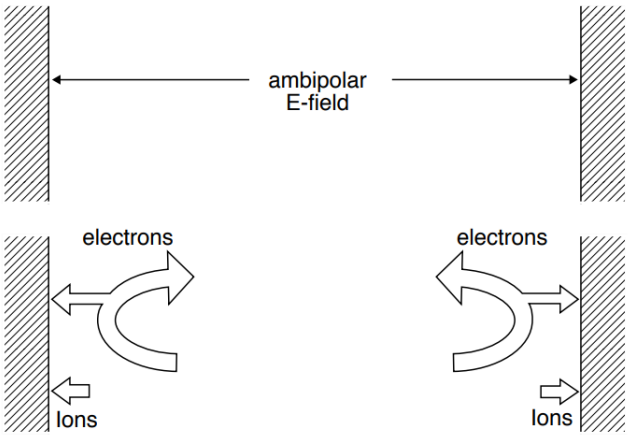

Figure 2.1: For an electrically isolated or floating wall, the ambipolar electric field is established across the plasma and sheath regions due to the equilibrium of the ion and electron fluxes to the wall. This figure is reproduced from Ref. [2].

Equation 2.8 is the Bohm criterion [39], which describes the minimum velocity required for ions to exit the plasma and enter the sheath. In order to acquire the Bohm velocity, there must be some potential driving the acceleration of ions within the bulk plasma. This occurs in the Bohm pre-sheath, which connects the sheath to the bulk, quasineutral plasma.

Next, the particle flux density Γ_{se} arriving at a surface through the sheath can be expressed in terms of the number density n and temperature T in Eq. 2.9. There is no dependence on the potential drop within the sheath, so the contribution of the sheath as a particle source can be neglected. Therefore, the particle flux at the sheath edge is equal to the flux arriving at the wall: $\Gamma_{se} = \Gamma_w$ [2].

$$\Gamma_{se} = n_{se} v_{se} = n_{se} c_s \approx \frac{1}{2} n_0 \left[k_B (T_e + T_i)/m_i \right]^{1/2} \tag{2.9}$$

However, the potential drop in the sheath is still a useful quantity in determining the

energy of ions that impact the wall and their heat flux. The potential of the wall relative to the sheath is V_w. For a floating wall, $V_w = V_{sf} < 0$, where V_{sf} is the floating potential due to the sheath. This is expressed as [2],

$$\frac{eV_{sf}}{k_B T_e} = 0.5 \ln \left[\left(2\pi \frac{m_e}{m_i} \right) \left(1 + \frac{T_i}{T_e} \right) \right]. \tag{2.10}$$

The derivation of Eq. 2.10, which expresses V_{sf} in terms of the ion and electron temperatures, assumes a Maxwellian one-way particle flux density [2]:

$$\Gamma_x = \frac{1}{4} n \bar{c} = \frac{1}{4} n \left(\frac{8 k_B T_e}{\pi m_e} \right)^{1/2}. \tag{2.11}$$

For $T_i \approx T_e$, and assuming a hydrogenic plasma, the floating potential is approximately $3T_e$. Therefore, for a 10 eV electron temperature, there is a 30 V potential drop through the sheath. Certain conditions can change the potential drop through the sheath, such as the emission of electrons. This may occur due to secondary electron emission or thermionic emission of electrons from a heated surface. The effect of electron emission is to make the floating wall potential more negative with respect to the plasma potential, because the emission of electrons from the surface requires a greater flux of electrons reaching the surface to maintain ambipolarity.

In the case of electrodes that are biased by applying an external voltage, there is a net current that flows through the plasma and the sheaths at each electrode. In the case of an isothermal, frictionless plasma, the applied electrode voltage is dropped in the two sheaths, which continue to provide ideal Debye shielding of the plasma. If the applied voltage is very large, then the electron-repelling surface, i.e. the cathode, takes up virtually all of the applied voltage [2]. Since ions entering the region of positive charge in the sheath are accelerated by the electric field to the surface, the ion impact energy increases by an amount proportional to the sheath potential. In the case of the SFS Z pinch, the applied voltage between the anode and cathode is

on the order of kilovolts, which substantially increases the ion impact energy. This is quantified as an increase in the heat flux to the surface in Sec. 2.3.

Conventional current flows to the cathode, while negative current flows to the anode. The potential of the anode relative to the plasma potential adjusts itself in order to regulate the flow of negative charge carriers as required by the external circuit [40], but remains negative with respect to the plasma potential. Concerns of electrode erosion on the SFS Z pinch are mainly on the cathode which receives the ion current and directly contacts the core Z-pinch plasma. This plasma-electrode contact is described in Sec. 3.1.

2.2 Particle Flux Effects

Significant modification to the solid components can occur due to particle impact. This often involves damage by excessive material loss or detrimental changes to the material properties. For instance, when incident ions collide with the atoms of the solid material with enough transfer of energy, atoms in the solid lattice may be ejected in a process known as physical sputtering. Significant levels of sputtering can result in net erosion of the surface material, limiting its lifetime and prompting repair or replacement. Physical sputtering, and other sputtering processes are quantified by the yield Y, which is the ratio of ejected particles to the incident particles, expressed as

$$Y = \frac{\Gamma_{ero}}{\Gamma_{in}}, \tag{2.12}$$

where Γ_{ero} is the eroded particle flux and Γ_{in} is the incident particle flux. The sputtering yield depends on the species of the particles involved, the impact energy, and the angle of incidence, all of which may be changing throughout device operation. Different regimes exist depending on the incident particle energy and mass. Low-Z ions impacting with low energy may only induce a single sputtering collision. At higher

energy, on the order of 10 eV, a collision cascade occurs in the solid as momentum is transferred to surrounding atoms. For even higher impact energies, in the keV to MeV range, and for high incident particle densities, there is significant generation of recoil atoms and local melting of the surface may occur [41]. Implantation of the incident ions can also occur at high ion impact energy, which reduces the sputtering yield. Physical sputtering can occur for any combination of incident particle and solid surface material, although the relative masses affect the efficiency of the energy transfer. Particles of similar mass will have the most efficient energy transfer. This is quantified by the energy transfer factor

$$\gamma = \frac{4M_1M_2}{(M_1 + M_2)^2}, \tag{2.13}$$

where M_1 and M_2 are the atomic masses of the incident particle and solid material respectively. For particles with similar mass, there is efficient energy transfer ($\gamma \approx 1$). The threshold energy for sputtering depends on the surface binding energy of the solid material. In practice, the value of the heat of sublimation is used as the surface binding energy [2]. In general, low-Z elements used for PFCs such as beryllium and carbon have lower binding energies than high-Z materials such as tungsten, leading to higher physical sputtering yields. However, the exact threshold will depend on the species of the incident ion.

Particular combinations of ion and PFC material can result in well-known degradation processes. Interactions between helium ions and tungsten are of particular concern. Tungsten is a common plasma-facing material in fusion devices due to its high melting point and low physical sputtering yield. However, the impact of helium ions induces blistering and the formation of fragile nanoscale "fuzz" on the tungsten surface that can easily be eroded and contaminate the plasma [42]. Another example is that of chemical sputtering, where formation of molecules occurs due to plasma particle impact. In the case of hydrogenic ions incident on carbon-based PFCs, the

formation of hydrocarbons such as CH_4 on the surface can enhance erosion due to the volatility of the molecule, especially at high surface temperatures [43].

In addition to erosion processes, redeposition of impurities removed from solid materials is an important process to consider. It is possible for sputtered material to be deposited back onto the surface where it originated. This is known as prompt redeposition, whereby the gyration trajectory of magnetized ions causes the ion to collide back with the solid surface. This mechanism is expected to significantly reduce the net erosion relative to the gross erosion in magnetic fusion devices [44]. However, sputtered material may also migrate and redeposit on a completely different surface elsewhere in the device. Redeposited layers can have different material properties compared to the original surface. For example, redeposited layers can enhance retention of deuterium and tritium [45]. Deposited layers with implanted hydrogen isotopes can result in embrittlement and reduced resistance to cracking [46]. Retention of hydrogen isotopes also dilutes the fuel content in the core plasma and causes buildup of unacceptably large amounts of radioactive tritium in the device.

Additional concerns are posed by neutron and electron impacts on the solid surfaces. In the nuclear environment of fusion devices, the energetic neutron flux can be particularly damaging. Significant attention has been paid to developing materials resistant to the detrimental effects of neutron irradiation including induced radioactivity, transmutation, and cracking [47, 48]. In a burning D-T plasma, energetic alpha particles, fuel ions, and runaway electrons all pose additional damage risk to PFCs [49]. Relativistic runaway electron populations are of significant concern [50], and have been observed in tokamaks to deposit MeV-scale energies to the walls [51].

2.3 Heat Flux

The abundant heating power produced by a fusion plasma presents a formidable challenge in terms of the power handling capability of the PFCs. In addition to the material requirements already discussed, PFCs must withstand steady state and dynamic heat loading from the plasma. Melting and sublimation of solid components from this thermal loading are significant concerns. Even at temperatures below the melting point of a typical material like tungsten, recrystallization can occur which results in reduced strength [52]. Thermal cycling can induce fatigue and cracking that compromises structural integrity. These processes can alter the thermal properties and dimensions of the PFCs. Decreased thermal conductivity and lower melting points reduce the effectiveness of a material against thermal loading, while dimensional changes may concentrate heat into smaller areas and increase the local heat flux.

Building upon the procedure presented in Sec. 2.2, the heat flux transmitted through the sheath can be calculated as follows. For the one-way Maxwellian flux density given in Eq. 2.11, the heat flux q in Wm^{-2} is given by the relation [2]:

$$q_x = 2k_B T \Gamma_x. \tag{2.14}$$

By definition, the Maxwellian distribution is taken to be at thermodynamic equilibrium, so there can be no net flux of particles or heat. However, at the interface between the sheath and the solid surface, denoted ss, the sink action of the surface on electrons results in no backwards-moving electrons. This also assumes that there is no electron reflection or secondary emission. The forward-moving electron flux at the ss still corresponds to a perfect Maxwellian with constant T_e [2], allowing the statement for electron heat flux to the surface from the sheath in Eq. 2.15. This requires assuming a sufficiently thin sheath such that the particle source within the

sheath is negligible, so that $\Gamma_{ss} = \Gamma_{se}$ [2]:

$$q_{ss}^{e} = 2k_B T_e \Gamma_{ss} = 2k_B T_e \Gamma_{se}. \tag{2.15}$$

Note that this expression gives the value of the electron heat flux to the surface, as opposed to the electron power lost from the plasma, which is greater in magnitude. The difference in power between these values is transferred to the ions that are accelerated through the sheath potential. Ions entering the sheath would tend to nullify the electrostatic field caused by the negatively charged surface, were it not for the energy from electrons to maintain the electrostatic field. In this way, the sheath is a mechanism for energy transfer from the electrons to ions. Due to the additional acceleration of ions in the presheath, the sheath edge ion distribution is not Maxwellian. However, the heat flux from ions can be approximated as the contribution from an assumed drifting Maxwellian [2], with the addition of the acceleration through the sheath potential V_{sheath}:

$$q_{ss}^{i} \approx (2k_B T_i + \mid eV_{sheath} \mid) \Gamma_{se}. \tag{2.16}$$

The total heat flux through the sheath is then the sum of the electron and ion contributions.

2.4 Magnetic Effects

Charged particles respond to magnetic fields by undergoing cyclotron motion along magnetic field lines. The presence of a magnetic field $\mathbf{B}$ at the plasma-material interface therefore has important implications for particle motion and sheath behavior, affecting the PMI processes in magnetic confinement devices.

Erosion processes eject neutrals from the surface, which are ionized in the plasma through collisions with electrons. The ionization mean free path for collision of neu-

trals with electrons is given by

$$\lambda_n = \frac{v_{th,n}}{\nu_n}, \tag{2.17}$$

where $v_{th,n}$ is the thermal velocity of eroded neutrals and ν_n is the collision frequency for neutrals with electrons. This can be compared to the ion Larmor radius, given by

$$r_L = \frac{mv_\perp}{eB}, \tag{2.18}$$

where m is the mass of the particle, $v_\perp$ is the velocity perpendicular to the circular particle motion, e is the elementary charge, and B is the local magnetic field strength. If the Larmor radius of an ionized neutral is larger than the ionization mean free path, cyclotron motion can result in redeposition back to the solid surface. When this redeposition occurs during the first gyration it is known as prompt redeposition, mentioned in Sec. 2.2. Prompt redeposition can be a highly favorable effect for limiting net erosion [53]. A weaker magnetic field increases the Larmor radius, which may enhance this redeposition process. In the SFS Z pinch, the azimuthal magnetic field is zero on the device axis, and increases to a maximum at the pinch radius. Since there is direct contact between the pinch and the electrode, the pinch radius determines the plasma-material contact area. Changes in the size of this contact area affect the local current density and magnetic field strength, and consequently the likelihood of prompt redeposition.

An additional effect of magnetic fields can be to reduce the overall particle and heat flux to a surface. The analysis in Sec. 2.1 assumes an unmagnetized sheath, or a configuration where $\mathbf{B}$ is parallel to the surface normal. However, such an arrangement is generally not present in magnetic confinement concepts. For instance, large values of the angle Ψ between the surface normal and $\mathbf{B}$ are desirable in tokamaks to minimize the proportion of parallel heat flux to the surface [2]. These are equivalent to a glancing angle between $\mathbf{B}$ and the surface plane. The azimuthal magnetic field around

a Z pinch is mostly parallel to the coaxial surfaces that make up the confinement vessel, therefore $\Psi = 90°$. The sheath structure due to a glancing, or oblique $\mathbf{B}$ is known as the Chodura sheath, shown in Fig. 2.2. The ion velocity at the entrance of the Chodura sheath, otherwise known as the magnetic pre-sheath edge, also follows the Bohm criterion in Eq. 2.8 [3]. Ions in a Chodura sheath are deflected by the electrostatic field due to their large Larmor radius and become parallel to the surface normal, while electrons remain undeflected due to their small Larmor radius. The implication is that the bulk plasma properties have no knowledge of the arrangement of the magnetic field lines with the surface, i.e. whether the sheath is normal or oblique. Therefore, the benefits of minimizing parallel heat flux to a surface can be realized without compromising the bulk plasma properties.

Despite this, it has been observed that the particle and heat fluxes incident to a surface tangential to the magnetic field lines can still be about 10% of the $\Psi = 0°$ case [54], suggesting the importance of cross-field transport for PMI in a Z-pinch configuration. This is quantified by applying a coefficient to the particle flux given in Eq. 2.9. This coefficient is given as

$$f_B = \left(\frac{D_\perp}{2Lc_s} \right)^{1/2}, \tag{2.19}$$

where $D_\perp$ is the perpendicular diffusion coefficient, L is a characteristic length for the surface, and c_s is the plasma sound speed. The diffusion coefficient is approximately equal to the Bohm coefficient [39] given by

$$D_\perp = \frac{1}{16} \frac{k_B T}{eB}, \tag{2.20}$$

where T is the plasma temperature and B is the magnetic field.

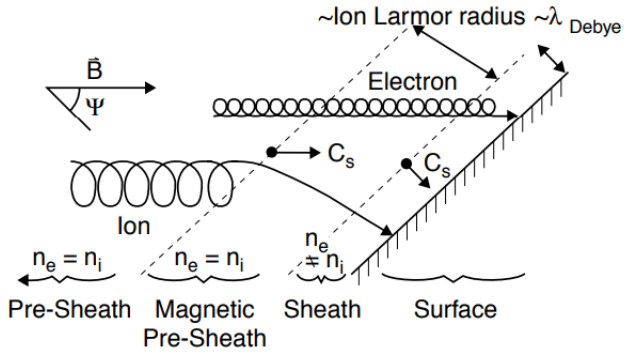

Figure 2.2: For magnetic field **B** at oblique angles to the wall, the Chodura magnetic pre-sheath arises between the ordinary pre-sheath and Debye sheath. The principal result of Chodura's analysis was that ions enter the magnetic pre-sheath according to the Bohm criterion and are deflected by the electric field to become parallel to the surface normal, while electrons are not deflected due to their smaller Larmor radius [3]. In this way, the bulk plasma has no knowledge of the arrangement of the magnetic field lines relative to the surface. The angle Ψ is defined to be between the magnetic field line and the surface normal. Figure reproduced from Ref. [3].

2.5 Effect of Plasma Impurities

A primary concern arises from the eroded impurities that enter the bulk plasma. An eroded impurity is ejected as a neutral, which is then ionized through electron impact, which may occur multiple times. Coulomb interactions between this ion and electrons in the plasma cause these electrons to change trajectory, thereby experiencing an acceleration. By conservation of energy, a photon is emitted with energy proportional to the change in energy of the electron due to the acceleration. As photons are unaffected by the confining fields, this radiation can escape the device if the plasma is optically thin at that wavelength. This is a loss of energy from confinement that leads

to reduction in the plasma temperature. This is known as bremsstrahlung radiation, and is a prominent cooling phenomenon in fusion devices. Bremsstrahlung losses in a hydrogen plasma scale with the square of the charge number Z by the following expression, given in units of W/cm^3 [55]:

$$P_{bremss} = 1.69 \times 10^{-32} N_e T_e^{1/2} \sum Z^2 N(Z) \tag{2.21}$$

Consequently, a tungsten ion with an atomic number of 74 will cause significantly more bremsstrahlung losses than a low-Z PFC material such as beryllium or carbon (atomic numbers 4 and 6 respectively). In other words, a fusion plasma is more tolerant to large amounts of low-Z impurities, whereas even a small amount of high-Z contamination can lead to detrimental cooling. Therefore, management of the impurity production is important not only for preventing damage to PFCs but also to reduce contamination and subsequent cooling of the fusion plasma.

2.6 Existing PMI Testbeds

The importance of PMI in fusion devices is underscored by extensive research over several decades [48, 56, 46], although with a large focus on toroidal configurations such as the tokamak and stellarator. The understanding of PMI effects specific to toroidal devices is therefore more mature compared to alternative approaches such as the SFS Z pinch. Due to this focus on toroidal configurations in mainstream fusion research, many existing PMI testbeds seek to replicate the edge plasma conditions expected on ITER. The typical benchmark conditions are steady-state heat fluxes of 20 MWm^{-2}, GWm^{-2} levels of transient heating, and low electron temperatures around 10 eV [57]. The exceptionally large transient heating is associated with the edge localized mode (ELM) instability [58], which enhances particle and heat flux to the walls and the divertor during steady-state operation. PMI studies for ITER-like

operational scenarios and magnetic field configurations are performed on contemporary large tokamaks such as JET [59] and DIII-D [60, 61], but may lack sufficient ion flux, neutron flux, or PFC surface temperatures [62]. However, long pulse durations of several hundred seconds and steady-state operation enable investigation of PMI effects for extended plasma exposure durations and high particle fluences.

A variety of linear plasma devices (LPDs) serve to overcome limitations present in toroidal configurations with regard to PMI studies, offering versatility and moderate costs [63]. Furthermore, these dedicated testbeds allow for well-defined exposure conditions and good access to material samples [62]. The incident ion fluences are large, on the order of $10^{27} - 10^{28}$ m^{-2} per steady-state exposure [62]. Examples of these devices include Magnum-PSI which can exceed expected tokamak particle and heat fluxes, and replicate the transient loading expected from ELMs [64]. Another example is the PSI-2 device, which has the capability of in-situ, in-vacuo sample analysis, simplifying the material analysis procedure and preventing contamination from exposure to atmosphere [63]. PSI-2 also serves as a pilot device for JULE-PSI which can combine neutron irradiation with transient thermal loading scenarios [65].

The SFS Z-pinch configuration offers several unique aspects as an experimental testbed for the study of PMI. First is the significantly higher plasma temperature, which leads to high ion impact energy and high heat fluxes. For example, the 1 keV electron temperatures demonstrated on ZaP-HD [1] are up to two orders of magnitude greater than for existing PMI testbeds, and 10 GWm^{-2} heat fluxes [66] are comparable to the thermal loading during ELM instabilities. In addition, this particle and heat flux are incident on a solid electrode that directly contacts the core Z-pinch plasma, rather than at the plasma boundary or in a divertor magnetic configuration for toroidal devices. Unlike PFCs in toroidal configurations, the electrode must also supply the plasma current, which can be up to hundreds of kiloamperes and causes

resistive heating of the solid material. The applied electrode voltage also enhances the ion impact energy by increasing the potential drop through the sheath, as described in Sec. 2.1. On the other hand, despite the elevated plasma temperature and presence of driven current, pulse durations on the SFS Z pinch are short–on the order of microseconds–which limits plasma exposure. An order of magnitude estimate assuming 10^{23} m^{-3} electron densities [1], calculating the sound speed with 1 keV ion temperatures, and assuming a 100 μs pulse gives a particle fluence of $\approx 10^{24}$ m^{-2}, which is a few orders of magnitude lower than for toroidal devices and LPDs. Obtaining a comparable particle fluence would require thousands of pulses for the described SFS Z-pinch conditions.

Operation of a solid electrode in extreme environments also occurs in vacuum and atmospheric arc discharges [67], cathodic arcs, [10] furnaces, [68] and plasma-based propulsion [11, 12]. These systems span a wide range of current densities and are also characterized by significant electrode surface heating, albeit for low plasma temperatures. Although the plasma and heat fluxes are concentrated on a relatively small area of plasma contact on the electrode, this also represents a small area to protect, which facilitates maintenance and replacement. Operation of these devices may provide useful techniques for managing erosion on the SFS Z-pinch electrode.

2.7 Electrode Characteristics

The plasma current in the SFS Z pinch is driven by the electrodes. The conduction of electrical current between electrodes occurs in a variety of configurations broadly referred to as electrical discharges or gas discharges, which includes the glow discharge, arc discharge, and the cathodic arc. There are important distinctions between the SFS Z pinch and these other discharges. Namely, the SFS Z pinch involves higher plasma temperatures of several hundred eV due to the adiabatic compression described in

Sec. 1.2, and higher sheath voltages on the order of kilovolts due to the applied voltage of the power supply. However, the basic characteristics of how electrodes function remain the same, and therefore provide a useful foundation for understanding the particular processes occurring at the SFS Z-pinch electrodes.

The primary purpose of electrodes in any configuration is to drive electrical current. By definition, this is the movement of charged particles, often ions and electrons. Conventional current is the flow of positive charge carriers, which travel from the anode to the cathode. Negative charge carriers therefore flow in the opposite direction from the cathode to the anode. This current is driven by the acceleration of charge carriers in the electric field produced by application of a voltage between the electrodes. A plasma is inherently composed of mobile positive and negative charge carriers, which facilitates the flow of current. This is in contrast to the charge carriers in a solid material. For instance, in a typical metallic conductor, current conduction is achieved through the mobility of delocalized electrons in the metallic lattice. In non-metallic materials such as graphite, the hexagonal bonding structure leaves one of the four carbon outer electrons free to move and to therefore conduct current. For a solid electrode to conduct electrical current through a plasma, some mechanism must exist at the plasma-material interface to provide current continuity between these two distinct regions. In the case of a cathode, negative charge carriers such as electrons must be emitted to provide this continuity. Electrons can escape the solid electrode through thermionic emission [69], where high surface temperatures provide energy to overcome the electron work function, or through field emission [70], where high electric fields permit tunneling through this energy barrier.

The method of production of the primary charge carriers, along with the current density, are often used to classify the various forms of electrical discharges. For example, glow discharges are characterized by a low temperature cathode where ions

primarily carry the current. Current densities are less than 10^4 A/m^2 and the voltage drop is above 100 V through the cathode sheath [40]. In thermionic arc discharges, the current is primarily carried by electrons produced via thermionic emission of a hot cathode. Arc discharge current densities are up to 10^6 A/m^2, and the cathode voltage drop is below 100 V [40]. The high surface temperatures involved in thermionic emission may cause significant melting and evaporation of the electrode material. The presence of sufficiently high local electric fields, on the order of $10^8 - 10^9$ V/m, can enhance thermionic emission by reducing the energy barrier, or result in field emission [40], which provides the required electron emission in the case of a cold (non-thermionic) cathode. At even higher current densities, between $10^8 - 10^{13}$ A/m^2, are cathodic arc discharges, which are characterized by sub-millimeter diameter, non-stationary cathodic arc spots. These extremely large current densities are sustained by concentrating the current over a small area, which intensifies the local heating and electric fields, resulting in greater thermionic and field electron emission. These cathodic arc spots are also characterized by dominance of plasma of the electrode material which has been eroded by the intense particle and heat fluxes, which results in a particularly damaging mode of operation. In the SFS Z-pinch configuration, the electrodes drive currents up to hundreds of kiloamperes for a pinch radius of a few millimeters. This results in current densities of approximately 10^9 A/m^2, within the range for the cathodic arc discharges. However, the Z-pinch plasma is not a cathodic arc, which suggests that the large current densities are sustained through mechanisms for electron emission other than thermionic and field emission.

The current density sustained by electron emission is limited by the space charge effect. This is given by the Child-Langmuir law [71],

$$j = \frac{4\varepsilon_0}{9}\left(\frac{2e}{m_e}\right)^{1/2}\frac{V_{sheath}^{3/2}}{d^2}, \tag{2.22}$$

where m_e is the electron mass, V_{sheath} is the voltage drop through the cathode sheath,

and d is the scale length of the region occupied by space charge, usually the separation of plane-parallel electrodes. In this case, this scale length is taken to be the sheath thickness of the SFS Z-pinch electrode, which is on the order of the Debye length,

$$\lambda_D = \left(\frac{\epsilon_0 k_B T_e}{n_e e^2} \right)^{1/2}, \tag{2.23}$$

which is calculated assuming the characteristic electron temperature and density provided in Ref. [1]. Assuming an applied voltage dropped through the cathode sheath of 10 kV, the Debye length given by Eq. 2.23 is on the order of 10^{-7} m and the space-charge-limited current density given by Eq. 2.22 is on the order of 10^{12} A/m^2, which exceeds the expected current density on the SFS Z pinch of 10^9 A/m^2.

Chapter 3

THE ZAP-HD FLOW Z-PINCH EXPERIMENT

The ZaP-HD experiment investigates the scaling of sheared-flow-stabilized Z-pinch plasmas at increased temperature and density. Evidence of stabilization was observed [13, 14, 15] on the original ZaP experiment which was consistent with the theoretical predictions made previously [33]. Following these results, the ZaP-HD device was designed to drive larger pinch currents to access higher plasma parameters.

The design of ZaP-HD is largely derivative of ZaP, with a few key modifications. A cross-section of the ZaP-HD configuration is provided in Fig. 3.1. Like ZaP, the device consists of a coaxial plasma accelerator coupled to a pinch assembly region. However, a third electrode (red) was added in between the inner (yellow) and outer (blue) electrodes. Neutral gas is injected by Parker fast puff valves into the annular volume between the inner and middle electrode. Eight azimuthally arranged valves are located 95 cm upstream of $z = 0$, referred to as the "outer" gas valves. Each opposing pair of valves is controlled by an individual triggering circuit. The single "inner" valve is located on a manifold 50 cm upstream of $z = 0$, puffing radially outward through eight outlets on the circumference of the inner electrode. The timing of each pair of outer valves and the inner valve can be independently controlled, although the full set of eight outer valves are generally triggered simultaneously.

The first of two capacitor banks is discharged across the inner and middle electrodes, ionizing the neutral gas and forming plasma. This is referred to as the discharge of the acceleration bank. The Lorentz force accelerates the plasma downstream until it reaches the assembly region. Here, the second capacitor bank is discharged,

driving additional current which compresses the plasma to high temperature and density. This is referred to as the discharge of the compression bank. Both capacitor banks consist of four 170 μF capacitors in parallel that can be charged up to 10 kV. The independently controlled capacitor banks decouple the plasma acceleration and plasma compression processes, providing enhanced control. This also enables higher pinch currents to be driven so that higher plasma parameters can be reached. Measurements indicate stability for approximately 50 μs, pinch radii of 0.3 cm, electron temperatures up to 1 keV, and electron density on the order of 10^{23} m^{-3} [1]. The Z-pinch plasma (magenta) contacts the inner electrode at the nose cone, which is a separate component threaded into the inner electrode tube. The inner electrode is the cathode of this configuration, therefore positive charge carriers flow in the upstream direction in the assembly region. The plasma-electrode interactions occurring at the cathode nose cone are the focus of the research presented in this dissertation.

3.1 Flow Z-Pinch Formation

The process of forming a flowing Z pinch with a radial velocity shear is shown schematically in Fig. 3.2. In stage (1), neutral gas (blue) is puffed into the annular region. In stage (2), the acceleration bank is discharged, resulting in a potential applied across the middle and inner electrodes. This discharge initiates breakdown of the neutral gas into plasma (red), and drives a radial current between the middle and inner electrodes. The direction of the current is given by the green arrows. This produces the azimuthal magnetic field in the direction shown. By considering the $\vec{J} \times \vec{B}$ cross product, where $\vec{J}$ is the current density vector and $\vec{B}$ is the magnetic field vector, the resulting Lorentz force accelerates the plasma in the downstream direction. Some residual neutral gas remains upstream. In stage (3), the ionization front approaches the end of the acceleration region. As the plasma enters the assembly region in stage

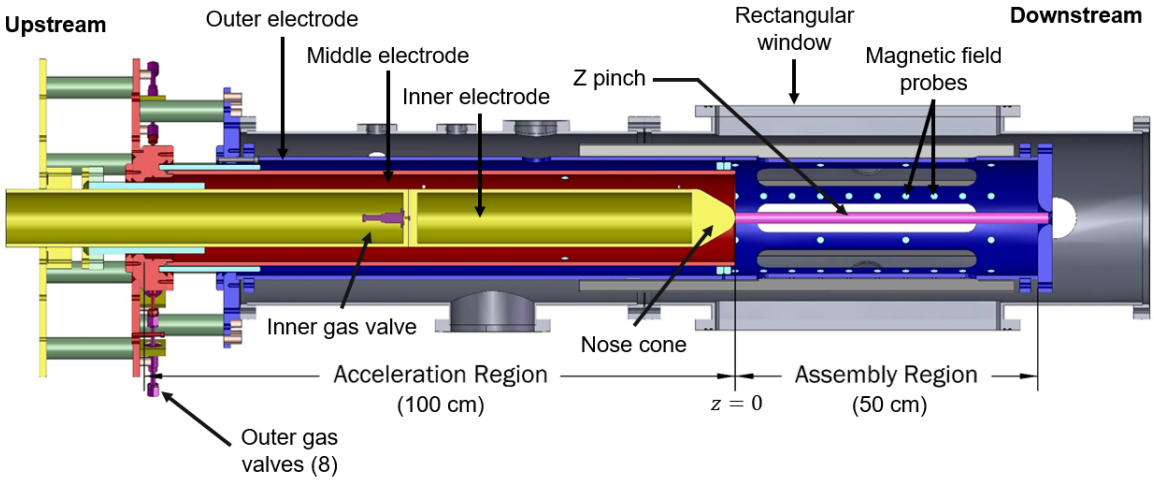

Figure 3.1: Section view showing the standard electrode configuration of the ZaP-HD device. The design uses three coaxial electrodes. Neutral gas is injected at two locations in the annular region between the inner electrode (yellow) and middle electrode (red). The first power supply discharges across these two electrodes, forming a plasma and accelerating it downstream. A second power supply is discharged across the inner electrode and outer electrode (blue) in the assembly region. This provides additional axial current to compress the Z-pinch plasma (magenta). The Z pinch contacts the inner electrode at the nose cone. The assembly region is equipped with a magnetic field probe array and fused silica windows for diagnostic access through slots in the outer electrode.

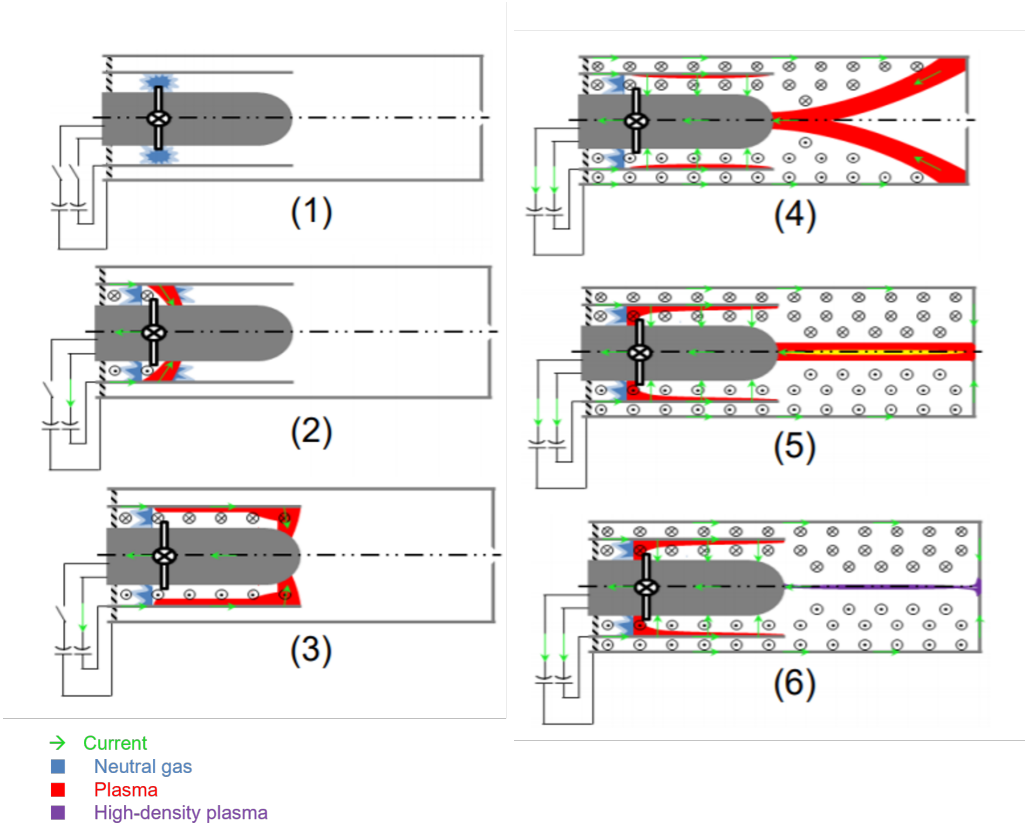

Figure 3.2: Schematic of the formation of a flow Z-pinch plasma on ZaP-HD. Neutral gas is puffed in the annular volume between the inner and middle electrodes (1). The acceleration capacitor bank is discharged, causing breakdown into plasma and forming a radial current and azimuthal field that produce a Lorentz force in the downstream direction (2). This accelerates the plasma downstream until it reaches the end of the acceleration region (3). The outboard current attachment moves from the middle to the outer electrode and continues downstream. The inboard current attachment remains on the inner electrode. The compression capacitor bank is discharged, supplying additional current as the plasma begins to assemble into a column on axis (4). The outboard plasma reaches the end wall of the outer electrode. The plasma forms a Z pinch with purely axial current, generating an azimuthal magnetic field. Residual gas from the accelerator supplies the assembly region with flowing plasma, providing the sheared flow (5). The axial current compresses and heats the Z pinch to high temperature and high density (6).

(4), the outboard current attachment moves from the middle electrode to the outer electrode, while attachment to the inner electrode remains. The compression bank is then discharged between the inner and outer electrodes, driving additional current through the plasma, which begins to assemble a column on axis. At stage (5), the attachment to the outer electrode has reached the end of the assembly region, and attaches to the end wall. The Z-pinch column is formed, with an axial current that generates an azimuthal magnetic field. Residual gas from the accelerator supplies the Z pinch with flowing plasma, providing the sheared flow. In stage (6), the axial current compresses and heats the Z pinch to high temperature and density. The Z pinch dissipates upon depletion of the residual gas supply, the magnitude of the current discharge from the capacitor banks crossing zero, or the growth of instabilities that disrupt the pinch current.

3.2 Diagnostics

A variety of diagnostics have been implemented to characterize the Z-pinch plasma formed on ZaP-HD. These consist of magnetic field probe arrays, current and voltage monitors, spectroscopy, and interferometry. Detailed descriptions of past diagnostic development on ZaP-HD can be found in Refs. [72] and [4]. This section provides an overview of the diagnostics relevant to this study.

3.2.1 Magnetic Field Probes

Both the acceleration and assembly regions on ZaP-HD are equipped with magnetic field probes, although a greater density of probes are in the assembly region to monitor the Z-pinch plasma. Since the study of plasma-electrode interactions concerns the contact of the pinch with the inner electrode, measurements from the assembly region probes are used. The magnetic field probes directly measure the time derivative of

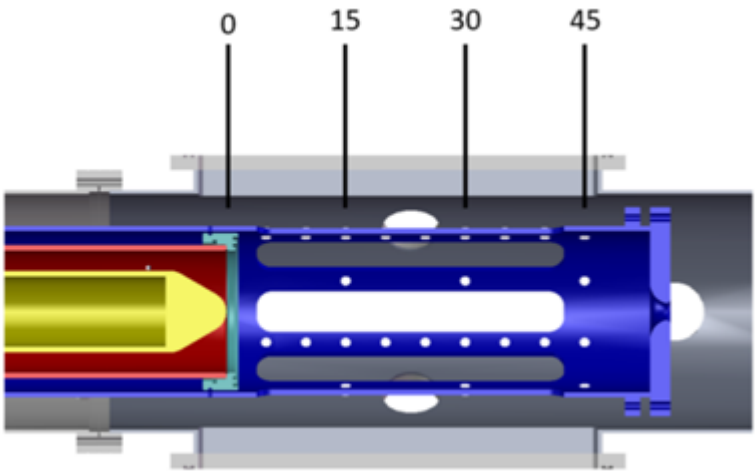

Figure 3.3: Locations of the magnetic field probes in the ZaP-HD assembly region. Probe arrays are spaced five centimeters apart beginning from $z = 0$. Every 15 cm there is an azimuthal array of eight probes. The remainder of axial locations have probes at four azimuthal locations.

the azimuthal magnetic field. This is expressed using Faraday's Law, which describes an induced voltage from a change in magnetic flux:

$$\int \frac{d\vec{B}}{dt} \cdot d\vec{A} = -\oint \vec{E} \cdot d\vec{l} = -V_i. \tag{3.1}$$

The magnetic probes consist of a coil of conducting wire with a total cross-sectional area A. A time-changing magnetic field $\frac{d\vec{B}}{dt}$ through the coil area induces a voltage V_i across the ends of the leads. This voltage is related to the time derivative of the field and the number of turns in the coil N:

$$V_i = -N \int \frac{d\vec{B}}{dt} \cdot d\vec{A} = -NA\frac{d\vec{B}}{dt}. \tag{3.2}$$

This voltage is then integrated to obtain the magnetic field. Figure 3.3 shows the arrangement of probes in the assembly region. An azimuthal array of four probes

is located every five centimeters, and an array of eight probes every 15 centimeters. Stability of the Z pinch is characterized by calculating the Fourier modes of the magnetic field data. Calculation of the $m = 0$ and $m = 1$ modes begins by applying a Fourier decomposition:

$$B_\theta(\theta_i) = \sum_{j=0}^{m} a_j \cos(j\theta_i) + \sum_{j=1}^{m} b_j \sin(j\theta_i) \tag{3.3}$$

B_θ is the azimuthal field, θ_i is the azimuthal probe location in radians, and a_j and b_j are unknown Fourier coefficients. The index j refers to the mode number, up to a maximum m. The azimuthal mode amplitudes are determined by solving for the Fourier coefficients. The measured field, coefficients, and trigonometric terms are placed into arrays **B**, **C**, and **A** respectively. Taking the pseudo-inverse of **A** returns the matrix of coefficients:

$$\mathbf{C} = (\mathbf{A}^T\mathbf{A})^{-1}\mathbf{A}^T\mathbf{B} \tag{3.4}$$

Using the coefficients, the mode amplitude and phase are calculated with the following equations:

$$m_j = \sqrt{a_j^2 + b_j^2} \tag{3.5}$$

$$\phi_j = \tan^{-1}(\frac{b_j}{a_j}) \tag{3.6}$$

The $m = 0$, or m_0, mode represents the mean amplitude of the magnetic field for each azimuthal array of probes, while m_1 describes the radial displacement of the current centroid from the center of the probe array. The value of m_1 is normalized by the maximum m_0 and the pinch is considered stable if the following relation is satisfied:

$$\frac{m_1}{m_0} = 2\frac{\Delta r}{r_{wall}}. \tag{3.7}$$

Here, Δr is the pinch displacement, and r_{wall} is the inner radius of the outer electrode. For $r_{wall} = 10.8$ cm, a normalized m_1 value of 0.2 means that the current is displaced

by 1 cm in the radial direction. Normalization by the m_0 mode defines the quiescent period only when there is a non-zero magnetic field, and therefore an axial current, in the assembly region. For the purposes of this study, the value of m_0 is used to calculate the axial pinch current at the position of the inner electrode nose cone. To do this, Ampère's Law is applied,

$$\int \vec{B} \cdot d\vec{l} = \mu_0 I, \tag{3.8}$$

where $\vec{B}$ is the magnetic field, $d\vec{l}$ is the differential of the closed loop defined by the radial position of the magnetic field probe array, and I is the enclosed current. Since there is only an azimuthal component for the magnetic field, $\vec{B} = B_\theta \hat{\theta}$. Carrying out the integration and rearranging for the current gives

$$I_{pinch} = \frac{2\pi r_{wall} B_\theta}{\mu_0}, \tag{3.9}$$

where r_{wall} is the same value as in Eq. 3.7, and B_θ is the mean amplitude of the magnetic field given by m_0 for the array of probes at some axial position. Throughout this dissertation, this axial current is referred to as the pinch current, and is evaluated at a particular axial location.

3.2.2 Ion Doppler Spectroscopy

Spectroscopy of the plasma-self emission is used for measuring a wide array of quantities relevant to fusion devices. The main advantage offered is the non-perturbing nature of the measurement, versatility of techniques, and relatively simple implementation. On ZaP and ZaP-HD, ion Doppler spectroscopy (IDS) has been used to extract the ion temperature from Doppler broadened spectra and the plasma flow velocity from the Doppler frequency shift [73, 74]. Since ZaP-HD mainly operates with a pure hydrogen plasma, IDS measures the radiation emitted by impurity ions, typically carbon and oxygen. The presence of higher ionization states is a qualitative indication of

the plasma temperature, while exact values of temperature are determined from the Doppler broadened spectra. Analysis of Doppler broadening is presented by Hutchinson [75], which relates the full width half-maximum of a Gaussian fit of the spectra to the ion temperature:

$$\Delta\lambda_{FWHM} = \lambda_o\sqrt{\frac{8k_BT_i\ln 2}{m_ic^2}}. \tag{3.10}$$

Two custom telecentric telescopes [76] view the plasma from above the assembly region through the rectangular fused silica windows shown in Fig. 3.1. The telescopes are mounted on rails so that different axial positions in the assembly region can be viewed. The radial telescope is perpendicular to the pinch axis, and therefore does not view any bulk plasma Doppler shift. The oblique telescope views 45 degrees from the pinch axis. Since a component of the plasma flow is normal to the telescope lens, the oblique telescope enables calculation of the bulk flow velocity as well as ion temperature. Spectroscopic emission from the plasma is focused by these telescopes onto a bundle of optical fibers. The fiber bundle is composed of 20 individual multimode fibers with 400 μm diameters arranged in a linear array. Within the plasma, these chords span a total of 23.6 mm. The emission is recorded by a gated PI-MAX 4 ICCD camera with 1024 x 1024 pixel resolution, coupled to an Acton 500i Czerny-Turner spectrometer with a UV-diffraction grating.

3.2.3 Current and Voltage Measurements

Rogowski coils measure the currents discharged through the electrodes on ZaP-HD. These coils consist of many loops of wire wrapped azimuthally around a longitudinal core of wire. This core is then looped around the cross-sectional area that the current intending to be measured passes through. Similarly to the magnetic field probes, Rogowski coils also function according to Faraday's law. The current passing trhough the large loop of the Rogowski coil induces a change in the magnetic flux through

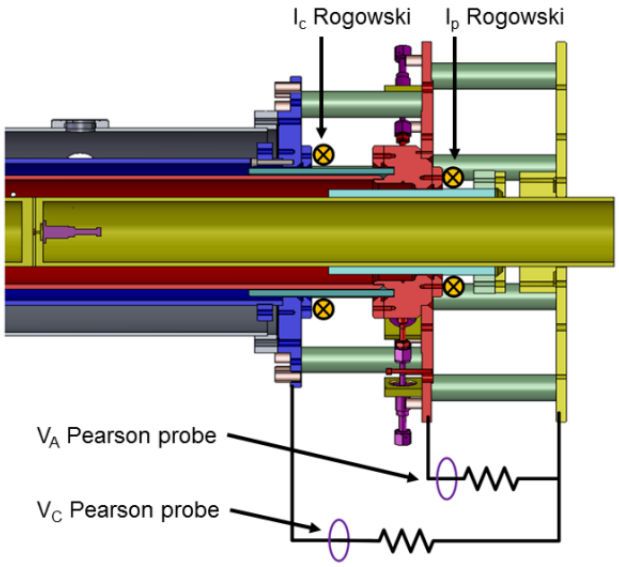

Figure 3.4: Cross-sectional view of ZaP-HD showing the placement of Rogowski coils and electrode voltage measurements. The image is flipped relative to Fig. 3.1 and corresponds to the left side of Fig. 3.1. This figure is reproduced from Ref. [4].

the smaller azimuthal loops, resulting in a voltage at the terminals of the coil. This voltage is proportional to the time rate of change of the current, and is integrated to obtain the current:

$$V_{rogo} = -\frac{d\phi}{dt} = -\mu_0 n A \frac{dI}{dt}. \tag{3.11}$$

Here, n is the total number of turns divided by the length of the Rogowski coil, and A is the overall coil area. The positions of the Rogowski coils on ZaP-HD are shown in Fig. 3.4. The total plasma current is given by I_P, and represents the total current discharged by both the acceleration and compression capacitor banks. Therefore, the I_P Rogowski coil encloses the inner electrode, which is the return path for the total discharge current. The compression current is given by I_C, which is the current

discharged by only the compression bank. The I_C Rogowski coil encloses both the inner and middle electrodes. Since the current through the middle electrode, which is from the discharge of the acceleration bank, is traveling opposite in direction to the I_P which is returning through the inner electrode, the current contributions subtract, resulting in measurement of the compression current I_C. The acceleration current, I_A, is not directly measured, but is calculated by the difference between the other two currents:

$$I_A = I_P - I_C \tag{3.12}$$

Also shown in Fig. 3.4 are circuit schematics that show how the electrode gap voltages are measured. Voltage is measured between each pair of electrodes by flowing a small amount of current through a Pearson current probe and high power resistors of known resistance. The measured current allows calculation of the voltage by Ohm's law, $V = IR$. The acceleration voltage V_A is measured between the middle and inner electrodes, while the compression voltage V_C is between the inner and outer electrodes. The potential of the middle electrode is given by the difference of these two values:

$$V_M = V_C - V_A. \tag{3.13}$$

3.2.4 Digital Holographic Interferometry

Laser interferometry methods measure the electron density of a plasma by recording the phase shift of a laser beam passed through the plasma. The plasma refractive index causes a shift in the phase velocity of an electromagnetic wave,

$$\phi = -\frac{e^2}{4\pi c^2 m_e \epsilon_0} \lambda N_e, \tag{3.14}$$

where the line-integrated density N_e is

$$N_e = \int n_e dl. \tag{3.15}$$

The laser beam is split into two beams, one of which is sent through the plasma and referred to as the scene beam, while the other beam is a reference beam that is routed outside of the plasma. Recombination of the beams results in a diffraction pattern containing the phase shift information. Early implementation of interferometry methods occurred on the ZaP device using holographic interferometry [77]. This involved recording the recombined beams with holographic film and extracting the phase and amplitude information using optical diffraction. An alternative method was developed using a four-chord interferometer which provides time-resolved measurements [78]. In either case, the electron number density n_e can be extracted from the chord-integrated measurement of N_e by applying an Abel inversion [77]. The development of digital holographic interferometry (DHI) on ZaP-HD uses numerical reconstruction of the hologram to extract the phase information, negating the need for holographic film [5]. This method is described in detail in the dissertation by Ross [4] and is further developed to obtain three-dimensional density data by Forbes [72]. DHI measurements are used in this study to provide radial profiles of the electron number density and electron temperature to determine the conditions of plasma exposure on the electrode, which is described in Chapter 4.

3.3 Characteristic ZaP-HD Plasma Pulse

This section presents the evolution of typical current and voltage measurements observed during a ZaP-HD pulse. The pulse presented in Fig. 3.5 is for a pure hydrogen gas injection with the acceleration bank charged to 9 kV and the compression bank charged at 7 kV. The inner and outer gas puff valves were triggered at 1.4 ms and 0.8 ms before the acceleration bank discharge, with inner and outer gas line pressures of 4500 and 4428 torr, respectively. Figure 3.5(a) shows the recorded electrode voltages, and Fig. 3.5(b) shows the recorded currents. The pulse is initiated with the

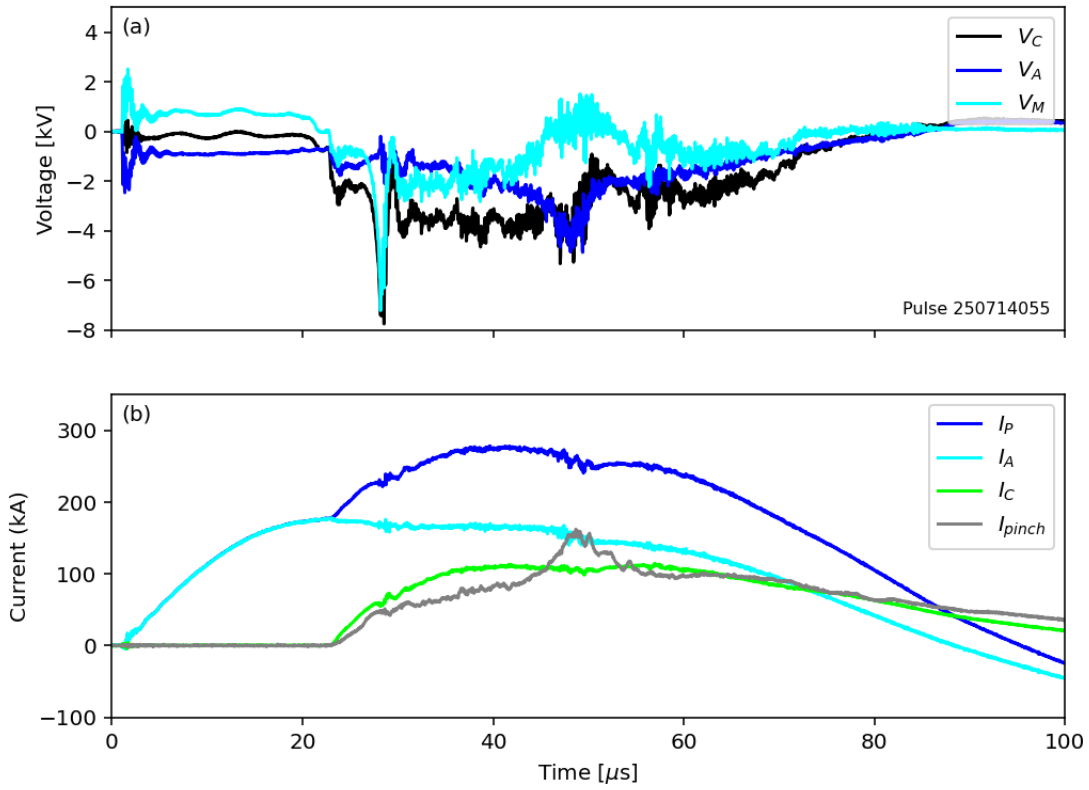

Figure 3.5: The measured electrode voltages (a) and currents (b) for a typical plasma pulse on ZaP-HD. In (a), the accelerator voltage, V_A, and middle electrode voltage, V_M step during the acceleration bank discharge. There is a corresponding rise in the total plasma discharge current, I_P, and I_A in (b). The compression bank is discharged 20 μs after the initial discharge, causing a step in the compression voltage, V_C, and a rise in the compression current, I_C. The total current I_P now records the sum of I_A and I_C. The pinch current calculated from magnetic field probes at $z = 10$ cm in the assembly region, I_{pinch}, also rises at this time, indicating that a pinch has assembled with axial current to produce the measured azimuthal magnetic field. After this time, plasma dynamics cause rapid spikes in the voltage. The pulse ends when I_P crosses zero at approximately 95 μs, although RLC oscillations in the current continue over a longer time period.

discharge of the acceleration bank at $t = 0$ μs. In Fig. 3.5(a), the step in acceleration voltage V_A and middle electrode voltage V_M occurs at approximately 2 μs due to the delay from the transmission of the trigger signal to the actual voltage being applied to the electrodes. This discharge ionizes the gas and accelerates the resulting plasma downstream. There is a corresponding rise in Fig. 3.5(b) in the I_P and I_A Rogowski coil measurements. V_M drops to zero at roughly 22 μs, indicating that conductive plasma has reached the end of the accelerator and attaches to the outer electrode as described in Sec. 3.1. This grounds the middle electrode to the outer electrode. The compression bank is then discharged, which is triggered 20 μs after the acceleration bank. At this time, the compression voltage V_C steps, and the compression current I_C rises, which adds to the total discharge current in I_P. The pinch current, I_{pinch}, rises at this time as well. The pinch current is evaluated using magnetic field probes at $z = 10$ cm, using Eq. 3.9. This indicates that there is an axial pinch current at $z = 10$ cm in the assembly region. After this time, changes in the plasma inductance lead to rapid spikes in the voltage measurements between 25 and 55 μs. The total discharge current I_P decreases and crosses zero around 95 μs, but will oscillate over a longer time scale following the RLC characteristic of the overall circuit. This marks the end of the pulse.

3.4 Previous PMI Investigations on ZaP-HD

PMI experiments were conducted by Forbes [72] on ZaP-HD which studied the effects of plasma kinetic and thermal energy on the material surface of targets exposed to the Z-pinch plasma. Effects on the plasma performance with the targets perturbing the plasma were also monitored. To control the kinetic energy, the acceleration bank voltage setting was varied. Changing this voltage setting changed the radial current driven in the accelerator, which determines the resulting Lorentz force that accelerates

the plasma downstream. To control the thermal energy, the compression bank voltage was varied. This setting controls how much axial current is driven through the Z pinch in the assembly region, which determines the compression and subsequent heating of the plasma. Although some heating of the plasma likely occurs during acceleration, most of the thermal energy imparted to the plasma occurs through compression. Graphite and boron nitride targets were placed in the plasma path within the assembly region and exposed to pulses of various kinetic and thermal energy. The total particle fluence was controlled by changing the number of pulses for each target.

Plasma parameters near the targets were monitored with spectroscopy, magnetic field probes, high-speed imaging, and DHI. A thermistor placed at the back of the target measured changes in the target temperature. Ex-situ analysis of the target surfaces was obtained using scanning electron microscopy (SEM) and energy dispersive X-ray spectroscopy (EDS). The main observations derived from this study showed that insertion of the target into the plasma did not affect the upstream plasma parameters. Stagnation of the plasma surrounding the target prevented the magnetic field from penetrating the material, and also reduced the particle and energy flux to the target surface. Micrographs of the graphite surface morphology showed evidence for redeposition of sputtered carbon for low energy plasmas that were not evident at high energy settings. For high energy settings, the calculated heat deposition exceeded the energy required for graphite sublimation. Evidence of graphite melting was observed on the sides of the target, which was hypothesized to occur due to sufficiently high plasma pressures. Boron-nitride targets showed evidence of melting over all settings and a dependence on total ion fluence. These results provide interesting insight into the material response to plasma exposure in ZaP-HD, indicating significant changes to surface morphology, and evidence for thermal effects such as melting. This dissertation builds upon the work by Forbes to investigate the PMI occurring

at the electrodes, which is the area of most concern for erosion damage in the SFS Z pinch.

Significant erosion of the inner electrode was originally observed on the ZaP experiment [79]. The electrode was composed of solid C11000 copper with a tungsten spray between up to 500 μm thick. Similar erosion was observed on the ZaP-HD experiment which initially operated with an identical electrode material [80]. Operation of ZaP-HD over thousands of plasma pulses removed a circular area of tungsten roughly 25 mm in diameter at the electrode nose cone, where contact with the Z-pinch plasma occurs. This damage is shown in Fig. 3.6. Some pitting is visible on the exposed copper surface which is no longer protected from sputtering by the tungsten layer. Solidified droplets of molten tungsten are visible around the periphery of this area. These droplets decrease in size and number further away from the nose cone tip, suggesting a decrease in surface temperature and melting away from the tip. Subsequently, a graphite nose cone was installed on ZaP-HD to help mitigate high Z impurity production from tungsten and to improve electrode durability. Qualitatively, no visible signs of erosion were observed after a few hundred pulses on the graphite nose cone [80].

3.5 Electrode Coupons

The targets used in the experiments by Forbes had no appreciable current flow, and therefore did not reproduce the plasma-electrode interactions which are the focus of this dissertation. To achieve this, the nose cone of the ZaP-HD inner electrode was redesigned with a removable coupon. Figure 3.7(a) shows the ZaP-HD assembly region with the modified electrode outlined in red. An enlarged view of this region is given in Fig. 3.7(b). The entire inner electrode assembly was moved 8 cm further downstream from the original position illustrated in Fig. 3.1, which improves optical access through

Figure 3.6: The original tungsten-sprayed copper electrode nose cone used on ZaP-HD showed substantial erosion damage at the location of contact with the Z-pinch plasma. A roughly 25 mm diameter area of tungsten has been completely removed, and the exposed copper underneath is marked with pits and craters. Solidified droplets of molten tungsten are evident at the periphery of the damaged region, and decrease in size and number away from the nose cone tip.

the rectangular windows. The coupon is effectively the entire tip of the electrode nose cone with internal mating surfaces. Four silver-plated 6-32 socket head cap screws, visible in Fig. 3.7(c), fasten the coupon to the larger graphite base component. All coupons, as well as the base component, were machined out of POCO AXF-5Q graphite. Coupon dimensions, shown in Fig. 3.8, were restricted by the sample stage of the ex-situ surface analysis tools and the slots within the outer electrode shown in Fig. 3.7(a) which were used for installation. The coupon dimensions maximize the surface area available for ex-situ analysis within these constraints. Coupon installation can be completed within two hours, enabling rapid and frequent replacement.

A cutaway of the electrode assembly design is provided in Fig. 3.9. The graphite nose cone is divided into two components, the base and the coupon. When assembled, the overall geometric profile of the assembly is identical to the previous nose cone design. The base component retains the 16 TPI external threads for installation within the inner electrode copper tube. There is a thread relief that serves two purposes. It provides a run-out zone for the lathe tool when turning the threads, and prevents an inner radius on the corner of the mating surface with the copper tube. This ensures good contact between the graphite and copper mating surfaces, which avoids a misalignment of material that could disrupt the current flow on the electrode surface. The volume of the thread relief is vented by an axial slot cut into the threads (not visible in Fig. 3.9). The coupon is fastened to the base by the four socket head cap screws. Counter-bored holes ensure that the socket heads do not protrude from the nose cone profile. Stainless steel threaded inserts are installed in the base. This avoids using graphite threads that are easily damaged, improving the re-usability of the assembly. The screws are slot-vented to evacuate the blind hole. A single 6-32 tapped hole on the coupon is used to thread a long screw which acts as a handle for transporting the coupon during installation and removal in the limited space of

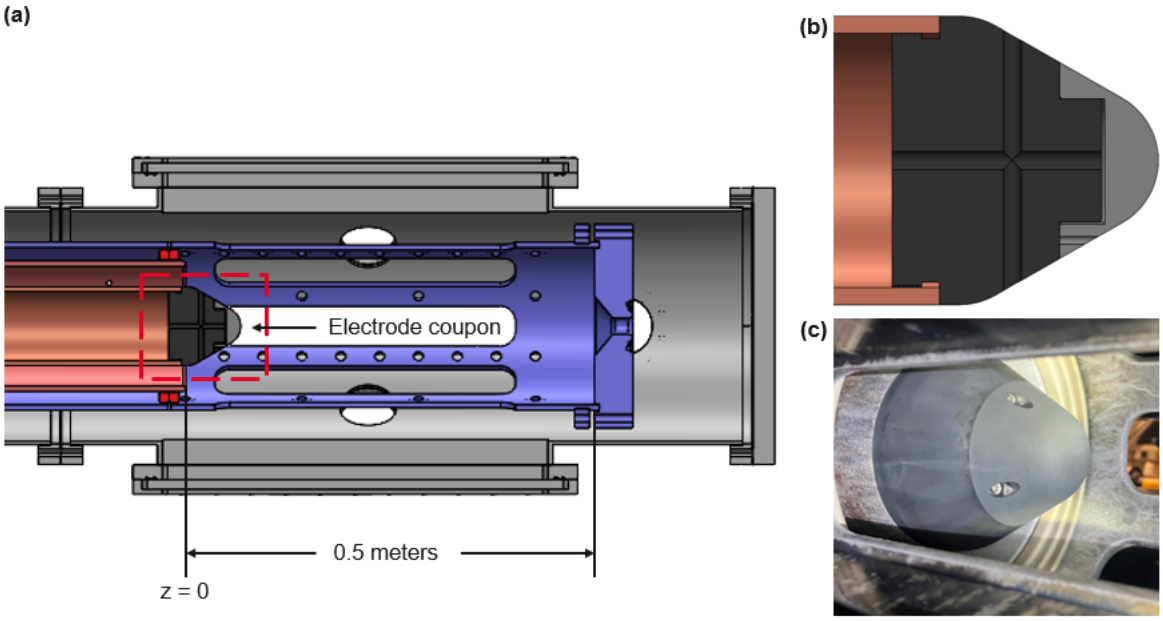

Figure 3.7: (a) Cross-sectional machine drawing of the assembly region showing the inner electrode positioned 8 cm downstream of $z = 0$, providing optical access for spectroscopy measurements through the fused silica windows. The redesigned electrode assembly incorporating the removable coupon is outlined in red. Removal of the windows enables access for coupon replacement through the slots in the outer electrode. (b) Enlarged section-view of the electrode coupon assembly. Fasteners are not visible in the plane of the cross-section. (c) Image of a pristine graphite electrode coupon installed on ZaP-HD with visible fasteners.

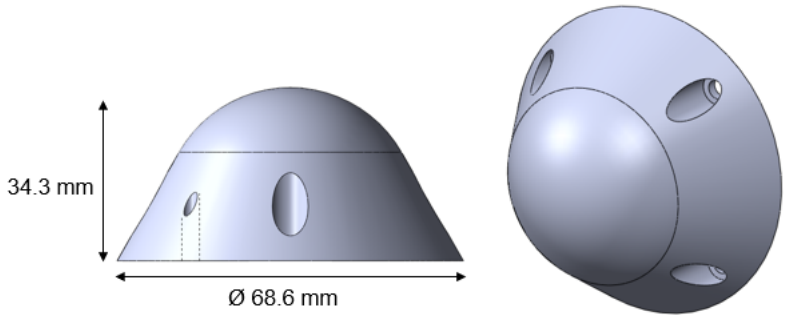

Figure 3.8: Major dimensions of the graphite electrode coupon. The dimensions were selected to enable installation through the ZaP-HD outer electrode slots, fit onto surface analysis instrument sample stages, and to maximize the surface area for analysis.

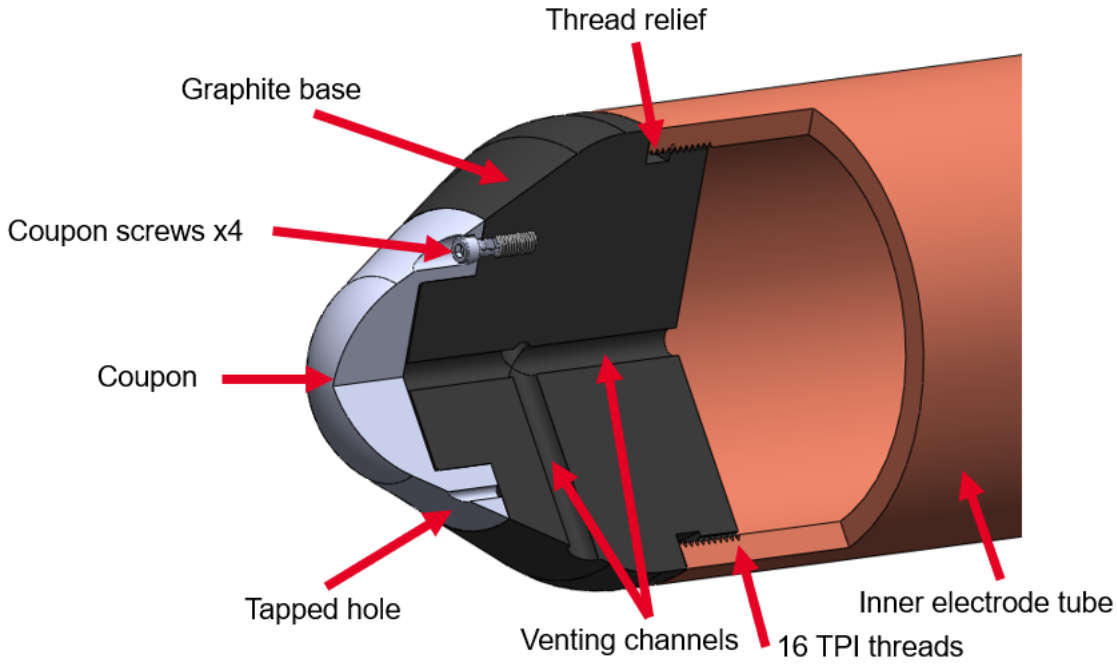

Figure 3.9: Section view of the redesigned ZaP-HD electrode assembly with removable coupons, illustrating internal features and venting channels. The coupon is fastened to a graphite base component. The base component threads into the copper electrode tube. The overall profile of the redesigned nose cone is identical to the previous design.

the assembly region. This prevents contact with the plasma-facing surface, since it is critical to preserve the surface for ex-situ analysis. The coupon has an internal bore which mates to the corresponding boss feature on the base component. This locates the coupon on the base prior to fastening with the screws. A slight gap is maintained between these internal mating features to ensure good contact between the coupon and the base component at the external interface. This gap is evacuated by internal venting channels in the base.

3.6 Framework for Plasma-Electrode Interaction Experiments on ZaP-HD

This experimental investigation involves both in-situ and ex-situ diagnostics. In-situ measurements of electrode erosion and the surface temperature are obtained through S/XB spectroscopy and two-color pyrometry, which are described in Chapters 4 and 5. Next, the response of the electrode material is determined through ex-situ surface analysis, described in Chapter 7. SEM, optical profilometry, and EDS measure changes in the microscopic surface morphology and topography of the electrode coupons. A total of four coupons were installed on ZaP-HD. The first coupon was exposed to a variety of experimental parameters for the purpose of verifying and characterizing operation of ZaP-HD with the new nose cone assembly. The remaining three coupons were part of three experimental campaigns with controlled exposure conditions. Two parameters were varied: the applied voltage during compression of the plasma and the number of pulses. The compression voltage controls the pinch current. Higher pinch currents lead to increased density and temperature based on the scaling described in Sec. 1.2. This results in higher current densities and greater particle and heat flux to the electrode. The number of pulses controls the total particle fluence on the electrode. The parameters of each plasma exposure case are summarized in Table 3.1, along with the maximum pinch current measured at $z = 10$ cm. The pinch current is averaged over all pulses within each campaign. For all cases, the initial capacitor bank discharge for plasma generation and acceleration was set to the maximum setting of 9 kV. Case I represents the most intense plasma exposure in this study, while Case III is the least intense.

Case	Accel. Voltage [kV]	Comp. Voltage [kV]	Total Pulses	Max. Pinch Current [kA]
0	9	Mixed	155	≥ 81
I	9	9	200	136
II	9	7	50	114
III	9	5	42	98

Table 3.1: Experimental parameters for the four graphite electrode coupons tested on ZaP-HD. Case 0 was a test campaign to verify and characterize operation with the prototype electrode assembly, and did not strictly control the voltage settings. Cases I, II, and III controlled the compression voltage and the total number of pulses. The compression voltage setting determines the axial pinch current that compresses the plasma in the assembly region. The number of pulses sets the total particle fluence incident on the electrode. The maximum pinch current is a campaign-averaged value calculated from magnetic field measurements at $z = 10$ cm.

Chapter 4
S/XB SPECTROSCOPY

Spectroscopy has long been a valuable tool for monitoring the erosion of solid components in fusion devices. Early applications occurred in the 1980s on various tokamaks [81, 82, 83, 84, 85] and continues in more recent experiments [61, 86, 87]. This chapter describes the implementation of the S/XB spectroscopy method on ZaP-HD to measure the gross erosion flux of carbon from the graphite electrode. Also known as the ionizations per photon method, this technique infers the erosion flux from measurements of the absolute emission intensity of eroded impurity ions. The emission intensity is recorded as a photon flux, and is converted to an erosion flux by applying the appropriate ionization and excitation rates. The ionization rate gives the population of the radiating ions and the excitation rate determines the flux of photon emission by that population of ions. The ratio of ionization to excitation rates is the eponymous S/XB coefficient, which converts the photon flux to an erosion flux. The basic form of this expression is given as

$$\Gamma = 4\pi \left(\frac{S}{XB} \right) I, \tag{4.1}$$

where Γ is the eroded atom flux (atoms $\mathrm{m}^{-2}\mathrm{s}^{-1}$), S is the ionization rate, X is the excitation rate, B is the branching ratio, and I is the line-integrated absolute intensity of emission converted to a photon flux (photons $\mathrm{m}^{-2}\mathrm{s}^{-1}\mathrm{sr}^{-1}$). The general benefits of spectroscopy apply, namely that this diagnostic is non-perturbing to the plasma and that the measurement can be performed in-situ. Additionally, a wide degree of spatial and temporal resolutions are available depending on the particular apparatus.

Monitoring the erosion flux is useful for predicting component lifetimes, evaluating erosion mitigation strategies, and characterizing impurity production. The following sections describe the basic theory, implementation, and interpretation of results of S/XB spectroscopy on ZaP-HD.

4.1 Theory

The S/XB method assumes that excitation and ionization occur solely through electron impact. For electron energies comparable to the excitation and ionization potentials (several eV), the cross-sections for inelastic electron collisions are several orders of magnitude larger than that for heavy particle collisions such as charge exchange. In the following expressions, A represents a neutral atom in the ground state, A^* represents an excited state, and A^+ represents an ion. Electron impact excitation of bound electrons is described by

$$A + e \rightarrow A^* + e, \tag{4.2}$$

while electron impact ionization is described by

$$A + e \rightarrow A^+ + e + e. \tag{4.3}$$

The de-excitation process is restricted to spontaneous emission of a photon with frequency ν:

$$A^* \rightarrow A + h\nu. \tag{4.4}$$

This frequency often corresponds to wavelengths in the visible or UV range, which is readily accessed by standard spectroscopic apparatus. Eroded impurity ions may penetrate further into the plasma and undergo multiple ionizations. As a result, lower ionization states tend to be more localized to their source and therefore more representative of the erosion flux. However, depending on the local plasma parame-

ters, lower ionization states may be less accessible for measurement due to their low ionization energies and rapid burn-through times.

4.1.1 Excitation and Ionization Rates

The cross-section σ for electron ionization and excitation describes the probability for that process to take place. Classically, a cross-section is the area transverse to the velocity vectors of the interacting objects. This is usually given in units of barns, where 1 barn = 10^{-28} m^2. The cross-section is then averaged over a Maxwellian distribution of the electron velocity v:

$$\langle \sigma v \rangle = \int_0^\infty \sigma v f(v)\, dv. \tag{4.5}$$

Here, $f(v)$ is given by the one-dimensional Maxwellian distribution function:

$$f(v)dv = \left(\frac{m_e}{2\pi k_B T_e}\right)^{\frac{1}{2}} exp\left(-\frac{m_e v^2}{2k_B T_e}\right) dv \tag{4.6}$$

where m is the particle mass, k_B is the Boltzmann constant, and T_e is the electron temperature. Since excitation and ionization processes are assumed to only occur due to electron collisions, population of an ionization state is determined by the electron ionization rate. This rate depends on the number density of atoms or ions n_A, the number density of electrons n_e, and the velocity-averaged cross-section. Let the ionization cross-section be σ_i and the ionization rate be S with units of m^{-3}s^{-1} in the following expression,

$$S = n_A n_e \int_0^\infty \sigma_i v_e f(v_e)\, dv, \tag{4.7}$$

which is simplified to

$$S = n_A n_e \langle \sigma_i v_e \rangle. \tag{4.8}$$

A similar expression for the excitation rate, X, is defined, taking σ_{Em} to be the excitation cross-section from the ground state to level m:

$$X = n_A n_e \langle \sigma_{Em} v_e \rangle \tag{4.9}$$

4.1.2 Ionizations per photon derivation

The following derivation is adapted from Bogen and Hintz [88], with a few changes to variable names. The assumption is made that radiative or collisional recombination is negligible due to long recombination times relative to particle residence times in the plasma edge. For low electron densities, the spectral line intensities are determined by the electron impact excitation rate X, given in Eq. 4.9. Each excitation event emits a single photon, and this emissivity is expressed by the emission coefficient with units of photons $\mathrm{m}^{-3}\mathrm{s}^{-1}\mathrm{sr}^{-1}$:

$$\epsilon = \frac{1}{4\pi} n_e n_A \langle \sigma_m v_e \rangle. \tag{4.10}$$

The line intensity I measured in experiments is the line-integrated value of the emission coefficient ϵ, with x_1 and x_2 defining the boundaries of the emitting layer:

$$I = \int_{x_1}^{x_2} \epsilon \, dx = \int_{x_1}^{x_2} \frac{1}{4\pi} n_e n_A \langle \sigma_m v_e \rangle \, dx. \tag{4.11}$$

Next, the radial dependence of the ionization of neutral atoms is described by:

$$\frac{d(n_A v_A)}{dr} = S = n_e n_A \langle \sigma_i v_e \rangle. \tag{4.12}$$

Rearranging for the product of the number densities from Eq. 4.10 gives:

$$n_e n_A = 4\pi\epsilon \frac{1}{\langle \sigma_m v_e \rangle}. \tag{4.13}$$

Substituting into Eq. 4.12 gives:

$$\frac{d(n_A v_A)}{dr} = \frac{d\Gamma_A}{dr} = 4\pi\epsilon \frac{\langle \sigma_i v_e \rangle}{\langle \sigma_m v_e \rangle}. \tag{4.14}$$

The left hand term is equivalent to the radial component of the particle flux Γ of species A. Integrating with respect to r gives

$$\int_0^r \frac{d(\Gamma_A)}{dr}\, dr = \Gamma_A = 4\pi \int_0^r \epsilon \frac{\langle \sigma_i v_e \rangle}{\langle \sigma_m v_e \rangle}\, dr. \tag{4.15}$$

Assuming that the ratio $\frac{\langle \sigma_i v_e \rangle}{\langle \sigma_m v_e \rangle}$ is constant along the radial coordinate, it can be removed from the integral:

$$\Gamma_A = 4\pi \frac{\langle \sigma_i v_e \rangle}{\langle \sigma_m v_e \rangle} \int_0^r \epsilon\, dr. \tag{4.16}$$

Using the intensity given in Eq. 4.10, integrating over the solid angle, and with the line of sight for I in the radial direction, the expression is simplified as

$$\Gamma_A = 4\pi \frac{\langle \sigma_i v_e \rangle}{\langle \sigma_m v_e \rangle} I. \tag{4.17}$$

Note that the ratio of the Maxwellian averaged cross-sections is equivalent to the ratio of S and X given in Eqs. 4.8 and 4.9 respectively, since the number density terms divide out. Rewriting in terms of these ionization and excitation rates gives the form introduced earlier as Eq. 4.1:

$$\Gamma_A = 4\pi \frac{S}{XB} I. \tag{4.18}$$

The branching ratio B is not explicitly included in this derivation, but is necessary to describe the fraction of particles that undergo the particular radiative decay path for the excitation described by X.

4.1.3 S/XB Coefficients

Collisional-radiative models have been developed [89] to obtain values of the S/XB coefficients. For this study, the line emission of C-III at 229.7 nm was selected for its strong intensity and isolation from other line radiation. This wavelength has been used previously for spectroscopic measurements on the ZaP [90] and ZaP-HD [74]

SFS Z-pinch devices. S/XB coefficients for C-III were obtained from the Atomic Data and Analysis Structure (ADAS) database [91]. These are shown in Fig. 6.2 for plasma parameters observed on ZaP-HD. Due to this variation, application of the S/XB method depends on accurate knowledge of the local plasma temperature and density.

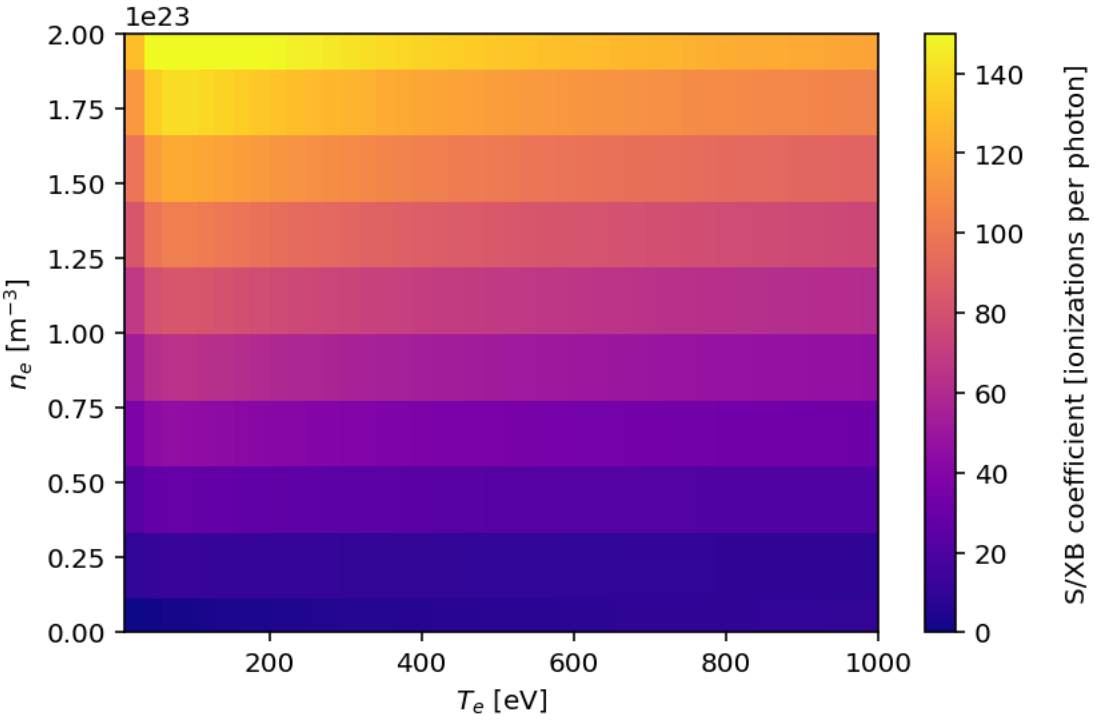

Figure 4.1: S/XB coefficients obtained from the ADAS database for the 229.7 nm line emission of the C-III ion, showing variation for the range of typical ZaP-HD plasma parameters. These coefficients are used to convert the measured photon flux of C-III emission into an inferred erosion flux of carbon neutrals.

4.2 Implementation on ZaP-HD

4.2.1 Spectroscopic Setup

This diagnostic uses a similar setup as the IDS measurements on ZaP and ZaP-HD [73, 74] as described in Sec. 3.2.2. The 229.7 nm line radiation emitted by the plasma is transmitted through the fused silica windows and focused by the radial telecentric telescope onto the optical fiber bundle, which is composed of 20 chords. Figure 4.2 shows the position of the radial telescope viewing the graphite electrode through the top window of the ZaP-HD assembly region. Figure 4.3 shows the impact parameter x of the 20 chords overlaid on the profile of the electrode nose cone. For chords that terminate on the electrode surface, the chord-integrated intensity includes emission of C-III near the surface as well as emission along the entire line of sight. To isolate the C-III emission measured at the nose cone surface, the intensity of the four outermost chords, which do not terminate on the nose cone, are subtracted as a background measurement.

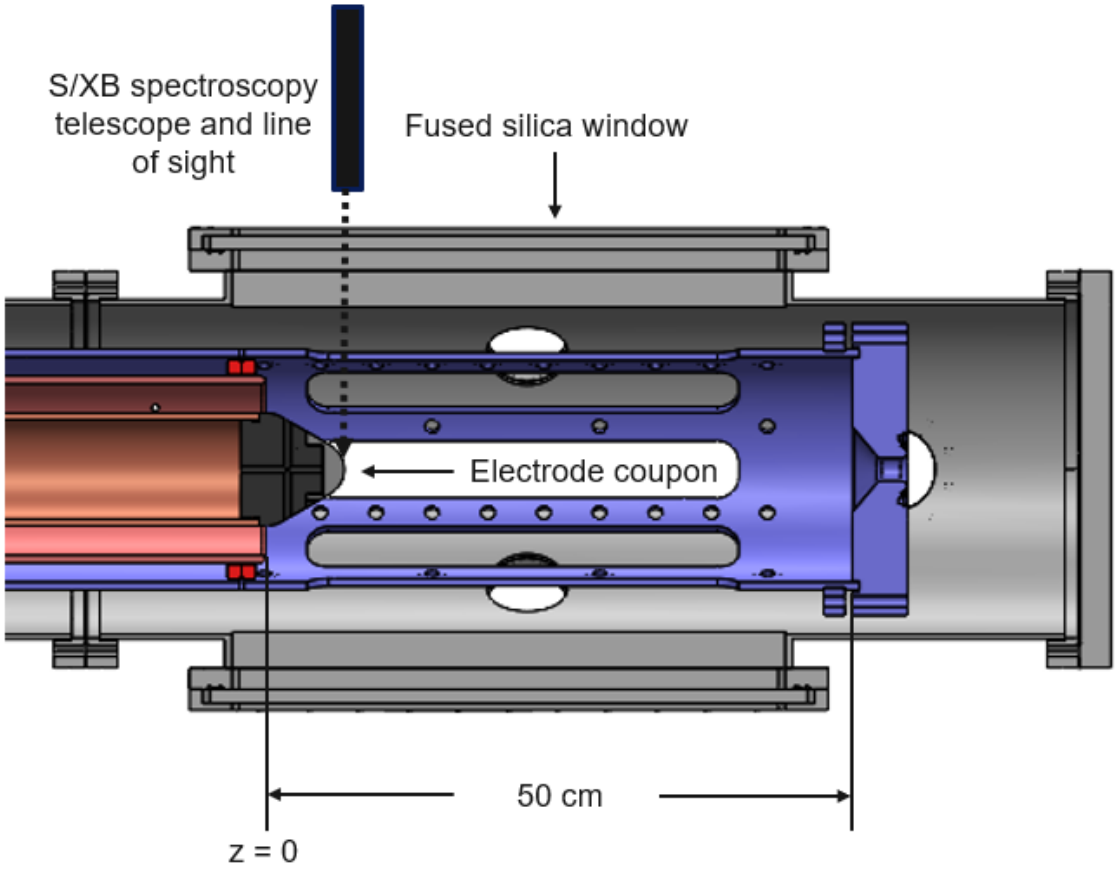

Figure 4.2: Modifications to ZaP-HD placed the nose cone further downstream, making it visible through the electrode slots when viewing perpendicular to the device axis. This provides optical access to the electrode nose cone. The radial telescope is shown with a direct line of sight viewing the electrode from the upper window.

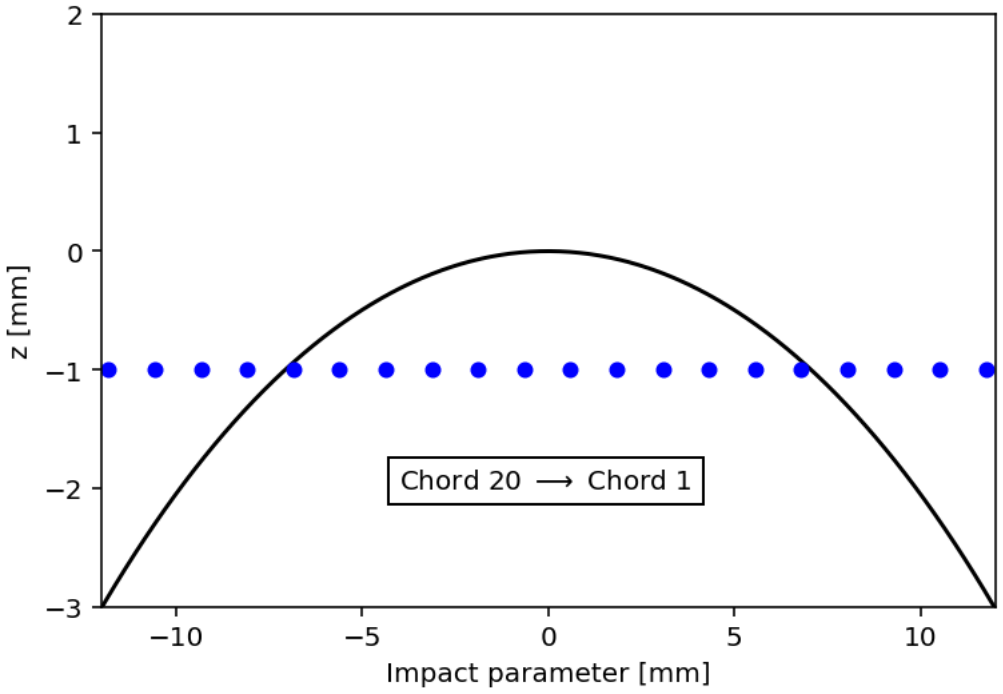

Figure 4.3: Impact parameters of the 20 spectroscopy chords on the electrode nose cone profile. Plasma flows downstream in the positive z direction. The central axis of ZaP-HD is along $x = 0$. The measurement chords span a total of 23.6 mm across the nose cone. All but the four outer chords on either side of the array have a line of sight which terminates on the electrode surface.

4.2.2 Absolute Irradiance Calibration

The S/XB method requires measurement of the photon flux of C-III. To achieve this, the absolute spectral response of the system was calibrated to a light source that outputs a known quantity of light at the desired wavelength. The intensity measured during the experiment was then converted to a photon flux. This calibration was performed individually for all 20 chords in order to account for transmission losses along each optical path. Calibration was done using an Ocean Optics DH-3 Plus light source, which delivers a spectral irradiance of 6.35 μW/cm^2/nm at 229.7 nm. The light source output was cosine-corrected with the CC-3-UV-T diffusive element to ensure isotropic emission. Figure 4.4 shows a schematic of the calibration setup. The distance between the light source and the telescope lens replicates the distance between the electrode and the telescope when installed on ZaP-HD. The light source was translated across the optical axis until the intensity was maximized at each of the 20 chords. An acquisition was obtained on the ICCD at each of these positions, which were combined into a single spectrum. The maximum ICCD exposure time of 21 seconds was necessary to gather sufficient light intensity. The signals from each chord were binned and averaged in a similar manner to previous spectroscopy applications [90, 73, 74]. For each chord, the intensity variation with wavelength was fitted with a cubic function. The function's value at 229.7 nm gives the counts corresponding to the absolute irradiance of the light source at that wavelength. This is illustrated in Fig. 4.5 for chord 10. The resulting calibration data is an array of 20 values for the counts that correspond to the known irradiance output of the light source.

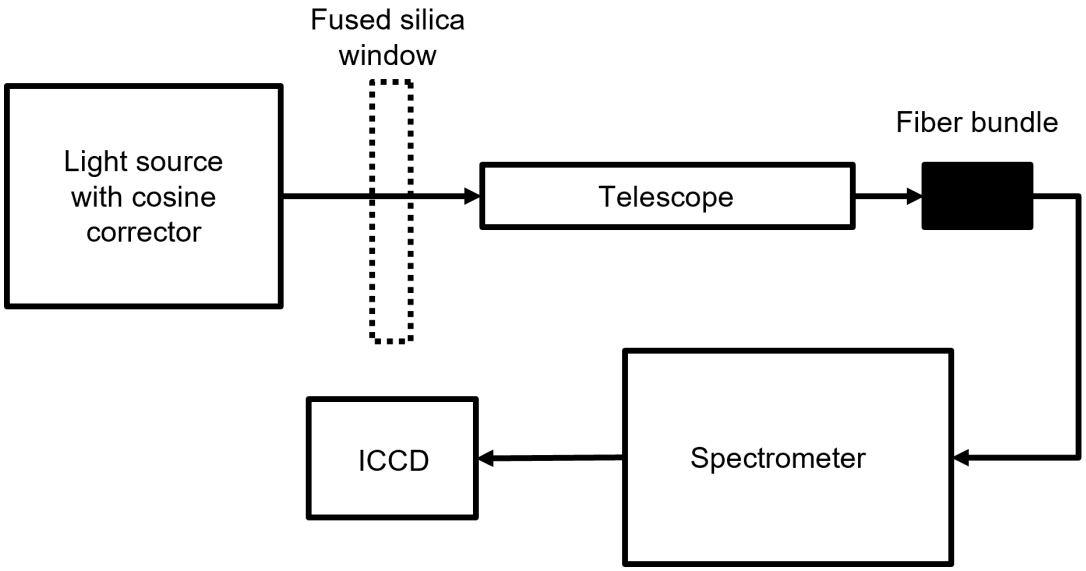

Figure 4.4: Absolute calibration setup for S/XB measurements. The output of the light source passes through a fused silica window and is focused by a telecentric telescope onto a 20-chord fiber bundle. The distance from the telescope lens to the light source replicates the distance on the experiment to the Z-pinch plasma. The absolute intensity response of the system is recorded on the ICCD for the known output of the light source.

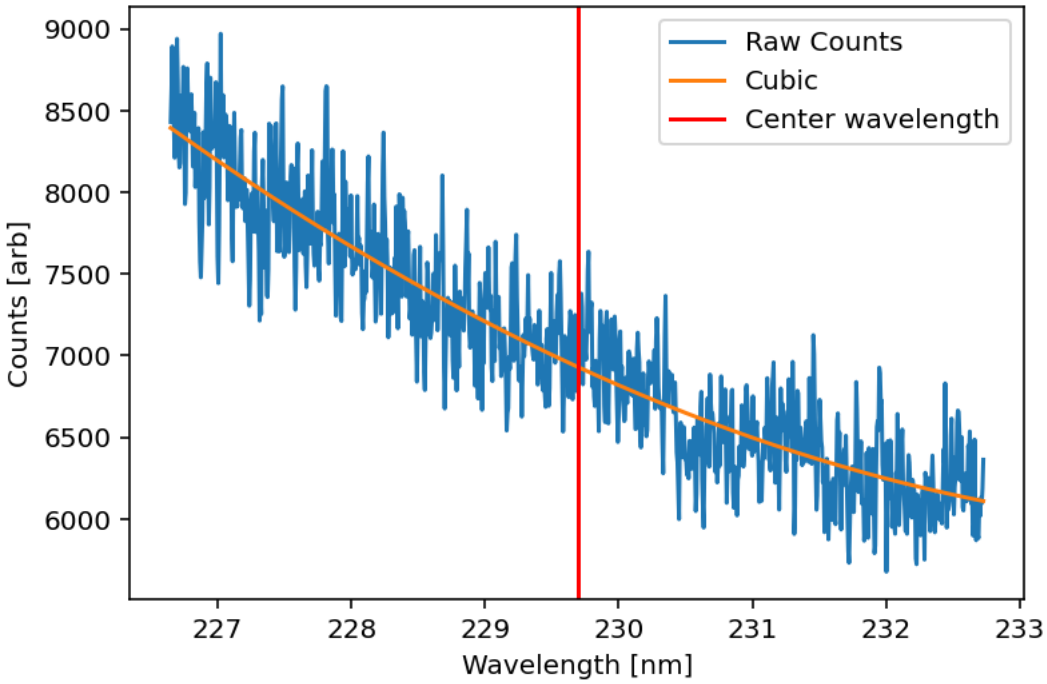

Figure 4.5: Calibration light source intensity centered at 229.7 nm for chord 10. A cubic function was used to fit the intensity data. The value of the cubic function at the center wavelength is the intensity in arbitrary counts corresponding to the known absolute irradiance output of the light source.

4.2.3 Calculation of the photon flux

During operation of the ZaP-HD experiment, the intensity of the C-III emission was recorded over a gate duration of 15 ns. Using the intensity values obtained in the calibration, the absolute irradiance measured during the experiment can be calculated with the expression

$$E_{exp} = (\frac{C_{exp}}{\tau_{exp}})(\frac{\tau_{cal}}{C_{cal}})E_{cal}, \tag{4.19}$$

where the symbol E denotes the absolute irradiance, C is the recorded emission intensity in counts, and τ is the gate duration of the ICCD acquisition. The subscript *exp* denotes quantities measured during operation of the ZaP-HD experiment, and the subscript *cal* is for values obtained during calibration. To calculate the photon flux, E_{exp} is divided by the photon energy,

$$I = \frac{E_{exp}}{hc}\lambda, \tag{4.20}$$

where h is the Planck constant, c is the speed of light, and λ is 229.7 nm.

4.2.4 Applying plasma parameter profiles for S/XB coefficient selection

Appropriate selection of the S/XB coefficient is made difficult by the rapidly changing plasma parameters near the electrode, and by the limitations in diagnostic measurements of those plasma parameters. On ZaP-HD, the electron density and temperature of the plasma are obtained by DHI measurements, described in Sec. 3.2.4, which provide radial profiles of the density and temperature over a span of axial locations at a single point in time. The profiles are interpolated to extract a particular density and temperature value at the position of the chords as shown in Fig. 4.3. Interpolation of the dataset in Fig. 4.1 at these plasma parameters gives the corresponding S/XB coefficients. Profiles of the number density obtained from DHI measurements

are shown in Fig. 4.6(a) for the axial location $z = 8$ cm in the assembly region. The number density peaks on axis at 2×10^{23} m^{-3}.

The electron temperature plotted in Fig. 4.6(b) is obtained by the equilibrium analysis described in Ref. [1]. An abbreviated procedure is provided here. The Z-pinch plasma current is calculated by integrating Ampère's Law and incorporating magnetic field probe data at the axial location of the density measurement. The magnetic field profile is then calculated by integrating the electron number density profile. The magnetic field profile is used in the integration of the radial force balance equation, Eq. 1.2, to calculate the electron temperature profile. The integration is carried out to the pinch radius a, beyond which the electron temperature drops to zero. The electron temperature peaks on axis at 670 eV. The characteristic radius $a = 3$ mm from Ref. [1] is maintained. It is important to note that the DHI measurements provide profiles of the Z-pinch plasma column, while the S/XB measurements are taken where the plasma contacts the electrode. This contact forces the plasma outward along the electrode, which expands the plasma parameter profiles. Therefore, direct application of the density profile from DHI should be interpreted as the upper limit of the plasma parameters used to determine the S/XB coefficients. Modification of this density profile to account for this expansion will be discussed in Sec. 4.3.1.

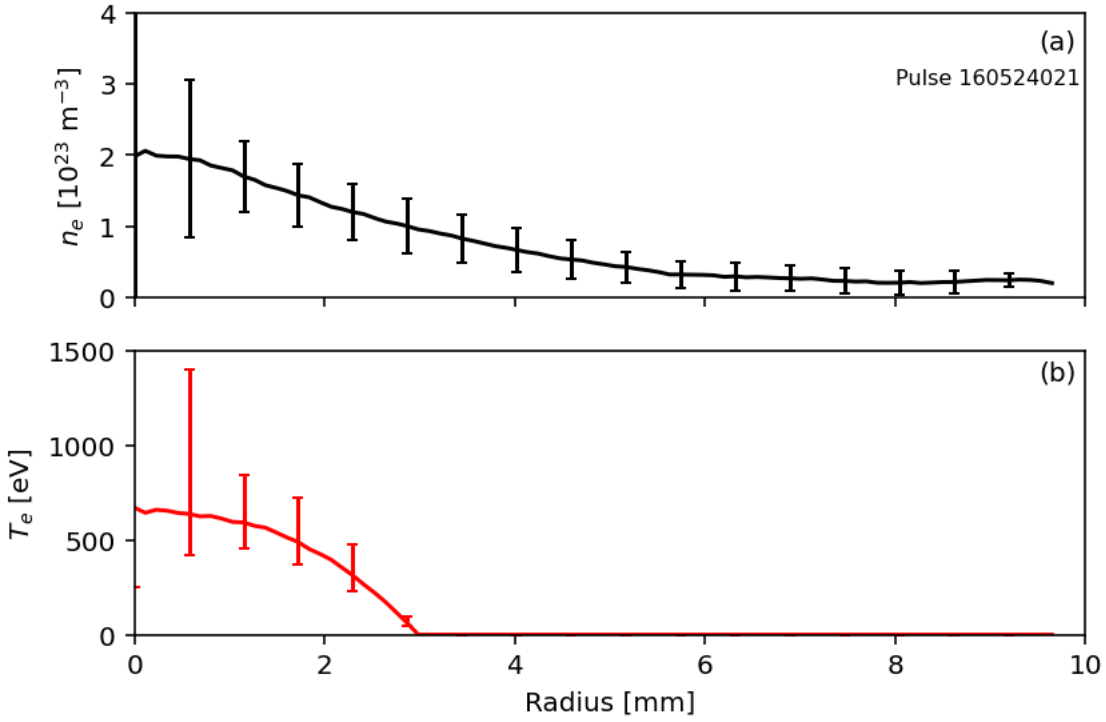

Figure 4.6: Radial profiles of the (a) electron number density and (b) electron temperature calculated from density values by applying the Z-pinch equilibrium analysis described in Ref. [1]. Number density measurements are obtained from interferometry [5]. This analysis uses the characteristic pinch radius of 3 mm, beyond which the electron temperature goes to zero. Error bars are shown at sample locations.

4.2.5 Error quantification

The error bars for the number density plotted in Fig. 4.6(a) correspond to the difference between assumed and reconstructed line-integrated density profiles that have been propagated through the same Abel inversion process that provides the number density values. This process is described in further detail in Ref. [5]. To propagate the uncertainty in number density, δ_n, to the electron temperature, the upper and lower limit of the density defined by the error bars is propagated through the analysis described in Sec. 4.2.4. The error bars in Fig. 4.6(b) represent the difference between these propagated temperature profiles. The range in the S/XB coefficients is then found by interpolation of the data set in Fig. 4.1 for the values of the upper and lower density and temperature profiles to give the uncertainty of the coefficients, δ_{SXB}. The other source of uncertainty in the flux measurement is from the emission intensity, which is assumed to follow Poisson statistics. The uncertainty in the counts is therefore $\delta_C = \sqrt{C_{exp}}$, which is propagated through Eqs. 4.19 and 4.20 to obtain the uncertainty in the photon flux, δ_I. The overall uncertainty in the eroded flux measurement, δ_Γ, is calculated with

$$\frac{\delta_\Gamma}{\Gamma} = \sqrt{\left(\frac{\delta_{SXB}}{S/XB}\right)^2 + \left(\frac{\delta_I}{I}\right)^2}. \tag{4.21}$$

4.3 Erosion Measurements

The S/XB diagnostic recorded C-III emission from the graphite electrode for pure hydrogen Z-pinch plasmas. A raw spectrum showing the emission captured at 229.7 nm is shown in Fig. 4.7. The solid line is positioned at 229.7 nm for reference. The spatial position corresponds to the x dimension in Fig. 4.3. The ICCD was triggered at 50 μs to capture C-III emission coincident with the peak pinch current, and therefore the peak density and temperature. This timing also aligns with the DHI measurement.

The intensity of emission required a gate width of 15 ns to avoid saturation of the sensor. The emission intensity decreases close to the axis where the chords terminate on the electrode, while more C-III emission is captured along the outer chords that have a longer line of sight. This supports the use of the outer chords as a background subtraction described in Sec. 4.2.1 to isolate the C-III emission local to the surface.

Carrying out the data processing results in the inferred carbon erosion fluxes shown in Fig. 4.8. Values of the flux are only calculated for chord positions within the pinch radius of 3 mm, which have a non-zero electron temperature according to the profile specified in Fig. 4.6(b). The vertical dotted lines indicate the edge of the electrode surface. The peak eroded flux is 9.7 $\times$ 10^{30} atoms $m^{-2}s^{-1}$ at -0.6 mm offset from the experiment axis (chord 11). However, the error bars indicate that the peak may occur further off-axis at 2 mm. Large errors in the eroded flux closer to the axis is likely due to corresponding large errors in density and temperature as shown in Fig. 4.6.

4.3.1 Expanded density profiles for S/XB calculations

The results shown in Fig. 4.8 apply the measured profiles of the core plasma to the S/XB measurement locations on the electrode. In reality, the geometry of the electrode forces the plasma outwards at the location of the S/XB measurement. For a constant linear density, the profiles should expand, reducing the density at the electrode. At present, local measurements of the plasma parameters on the electrode are not available on ZaP-HD. However, the measured profiles from DHI can be modified to account for this expansion. The Z-pinch mass, and therefore the linear density, is held constant, and the expanded profile redistributes the conserved mass. To implement this, the number density measured by DHI in Fig. 4.6(a) is integrated using Eq. 1.7 to give the linear density N. Using the electrode radius as the lower limit of

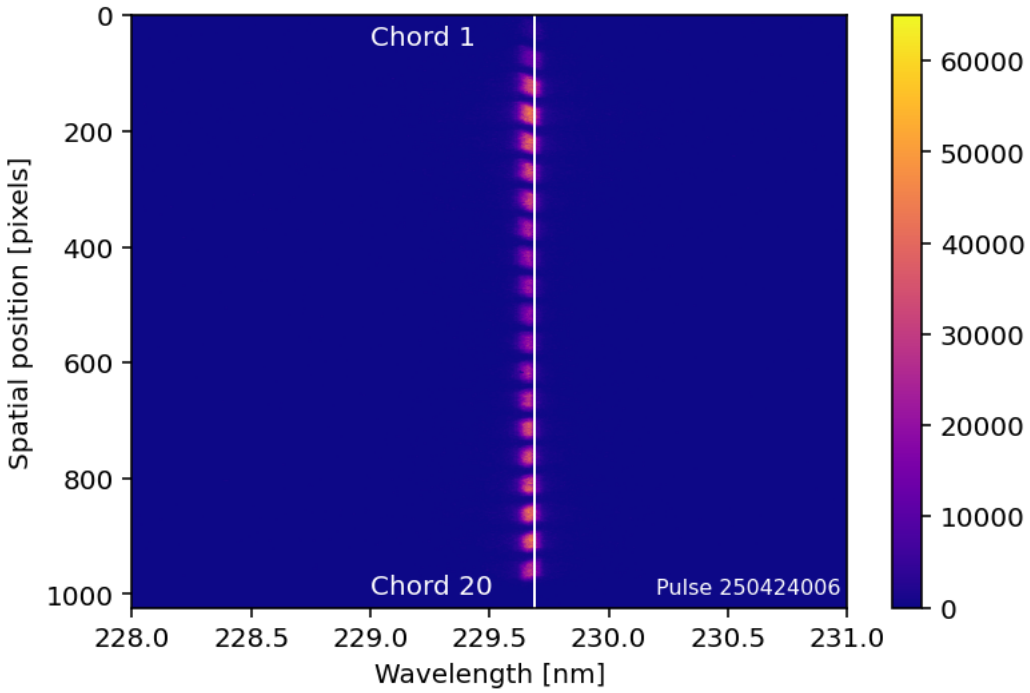

Figure 4.7: Chord-integrated line emission of C-III at 229.7 nm. The central chords, which terminate on the electrode, record a lower intensity compared to the outer chords. The solid line is positioned at 229.7 nm for reference. The 20 chords are arranged as shown in Fig. 4.3, with the telescope orientation as shown in Fig. 4.2.

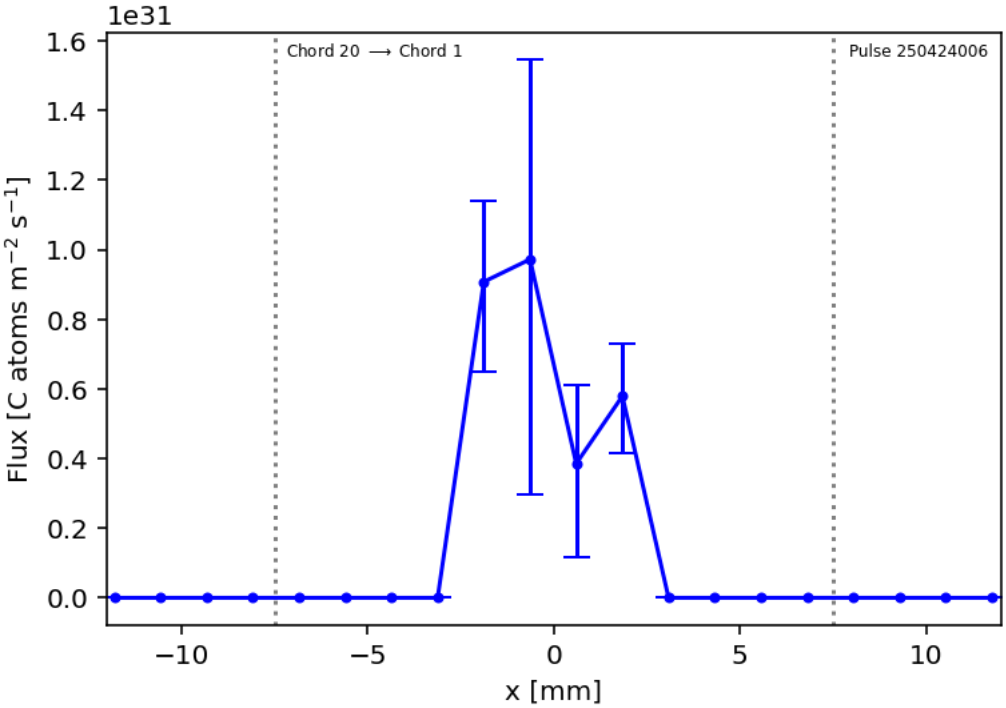

Figure 4.8: The eroded flux of carbon atoms as measured by the S/XB spectroscopy diagnostic. The S/XB coefficients at each impact parameter x are determined using the radial density and temperature profiles shown in Fig. 4.6. Beyond the assumed pinch radius of 3 mm, the electron temperature profile drops to zero, therefore S/XB coefficients are only assigned to the central four chords for calculation of the eroded flux.

integration and imposing an equality for the linear density,

$$N = \int_0^\infty 2\pi n_1(r) r dr = \int_{r_{nc}}^\infty 2\pi n_2(r) r dr, \tag{4.22}$$

where n_1 is the original number density profile, n_2 is the expanded number density profile, and r_{nc} is the radius of the electrode on the nose cone where the S/XB measurement is taken. The calculated linear density is $N = 1.26 \times 10^{19}$ m^{-1}. A comparison of the profiles is illustrated in Fig. 4.9. The original density profile n_1 is shown in black. A Lorentzian fit provides a good approximation of n_1, shown in blue. Therefore, a Lorentzian is used to generate the expanded profile, shown in green, with amplitude and width parameters such that the linear density N is conserved. The expanded profile starts at $r_{nc} = 7$ mm, shown as a dotted gray line. Applying the same equilibrium analysis from Ref. [1] gives the electron temperature, illustrated along with the expanded density profile in Fig. 4.10. The radius of $a = 3$ mm has been maintained. The peak density of the expanded profile decreases to 4.2×10^{22} m^{-3}, while the peak electron temperature decreases to 145 eV. The error bars are calculated by performing the same expansion procedure on density profiles defined by the error bars of the original profiles. For the same linear density, a reduced number density and temperature correspond to a reduced pinch current as shown by the scaling relations [16, 1, 18] from Sec. 1.2.

This model of constant linear density does not take into account any effects of the plasma flow or of the electrode resistance. For instance, in the case of a positive radial shear of the axial velocity as expressed in Eq. 1.9, plasma that contacts the electrode and is forced radially outward will encounter a region of plasma moving at higher velocity in the downstream direction. The reduction in current density and magnetic field strength of this expanded plasma suggests that it may be more susceptible to perturbations from the flowing plasma, which would alter the plasma parameters. Furthermore, the resistance of the electrode will affect the behavior of the current

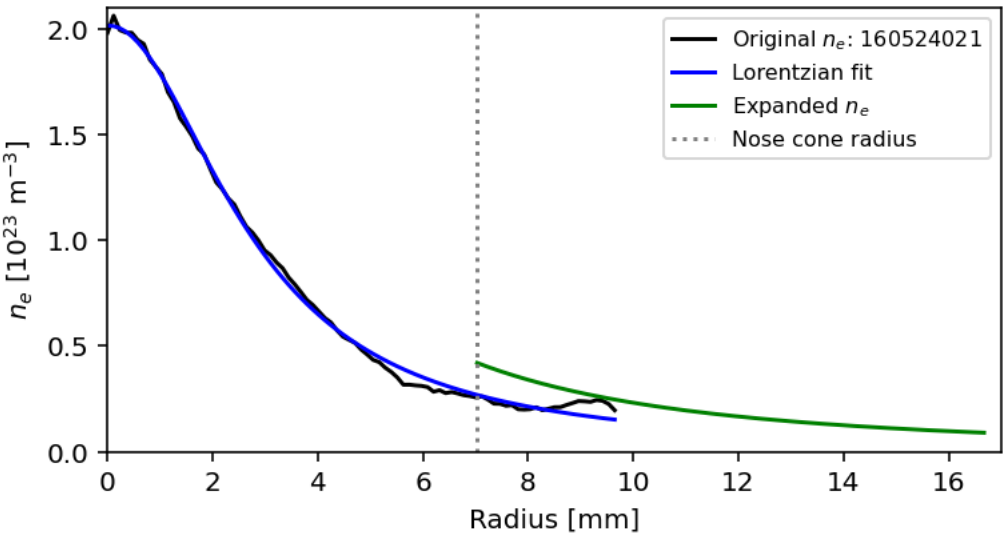

Figure 4.9: Original (black) and expanded (green) electron number density profiles using data from DHI. A Lorentzian fit (blue) is used to approximate the original profile and to generate the expanded profile. The linear density of both profiles is conserved according to Eq. 4.22. The dotted gray line represents the electrode radius at the nose cone. The peak density is reduced by a factor of four in the expanded profile.

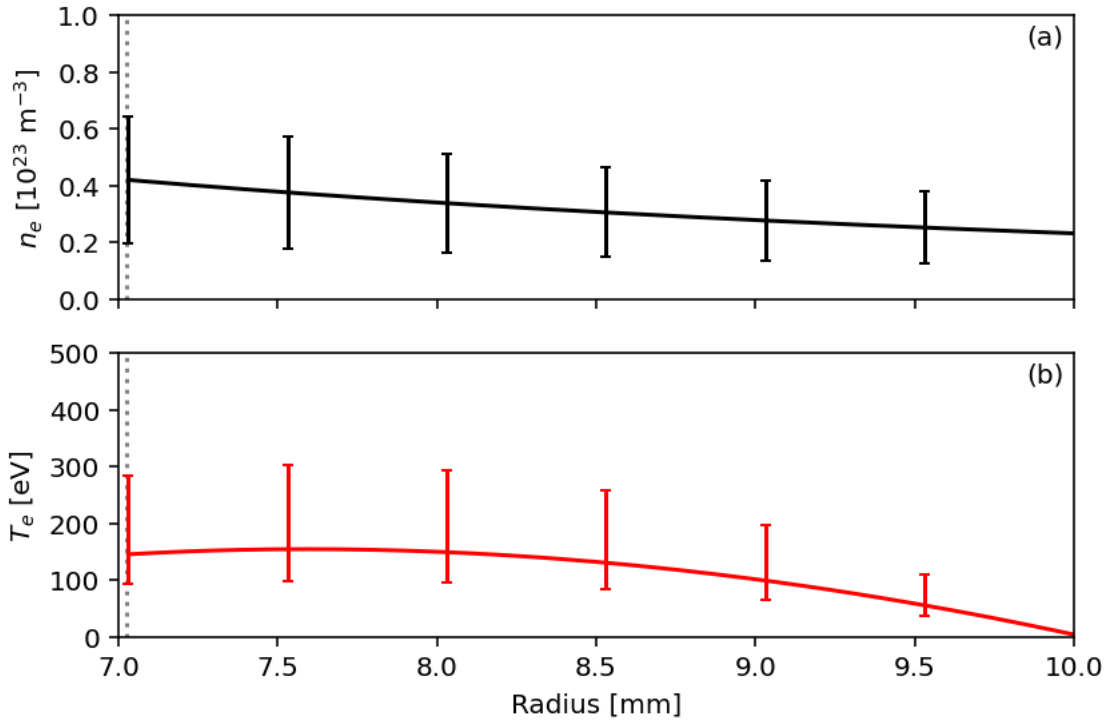

Figure 4.10: Expanded radial profiles of the (a) electron number density and (b) electron temperature, based on original profiles in Fig. 4.6. Expanded profiles begin at the radius of the electrode at the nose cone, shown as the dotted gray line, which accounts for plasma contact with the electrode. The peak electron temperature is reduced by about a factor of five compared to the original profile, to 145 eV.

attachment, causing deviations from the expansion described by simply conserving the linear density. These effects merit further investigation for a more comprehensive model of the plasma in contact with the electrode, however they are assumed to be negligible for the analysis presented in this dissertation.

To calculate the erosion flux with the expanded profile, the S/XB coefficients are found using the density and temperature values at r_{nc} since each chord terminates on the nose cone at the same radius. The results are plotted in Fig. 4.11. The peak erosion flux is approximately a factor of four smaller than that calculated with the original profiles, decreasing to 2.4×10^{30} atoms $m^{-2}s^{-1}$. In Chapter 6, the measured values of the carbon erosion flux are compared to the theoretical values for physical sputtering and sublimation of carbon in order to evaluate the relevance of these specific erosion processes.

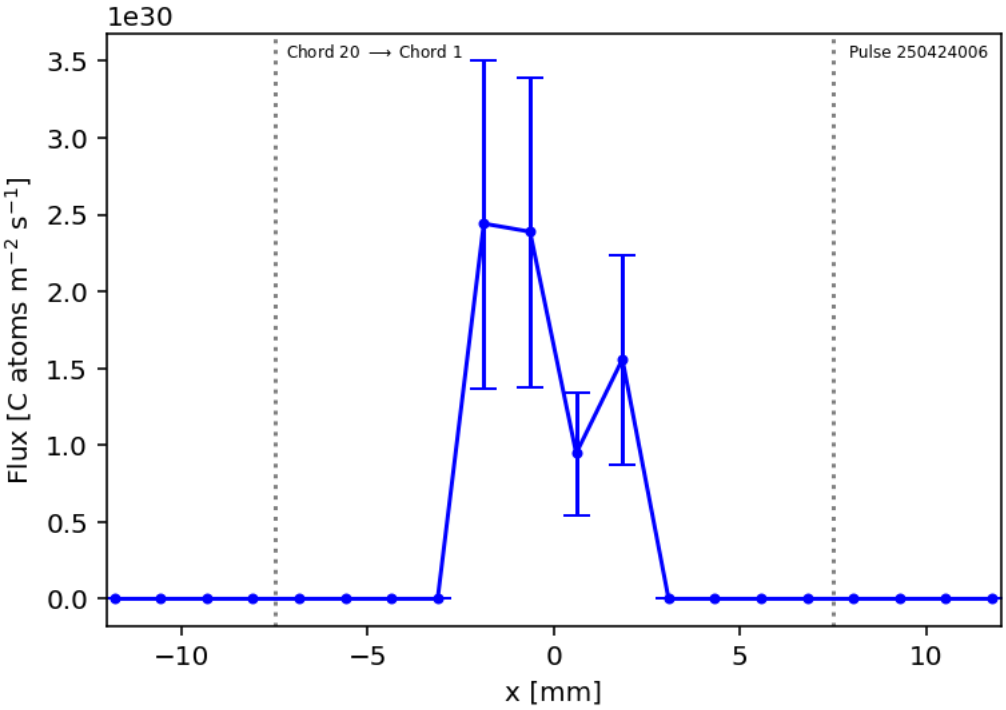

Figure 4.11: The eroded flux of carbon atoms as measured by the S/XB spectroscopy diagnostic. The S/XB coefficients at each impact parameter x are determined using the expanded radial density and temperature profiles from Fig. 4.10. Fluxes are reduced by about a factor of four compared to those calculated using the profiles in Fig. 4.6.

Chapter 5
TWO-COLOR PYROMETRY

A pyrometer is a device that measures the temperature of an object from a distance by sensing the emitted thermal radiation. This remote sensing capability is essential for monitoring extreme temperatures that would destroy contact sensors such as thermocouples or thermistors, or for environments that preclude the use of contact sensors, such as molten metal in furnaces, gases in turbine engines, or objects in motion. On ZaP-HD, the placement of a thermocouple on the electrode would result in melting of the probe, as well as perturbation of the plasma and discharge current path. Evidence of molten tungsten was observed on the graphite samples from the study by Forbes [72], as well as by droplet formation on the original metallic nose cone on ZaP-HD [80]. This implies electrode surface temperatures up to 3700 K, the melting point of elemental tungsten. In the case of a graphite electrode, sublimation occurs at 3900 K at standard pressure [92]. Such extreme temperatures necessitate the use of a remote temperature diagnostic such as pyrometry. Surface temperature measurements also permit calculation of the heat flux to the cathode, an important metric with regard to the power handling capability of the electrodes. This chapter describes the theory and implementation of two-color pyrometry measurements on ZaP-HD.

5.1 Theory

Any object that has a temperature above absolute zero will emit electromagnetic radiation, also known as thermal radiation. In the idealized case, an object that

absorbs all wavelengths of incident radiation and is in thermal equilibrium with its surroundings is known as a black body. An ideal black body has a characteristic spectrum of thermal radiation that depends only on the temperature of the object. This thermal radiation can be related to the body's temperature via Planck's Law:

$$B(\lambda, T) = \frac{8\pi hc}{\lambda^5} \frac{1}{e^{\frac{hc}{\lambda k_B T}} - 1}. \tag{5.1}$$

The quantity B is the spectral radiance in units of power per unit area, per unit solid angle, and per unit wavelength [W $m^{-2}sr^{-1}nm^{-1}$], h is Planck's constant, λ is the radiation wavelength, and c is the speed of light. Planck's Law is plotted for several temperatures in Fig. 5.1.

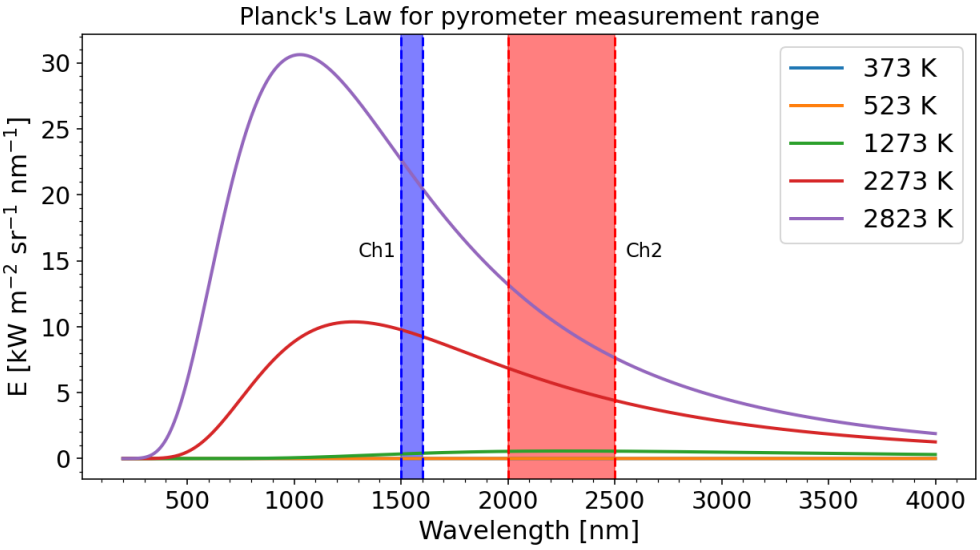

Figure 5.1: Spectral variation of black body radiation described by Planck's Law for selected temperatures. As the temperature increases, the peak radiation shifts to shorter wavelengths. The blue and red shaded regions indicate the wavelength ranges used by the IGAR6 pyrometer channels in two-color mode.

As the temperature of a body increases, the wavelength at the peak of the spectrum

shifts to shorter wavelengths and increases in radiation intensity. This shift is given by Wien's displacement law:

$$\lambda_{max} = \frac{b}{T}. \tag{5.2}$$

The constant b is known as Wien's displacement constant, which has a value of $b = 2897.8$ μm K. According to Eq. 5.2, objects at room temperature, 25 °C, emit their maximum thermal radiation at 9660 nm, deep in the infrared (IR) region and therefore invisible to the human eye. The black-body spectrum for an object at 2000 °C peaks closer to 1200 nm, which in the near infrared (NIR) range. However, a significant portion of the spectrum is also emitting in the visible range, specifically in the longer red wavelengths. This phenomenon is why a heated piece of metal will eventually glow red with increasing temperature as the peak emission shifts from NIR to the red portion of the visible spectrum. With further heating, the emission turns red-orange as the wavelengths continue to shorten, and at even higher temperatures will appear white as many different visible wavelengths contribute to the emitted spectrum. By assuming the target object is emitting a black-body spectrum, measuring the emitted radiation power at a specific wavelength allows calculation of the temperature by applying Planck's Law. Integration of Planck's Law over the frequency, $\frac{c}{\lambda}$, and the solid angle Ω, results in the Stefan-Boltzmann Law,

$$\frac{P}{A} = \epsilon \sigma T^4, \tag{5.3}$$

which relates the emitted power per unit area to the fourth power of the temperature. This is a useful direct method for calculation of the surface temperature, if the emissivity ϵ is known. The emissivity is a material property that describes how closely an object approaches the ideal black-body emission behavior. It is a ratio between 0 and 1 of the object's thermal radiation emission and the emission of an ideal black body. Emissivity can vary with temperature and emitted wavelength, and may itself change

due to changes in the material surface. This makes the application of the Stefan-Boltzmann law challenging if the emissivity is not precisely known for the conditions of the measurement. Any signal attenuation through intervening media such as a gas or view port material will also result in an incorrect measurement. Alternatively, if the intensities of two spectral wavelengths are recorded, and their ratio related to the surface temperature, then the effects of emissivity and signal attenuation can be negated. This is the basis for the ratio, or two-color pyrometer. Adapting the analysis from Ref. [93], an expression for the intensity of measured thermal radiation can be derived from Eq. 5.1:

$$I_n(T) = \frac{K_n \epsilon_n}{\lambda_n^5 e^{\frac{hc}{k_B \lambda_n T}}}. \tag{5.4}$$

Here, n represents either the first or second wavelength in the two-color configuration. I_n is the measured intensity, and K is a constant specific to the pyrometer design, optics, geometry, and sensitivity that is obtained through calibration with a reference blackbody at known temperature [94]. The emissivity is ϵ_n, wavelength is λ, Planck constant is h, speed of light is c, the Boltzmann constant is k_B, and surface temperature is T. Next, the ratio of Eq. 5.4 for both wavelengths is defined as R:

$$R \equiv \frac{I_1}{I_2}. \tag{5.5}$$

Designating the measured ratio temperature as T_R, a relationship with R is derived [93]:

$$T_R = \left(\frac{\ln(R) - \ln(\epsilon_1/\epsilon_2) - \ln(K_1 \lambda_2^5 / K_2 \lambda_1^5)}{(hc/k_B)(\lambda_2^{-1} - \lambda_1^{-1})} \right)^{-1}. \tag{5.6}$$

Assuming that the change in emissivity is negligible over the duration of measurement, change in temperature, and between the two wavelengths being recorded, the two emissivity terms can be made equal, $\epsilon_1 = \epsilon_2$, which removes the natural logarithm term from Eq. 5.6.

5.2 Implementation on ZaP-HD

Measurements of the graphite electrode surface temperature on ZaP-HD were made with the Advanced Energy IMPAC IGAR6 SMART two-color pyrometer. This device is able to operate in both single-color and two-color modes, with a combined temperature sensitivity range of $100 - 2550$ °C, equivalent to $373 - 2823$ K. The two-color mode has a minimum temperature sensitivity of 250 °C. Figure 5.2 shows the general layout of the pyrometer and a line of sight measurement at the nose cone tip. The pyrometer is mounted to a translation stage on the optical table next to the ZaP-HD experiment, and views the electrode through one of the rectangular fused silica windows. The vertical position of the pyrometer is aligned to the mid-plane of the electrode. The pyrometer is equipped with an alignment laser and adjustable focal length that can be set to the appropriate distance to the point of measurement. The pyrometer is located approximately 1000 mm from the central axis of the electrode, which results in a spot size on the electrode roughly 1 cm in diameter.

The wavelength ranges recorded by each channel in two-color mode are $1500 - 1600$ nm and $2000 - 2500$ nm respectively. These ranges are highlighted in Fig. 5.1 for the range of measurable temperatures by the IGAR6 pyrometer. Transmission of IR wavelengths through fused silica does decrease below 90% for wavelengths between 2200 and 2300 nm and above 2500 nm. The transmission is as low as 62% at 2200 nm. This represents a significant portion of the longer wavelength range of the IGAR6 pyrometer, and may contribute to the limitations observed in the resulting temperature measurements.

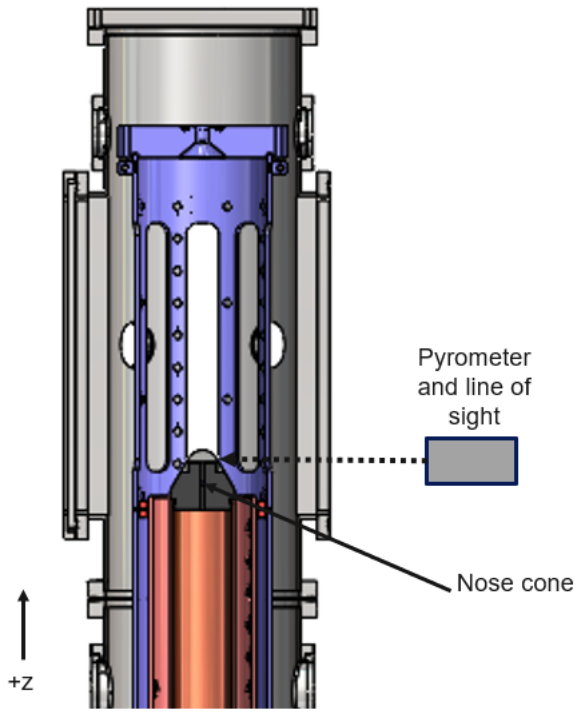

Figure 5.2: Top-down section view of the ZaP-HD Assembly Region. The IGAR 6 two-color pyrometer measures the graphite electrode surface temperature through the side fused silica window. The pyrometer is mounted to a translation stage allowing measurements at different z locations.

Data acquisition from the pyrometer is achieved by two methods. The first uses the manufacturer-provided software which continuously collects data while the pyrometer is connected to the operating computer. However, this collection method can only record one data point every 32 ms. This is useful for monitoring temperatures in between pulses, which are intervals of several minutes. The second method enables data acquisition at the maximum pyrometer response time of 2 ms. The IGAR6 has a $0 - 10$ mA analog output that is digitized by an MDO3014 osilloscope. A 510 Ω resistor is placed across the current output terminals, and the voltage across this resistor is recorded by the oscilloscope. This converts the current output to a voltage measurement with a corresponding range of $0 - 10$ V. The pyrometer temperature calibration is provided in terms of this analog output current, I_{out}, as

$$T_1 = 122.5 * I_{out} + 100 \tag{5.7}$$

for the single-color mode and

$$T_2 = 115 * I_{out} + 250 \tag{5.8}$$

for the two-color mode, with I_{out} in mA units. In order to apply the calibration, the voltage recorded on the oscilloscope, V_{out}, is converted to the current output I_{out} by applying Ohm's Law with the appropriate unit conversion,

$$I_{out} = 0.001 * V_{out}/R, \tag{5.9}$$

where R = 510 Ω.

5.3 Electrode Surface Temperature Measurements

The oscilloscope measurement is triggered simultaneously with the ZaP-HD pulse and set to record 10,000 samples at a sample frequency of 1 MS/s. This provides data points every microsecond for a total duration of 10 ms. An example of the recorded

trace for one pulse is shown in Fig. 5.3. This measurement was made at the tip of the nose cone as shown in Fig. 5.2. The $t = 0$ trigger is shown as the vertical dashed line, marking the start of the pulse. As described in Sec. 3.3, the first capacitor bank is discharged 2 μs after $t = 0$, and the second capacitor bank is discharged 20 μs later. These discharges are evident as large spikes in the recorded pyrometer signal between 0 and 0.5 ms. The oscilloscope is likely picking up some capacitive or inductive signal generated by the ZaP-HD pulse. Regardless, since the response time of the pyrometer itself is only 2 ms, the temperature during the pulse is unable to be resolved. These spikes are still observed when the pyrometer is blocked during a plasma pulse, which confirms their association with the firing of the discharge circuit. This also indicates that the pyrometer signal observed after the duration of the pulse can be attributed to measurement of thermal radiation.

The signal in Fig. 5.3 shows a linear rise that reaches a plateau just before 2 ms. Since this linear rise occurs before the response time of the pyrometer, this region is not considered a temperature measurement. Rather, it may be associated with the internal photodiode amplification circuit. At the plateau, the temperature is constant for roughly half a millisecond before a rapid drop to the threshold temperature of 250 °C. This sudden decrease may be explained by a loss in signal in one or both of the two wavelength channels, which prevents processing of the signal ratio. Loss of signal can occur due to a sufficiently large change in the emissivity of the graphite surface. As described by Eq. 5.6, the two-color method relies on the emissivity of both channels remaining close enough such that the natural logarithm term is effectively zero. The two-color method remains valid for changes in the emissivity provided that both channels are affected equally. Graphite emissivity is known to be temperature and wavelength dependent [95, 96]. In addition, erosion processes such as sublimation and sputtering can significantly change the surface roughness, which can also change

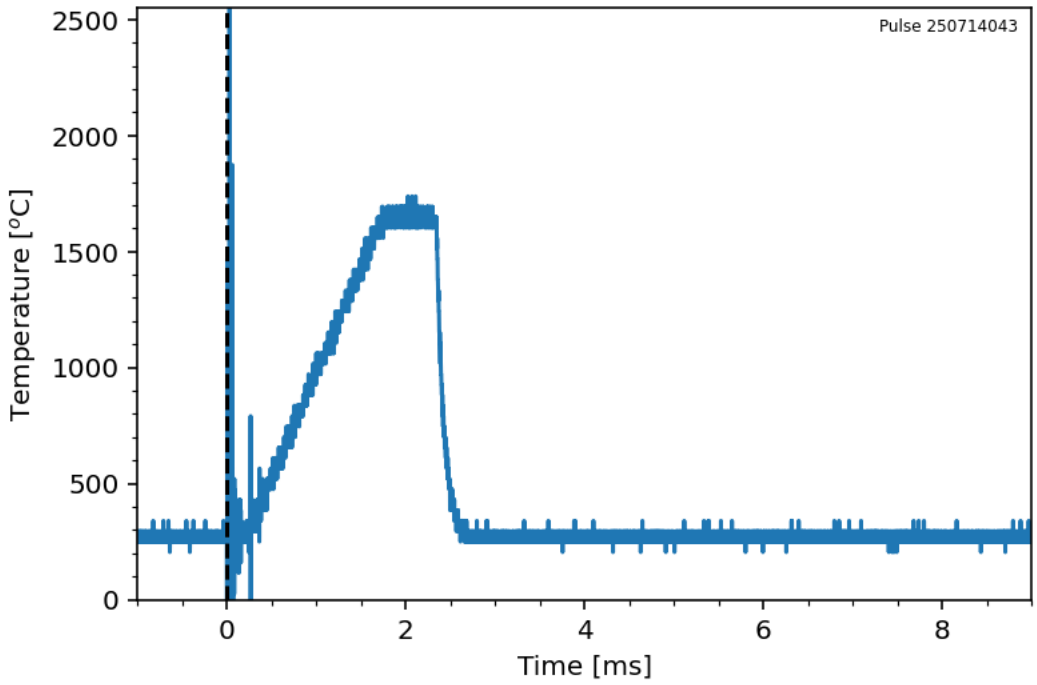

Figure 5.3: Time-resolved response of the two-color pyrometer measuring the surface temperature at the tip of the graphite nose cone. The experiment trigger occurs at the vertical dashed line. Immediately after the trigger, large oscillations in the pyrometer signal are observed which coincide with the duration of the ZaP-HD pulse. The two-color signal rises to a plateau just before 2 ms at 1670 °C, then drops to the threshold of 250 °C within a millisecond.

the surface emissivity [95]. The peak temperature observed in Fig. 5.3 is 1670 °C during the signal plateau, which is well below the sublimation point of graphite. Because this recorded temperature is not close to the 2550 °C maximum detectable temperature or the 250 °C minimum temperature, the reason for the sudden drop in signal is not due to the surface temperature exiting this range, and may be due to factors affecting the emissivity as described previously.

Pyrometer measurements from the continuous acquisition in between pulses provide insight into electrode cooling, shown in Fig. 5.4. This temperature trace includes two ZaP-HD pulses, which appear as the jumps in temperature at 38 and 240 seconds. The pyrometer was operated in single-color mode to lower the threshold temperature to 100 °C. In single-color mode, an emissivity of 1 is assumed by default in the pyrometer software. Due to the much slower time resolution of 32 ms for continuous measurement, the peak amplitudes shown in Fig. 5.4 do not represent the true maximum temperature measurements. The large difference in peak height in this set of two pulses is characteristic of this mode of data acquisition. However, this measurement does capture the long-duration cooling of the electrode in between pulses. This cooling is not observed in two-color mode, which implies that the electrode temperature drops below the two-color threshold of 250 °C rapidly after a pulse. In the roughly three minute interval shown in Fig. 5.4, the electrode temperature decreases to roughly 100 °C after the first pulse. The change in temperature is a decrease of about 10 °C after the jump in the signal. This measurement shows that the electrode, at the localized point of measurement, does retain a significant amount of heat in between pulses, albeit well below the graphite sublimation temperature. If sublimation is occurring, it is likely limited to the duration of time during and possibly immediately after the pulse, on a scale less than 2 ms.

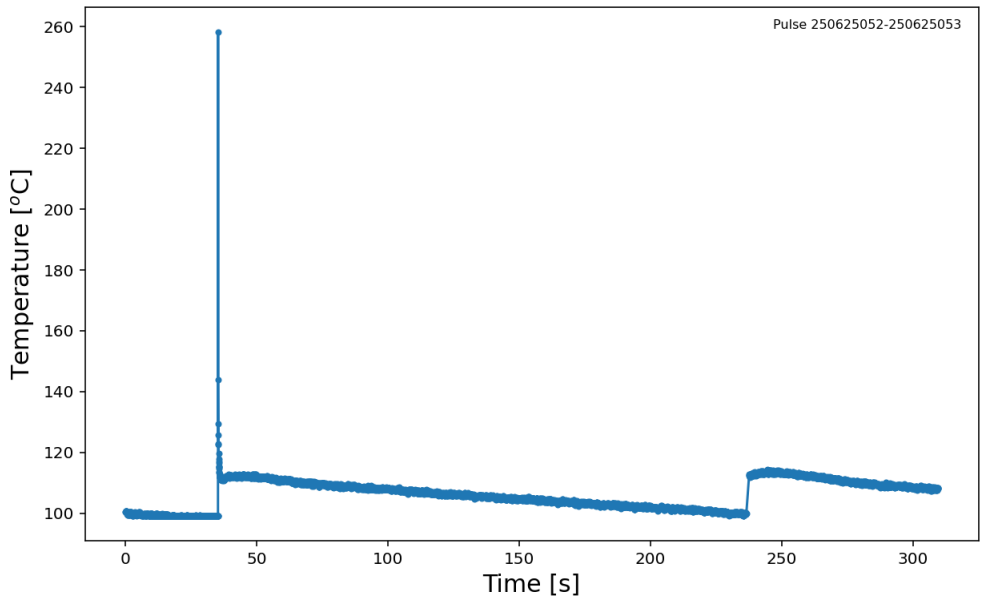

Figure 5.4: Time-resolved measurement of the IGAR6 pyrometer in single-color mode in between ZaP-HD pulses with 32 ms resolution. The pulses are indicated by the sharp jumps in temperature at 38 and 240 seconds. The single-color mode assumes an emissivity of 1 by default. The pyrometer captures cooling of the graphite electrode by about 10 °C over roughly three minutes after the first pulse. The measured temperature is approximately 100 °C at the start of the next pulse. Since this measurement is slow relative to the pulse duration, the true peak temperature is not known.

5.4 Surface Temperature Evolution Using Simplified 1-D Heat Equation

The measurements presented in Sec. 5.3 provide a limited picture of the temperature evolution of the graphite electrode. However, Fig. 5.3 does indicate an elevated surface temperature of 1670 °C, or 1940 K, occurring 2 ms after the start of a pulse. Since the pulse itself only lasts for approximately 100 μs, the electrode is assumed to be cooling after the application of heat flux from the plasma. A simplified model of this situation can be applied to determine whether this observed temperature is realistic at this time scale, given the thermal properties of the graphite and the resulting heat diffusion. For this purpose, the one-dimensional, transient heat equation was applied for the simple case of a 1 mm thick planar wall of graphite. It is assumed that there is no variation of thermal properties with temperature. The partial differential equation is given as

$$\frac{\partial T}{\partial t} = \alpha \frac{\partial^2 T}{\partial x^2}, \tag{5.10}$$

where the temperature T is a function of distance x and time t, and α is the thermal diffusivity defined as

$$\alpha = \frac{k}{\rho c_p}. \tag{5.11}$$

For POCO AXF-5Q graphite, the thermal conductivity is $k = 95$ W/mK, the mass density is $\rho = 1780$ kg/m^3, and the specific heat capacity is $c_p = 710$ J/kgK [97]. The heat equation is solved by applying the finite difference method in a Python script. The resulting spatial and temporal variation of temperature through the 1 mm thick graphite plane is shown in Fig. 5.5. The initial conditions assume that the left side of the graphite plane is facing the plasma and is heated to the sublimation temperature of 3900 K, and the right side of the planar wall is at 100 °C, or 373 K as indicated by the results in Fig. 5.4. The initial temperature distribution is shown as the blue line. Neumann boundary conditions are applied, which specifies the heat flux at the

left and right sides of the plane. The heat flux is calculated in the x-direction with Fourier's Law,

$$q = -k\frac{\partial T}{\partial x}, \tag{5.12}$$

which results in a heat flux of -335 MW/m^2. After the pulse, the left side of the plane simply faces vacuum, where an insulated boundary condition is applied:

$$q_0 = -k\frac{\partial T}{\partial x}(0,t) = 0. \tag{5.13}$$

This assumes that there is no radiative heat transfer. On the right side, the heat flux calculated with Eq. 5.12 is applied at $x = 1$ mm,

$$q_1 = -k\frac{\partial T}{\partial x}(1,t) = -335\,\mathrm{MW/m^2}. \tag{5.14}$$

The purple trace in Fig. 5.5 shows the temperature of the plasma-facing surface of the graphite cools to around 2300 K after 2 ms. While there is some discrepancy of a few hundred degrees to the measurement of 1940 K from Fig. 5.3, this simplified model is reasonably close to the measured temperature. Some of this discrepancy may be accounted for by including the radiative heat loss. This result suggests that the pyrometer measurement obtained before the loss of signal shown in Fig. 5.3 is accurate, which further implies that any graphite sublimation is limited to the duration of the applied heat flux from the plasma.

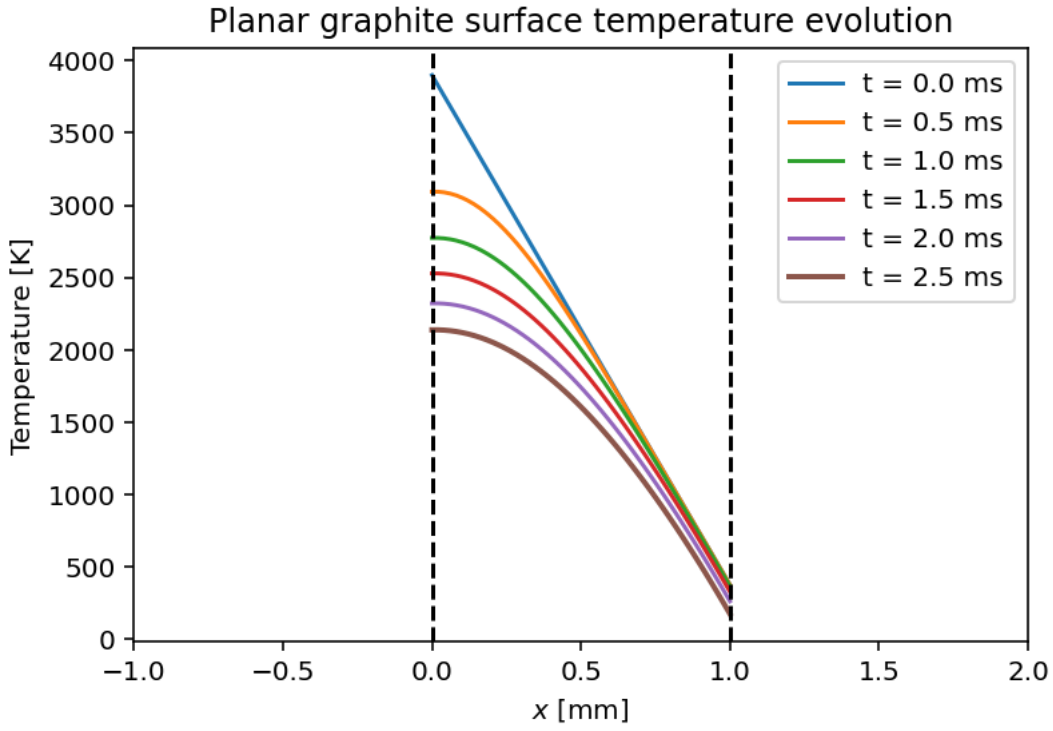

Figure 5.5: Traces of the spatial variation of temperature within a 1 mm thick graphite plane at different times, obtained by solving the one-dimensional transient heat equation and applying thermal properties of POCO AXF-5Q graphite. The initial condition assumes that the left side of the plane has been heated to the graphite sublimation temperature of 3900 K, while the right side of the plane begins at 373 K (100 °C) according to measurements in Fig. 5.4. The model predicts a surface temperature of around 2300 K at 2 ms, which is within the same order of magnitude as the measured temperature in Fig. 5.3. The discrepancy of a few hundred degrees is attributed to the assumption of no radiative heat transfer, but has reasonable agreement with the pyrometer measurement.

Chapter 6

ELECTRODE EROSION MECHANISMS

This chapter compares the measured carbon erosion fluxes to the theoretical values from physical sputtering and sublimation, which provides insight into the physical mechanisms involved in electrode erosion. Physical sputtering arises from the impact of energetic plasma ions on the electrode surface. A neutral carbon atom is sputtered if the energy transferred in the collision exceeds the binding energy between carbon atoms in the solid lattice. Sublimation arises from the absorption of heat which provides sufficient energy for carbon atoms in the lattice to escape as a vapor. Modeling [66] of the electrode response on the FuZE SFS Z-pinch device [35] incorporates both of these processes in its erosion model, and predicts the surface temperature to far exceed the sublimation temperature of graphite.

6.1 Calculating Theoretical Sputtering and Sublimation Fluxes

Since ZaP-HD operates with a hydrogen plasma, H^+ is the dominant ion species. The following calculations assume that incident H^+ ions impact at normal incidence with a sputtering yield of 100%. This provides the upper limit of sputtering that can occur for H^+ ions on carbon. From the analysis in Ref. [1], the assumption of $T_i = T_e = T$ is applied, where $T = 670$ eV from Fig. 4.6(b). The sputtered carbon flux is calculated with the following expression, adapted from Ref. [53]:

$$\Gamma_{sp} = n_e c_s \sin(\alpha) Y^*. \tag{6.1}$$

Here, n_e is the electron number density, and c_s is the sound speed expressed as $[k_B(T_e + T_i)/m_i]^{1/2}$. For normal incidence, $\alpha = 90^o$ and Y^* is the effective yield defined as

$$Y^* = Y_{H^+ \rightarrow C} f_{H^+}, \tag{6.2}$$

where $Y_{H^+ \rightarrow C} = 1$ represents 100% yield for physical sputtering of carbon by hydrogen ions, and f_{H^+} is the fraction of the plasma composed of hydrogen, in this case equal to 1. The sputtered flux is calculated for the same range of n_e and T_e as Fig. 4.1. The resulting values for Γ_{sp} are plotted in Fig. 6.1 for relevant ZaP-HD plasma parameters. The marker indicates the peak value of 7.2×10^{28} atoms $\mathrm{m}^{-2}\mathrm{s}^{-1}$ for conditions on ZaP-HD.

To calculate the sublimation flux of carbon, the entirety of the heat flux from the plasma reaching the electrode surface is assumed to contribute to heating and sublimation. Magnetic field effects, which may reduce the flux to the surface, are neglected. The particle flux at the sheath edge is assumed to be the particle flux at the solid surface. Similarly to the calculation of the sputtered flux, these assumptions provide the upper limit to the calculated sublimation flux. Following the analysis in Ref. [2], the heat flux to the surface is approximated by

$$q = (2k_B T_i + \mid eV_{sheath} \mid)\Gamma_{se}, \tag{6.3}$$

where T_i is the ion temperature, V_{sheath} is the voltage drop through the sheath, and Γ_{se} is the particle flux at the sheath edge. For this analysis, V_{sheath} is assumed to be the applied voltage to the electrode, approximated from voltage measurements on ZaP-HD as 4.8 kV. The particle flux is expressed as

$$\Gamma_{se} = n_{se} c_s \approx \frac{1}{2} n_0 [k_B(T_e + T_i)/m_i]^{1/2}, \tag{6.4}$$

where n_{se} is the electron number density at the sheath edge. The calculation uses the peak density in Fig. 4.6(a) as n_0, the same temperature values used in Eq. 6.1, and

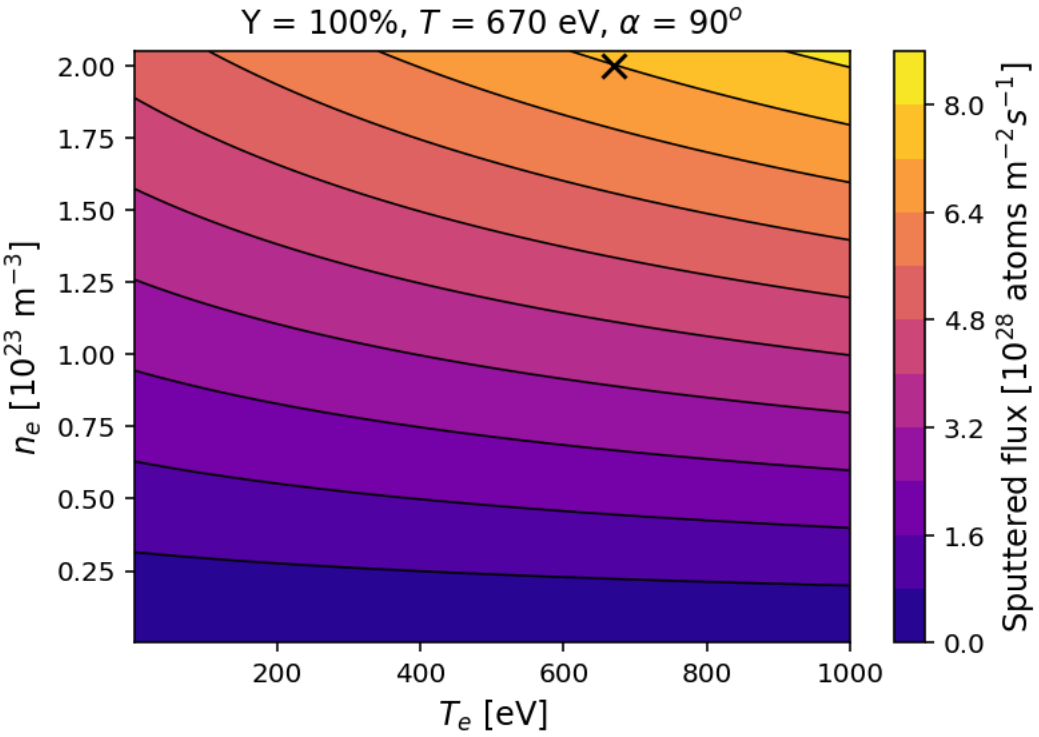

Figure 6.1: Theoretical values for the eroded carbon flux due to physical sputtering by hydrogen ions, assuming a sputtering yield of 100%, $T = T_i = 670$ eV, and normal incidence of impacting ions. The value indicated by the marker is used for comparison to measured erosion fluxes.

the ion mass of hydrogen as m_i. To obtain the flux of sublimated carbon, the heat flux calculated in Eq. 6.3 is divided by the surface binding energy of 7.4 eV, which is the heat of sublimation of graphite [98]. The result is a theoretical sublimated flux of 3×10^{31} atoms $\mathrm{m}^{-2}\mathrm{s}^{-1}$. This value is roughly a factor of 400 times larger than the theoretical sputtered flux. Simulations for parameters on the FuZE device resulted in sublimation five orders of magnitude larger than sputtered fluxes [66]. This larger discrepancy is attributed to the incorporation of prompt redeposition effects in the model which reduces the sputtered flux.

6.2 Gross Electrode Erosion is Dominated by Sublimation

Using the methods described in Chapter 4, measurements of the eroded carbon flux are obtained throughout the duration of the plasma pulse. The expanded radial profiles of number density and temperature shown in Fig 4.10 are used as representative values across the three compression bank voltage settings tested to determine the S/XB coefficients. These expanded profiles modified the radial profiles in Fig. 4.6, which have a peak number density of 2×10^{23} m^{-3}. This is the average density measured for pulses of all compression bank voltages in the PMI study by Forbes [72]. The range of peak number densities for these voltage settings varies from $10^{20} - 10^{24}$ m^{-3}.

To obtain a time-resolved measurement, the S/XB diagnostic was triggered at intervals of 5 μs over repeated pulses. The results are shown in Fig. 6.2 for the three compression voltage settings. Figure 6.2(a) shows the campaign-averaged pinch current measured using the $z = 10$ cm probe array. The shaded regions show the standard deviation across all pulses in each campaign. The variation in the pinch current for the 5 kV setting has some overlap with currents measured for the 7 kV setting close to the peak of the trace. Figure 6.2(b) shows the corresponding erosion measurements. Each data point is obtained from an individual pulse, and represents

the average of measured values within 1.2 mm of the ZaP-HD axis. The peak pinch current occurs at approximately 50 μs, which is concurrent with the period of high measured carbon erosion. The particle and heat flux from the plasma should be the largest close to the time of peak pinch current, leading to greater erosion. The erosion measurements show a similar overlap between the 5 kV and 7 kV settings which is attributed to the pinch current overlap.

Figure 6.2(b) also compares the measured total erosion with the theoretical values for the sublimation flux (red dotted line) and physical sputtering flux (black dotted line) calculated in the previous section. Throughout most of the pulse duration, the erosion fluxes are at least two orders of magnitude larger than the maximum theoretical sputtered flux. The measured fluxes approach the maximum sublimation flux, and at times exceed it for the 9 kV pulses. This suggests that the majority of the C-III emission recorded by the S/XB measurement comes from ionized carbon neutrals that have sublimated off the electrode surface.

When the current is low at early and late stages of the pulse, the measured erosion flux is at or below the theoretical sputtered flux limit. At these times, little to no radiation is measured on the spectrometer, therefore these values indicate the lower limit of the erosion measurement. Depending on how quickly the graphite heats up and subsequently cools, sublimation may occur at early and late phases of the pulse in addition to during peak current. The duration of C-III emission appears to decrease with the lower voltage. Since a lower voltage results in lower pinch current, the graphite takes more time to heat up to sublimation temperatures.

6.3 Redeposition of Sublimated Particles Reduces the Net Erosion

The mechanism of material erosion implies a difference in the energy of the neutral that is ejected from the surface. Specifically, the energy of a sputtered atom should be

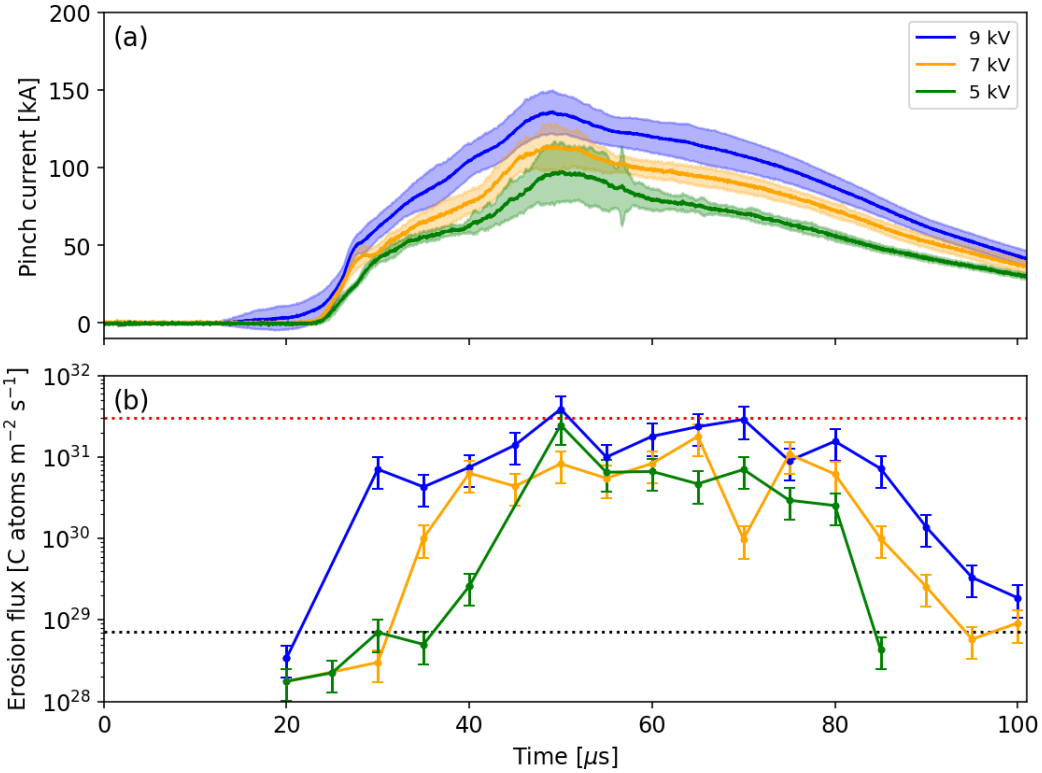

Figure 6.2: Time evolution of the (a) pinch current and (b) flux of gross eroded carbon for the compression capacitor bank voltages used in the study. In (a), the shaded regions show the standard deviation of the pinch current over all pulses in each campaign. Increasing this voltage setting increases the pinch current, which corresponds to greater measured erosion flux. The red and black dotted lines correspond to theoretical upper limits of the flux from sublimation and physical sputtering, respectively. Comparison of these theoretical values to the measurements suggests that total erosion is dominated by sublimation.

comparable to the ion impact energy, and a sublimated atom should have an energy comparable to the electrode surface temperature. This difference in energy translates to a different ionization mean free path for the two neutral populations, which ultimately determines whether the neutral enters the bulk plasma or is redeposited on the electrode. The following describes the calculation of the ionization mean free path of neutral carbon from the ZaP-HD electrode. In both cases, the neutral carbon enters the plasma at thermal speed $v_{th,n}$,

$$v_{th,n} = \left(\frac{2k_B T_n}{m_n} \right)^{1/2}, \tag{6.5}$$

where k_B is the Boltzmann constant, T_n is the neutral temperature, and m_n is the neutral mass. The mean free path for electron impact ionization of neutrals is given by

$$\lambda_n = \frac{v_{th,n}}{\nu_n} = \frac{v_{th,n}}{n_e \overline{\sigma v}}, \tag{6.6}$$

which is the ratio of the thermal speed and the collision frequency for neutrals with electrons, ν_n. The collision frequency itself is the product of the electron number density n_e and the ionization rate coefficient, $\overline{\sigma v}$. The ionization rate coefficients are obtained by integrating the cross-section over a Maxwellian distribution of the electron velocity. Values of this coefficient from ADAS [91] for single ionization of neutral carbon range from $10^{-19} - 10^{-13}$ $\mathrm{m^3 s^{-1}}$ over electron temperatures between 1 and 10^4 eV.

The next step is to determine the appropriate value of T_n for sublimation and sputtering. Sublimated neutrals should have energy corresponding to the surface temperature. This gives a minimum $T_{n,sub}$ of 3900 K, the sublimation temperature of graphite, [92] equivalent to 0.3 eV.

In the case of sputtered neutrals, the neutral energy corresponds to the difference between the ion impact energy and the threshold energy for sputtering. Using the

analysis presented in Ref. [2], this energy is

$$T_{n,sp} = E_0\gamma(1-\gamma) - E_{sb}, \tag{6.7}$$

where $T_{n,sp}$ is the energy of the sputtered neutral, E_0 is the impact energy of the ion, E_{sb} is the surface binding energy of the solid, and γ is the maximum energy fraction defined in Eq. 2.13. This fraction comes from the momentum transfer of two particles with mass M_1 and M_2 in a head-on collision. For the pure hydrogen plasma in ZaP-HD, H^+ is the dominant ion species. Therefore, the energy fraction is calculated with the atomic masses of hydrogen and carbon. Note that $E_{sb} = 7.4$ eV is negligible compared to the first term in Eq. 6.7 for the conditions being studied. The ion impact energy is calculated with

$$E_0 = 2k_B T_i + \mid eV_{sheath} \mid . \tag{6.8}$$

V_{sheath} is the voltage drop through the electrode sheath, assumed to be the applied voltage. This is approximated from voltage measurements to be between 2.8 and 4.8 kV. Assuming thermal equilibrium, $T_i = T_e = 1$ keV from Ref. [1]. Calculating the impact energy with Eq. 6.8 gives $E_0 = 6.8$ keV, which corresponds to $T_{n,sp} = 1.4$ keV from Eq. 6.7. The ionization mean free path of neutrals is then calculated with Eqs. 6.5 and 6.6. The scale length of interest for comparison is the sheath thickness, λ_s, which is on the order of the Debye length λ_D,

$$\lambda_s = \left(\frac{eV_{sheath}}{k_B T_e}\right)^{1/2} \lambda_D, \tag{6.9}$$

using the electron number density $n_e = 2 \times 10^{23}$ m^{-3} from Ref. [1].

The resulting mean free paths are plotted in Fig. 6.3. For the $100 - 1000$ eV range of electron temperatures expected on ZaP-HD, the sputtered neutrals have a mean free path of 1×10^{-5} m, while sublimated neutrals have a mean free path of 2×10^{-7} m. These values are compared to the sheath thickness calculated from

Eq. 6.9 which is 1×10^{-6} m. This analysis shows that sublimated neutrals are ionized within the sheath, while sputtered neutrals are ionized over distances greater than the sheath thickness. The sublimated neutrals that are ionized within the sheath are subsequently accelerated by the sheath electric field back to the electrode surface where they are redeposited. By contrast, since sputtered neutrals are ionized much deeper within the bulk plasma they are not affected by the sheath electric field. Crucially, these results describe a physical process of recycling of eroded carbon atoms that significantly reduces the net erosion. Although sublimation accounts for the bulk of the total erosion, high redeposition rates return this carbon to the electrode, while the sputtered carbon flux is primarily responsible for the net erosion.

The sublimation flux represents an additional source of electrons to drive the pinch current, as described in Sec. 2.7. Assuming single ionization, an order of magnitude estimate for the current density that can be supported by the sublimation flux is calculated by multiplying 10^{31} $\mathrm{m^{-2}s^{-1}}$ by the elementary charge, which gives 10^{12} $\mathrm{A/m^2}$, which is three orders of magnitude larger than the expected current density calculated in Sec. 2.7. Furthermore, since the sheath thickness for a sheath voltage drop of a few kilovolts is significantly larger than the ionization mean free path, this recycling effect can also be achieved with much lower voltages that result in smaller sheath thicknesses. In fact, Eq. 6.9 indicates that for ZaP-HD, a sheath voltage drop as low as 100 V is already sufficient to produce a sheath thickness equal to the ionization mean free path of sublimated neutrals. Indeed, sheath voltage drops in the kilovolt range are not required for this process to occur, as demonstrated by a recycling process involving evaporation of electrode material that has been observed for thermionic tungsten cathodes with sheath voltages of only $10 - 15$ V [99].

It is important to also consider possible magnetic effects on this physical picture using the concepts presented in Sec. 2.4. Namely, the Larmor radius is calculated

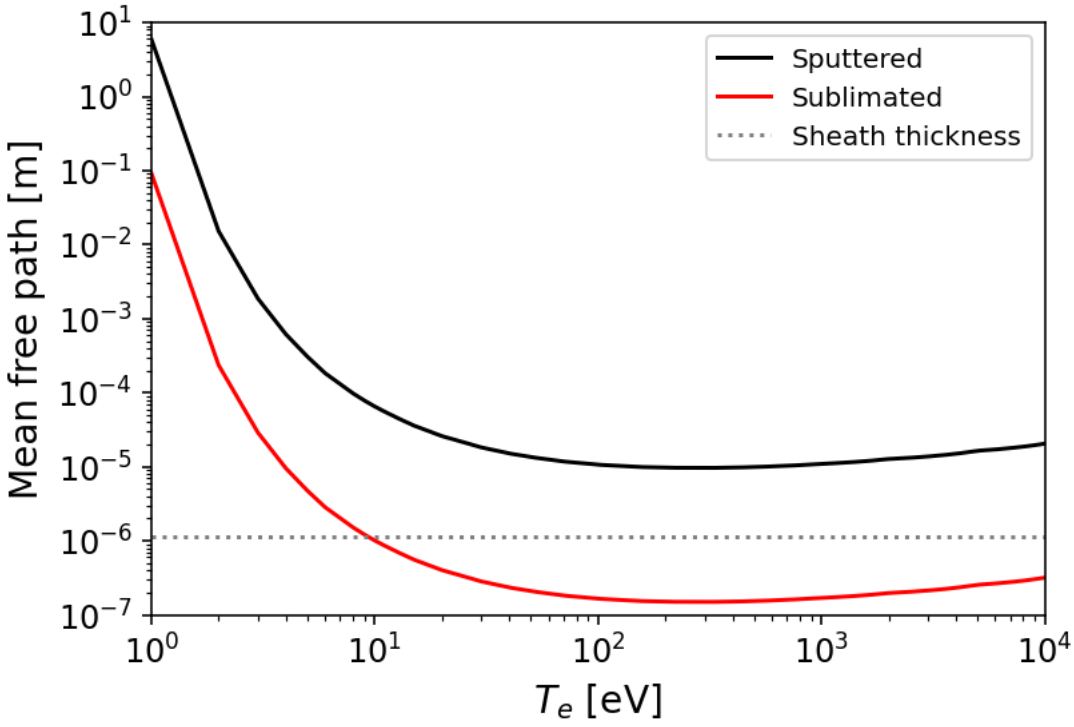

Figure 6.3: Comparison of the electron impact ionization mean free paths for sputtered and sublimated carbon neutrals. For the $100 - 1000$ eV range of temperatures relevant to ZaP-HD, the sublimated neutrals are ionized over a distance much shorter than the sheath thickness, while sputtered neutrals undergo ionization well outside of the sheath.

for both sublimated and sputtered carbon and compared to the respective ionization mean free paths. Equation 2.18 is used to calculate the Larmor radius, which assumes $v_\perp$ to be the neutral thermal speed. The maximum value of the local magnetic field occurs at the pinch radius. From the equilibrium analysis described in Sec. 4.2.4, this is calculated to be 6.6 T. The Larmor radius for sputtered carbon is 3×10^{-3} m and is 4×10^{-5} m for sublimated carbon. Both of these values are much larger than the respective ionization mean free paths in Fig. 6.3, so redeposition from cyclotron motion can be expected for both erosion processes. Therefore, the magnetic field acts to reduce the net erosion from sputtered carbon, and enhances redeposition of sublimated carbon that is already occurring due to acceleration within the sheath. The electron Larmor radius is also calculated, which is on the order of 10^{-7} m. This is an order of magnitude smaller than the sheath thickness, which means that the magnetic field has little effect on overall electron motion.

In Sec. 4.3.1, the same equilibrium analysis is repeated accounting for plasma expansion when in contact with the electrode. Assuming this physical picture is accurate, this increases the contact area, which reduces the current density and the magnetic field. This is confirmed by the calculations which give a reduced magnetic field strength of 2 T. Magnetization of the ions is decreased, resulting in larger Larmor radii: 9×10^{-3} m and 1×10^{-4} m for sputtering and sublimation respectively. Therefore, the expansion of plasma on the electrode acts to enhance the redeposition rates for both erosion processes. As described in Ref. [53], depending on the angular distribution of sputtered neutrals, a significant fraction can avoid redeposition through this mechanism and cause net erosion. On the other hand, redeposition of sublimated neutrals remains far more likely due to the combined effects of sheath acceleration and large Larmor radius. Therefore, incorporation of magnetic effects is compatible with the physical picture of carbon recycling described by this analysis.

Chapter 7

EX-SITU ANALYSIS OF GRAPHITE ELECTRODE COUPONS

One of the primary objectives of this research is to determine the response of the ZaP-HD electrode material to plasma exposure and high current density. Mass measurements are a straightforward indication of net erosion or redeposition. The material response is also characterized by measuring changes in the surface morphology, material composition, and surface profile. Modification of these characteristics is related to the physical processes occurring at the surface from the incident particle and heat flux, such as erosion damage from sputtering, cracking from thermal fatigue, or the build-up of redeposited material. This chapter describes the mass measurements of the graphite electrode coupons, calculation of erosion rates, and the effects of plasma exposure on the microscopic graphite surface.

Mass measurements and surface analysis are conducted ex-situ using the removable electrode coupons described in Sec. 3.5. Mass measurements are used to calculate net erosion fluxes in $m^{-2}s^{-1}$ units which are compared to spectroscopic erosion measurements from Sec. 6.2. In addition, the electrode erosion rates in mg/C units are calculated for comparison to electrodes in other devices. Surface analysis was performed with the Apreo-S scanning electron microscope (SEM) at the UW Molecular Analysis Facility (MAF), and with the Olympus OLS4100 optical profilometer at the Washington Clean Energy Testbeds (WCET). The SEM provides high-resolution images of the microscopic surface, and is equipped with energy-dispersive X-ray spectroscopy (EDS) for elemental analysis. The optical profilometer measures the microscopic sur-

face profile, which is used to calculate changes in the surface roughness. In Fig. 7.1, blue squares indicate the locations of SEM measurements, and the red square shows the location of optical profilometer measurements. SEM micrographs were obtained along the x and y axes every 10 mm for various magnifications. Profilometry measurements were limited to the center of the coupon at the tip. All measurements were made with the coupon oriented as shown in Fig. 7.1.

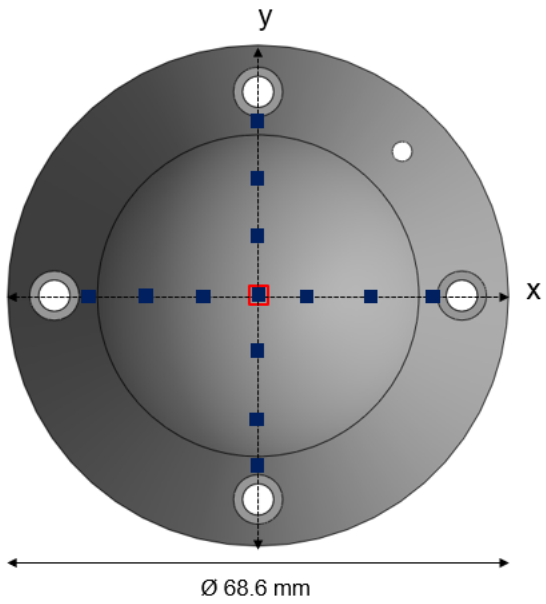

Figure 7.1: Map of locations on the graphite electrode coupon where surface analysis was conducted. The coupon orientation for analysis was controlled by placing the smaller hole at 45 degrees from the x axis as shown. Blue solid squares show SEM measurement locations. The red square shows the location of optical profilometer measurements.

7.1 Coupon Mass Measurements and Net Erosion Rates

The coupon mass was recorded before and after each experimental campaign using a Mettler Toledo MS403TS scale with a 1 mg accuracy. This gives the change in mass, Δm. The average initial mass of the three coupons is 71.056 g.

For comparison to the erosion measurements from Fig. 6.2(b), an equivalent net erosion flux Γ_{net} is calculated in units of $\mathrm{m^{-2}s^{-1}}$ using

$$\Gamma_{net} = \frac{\Delta m}{N_p m_C \tau_p A_p}, \tag{7.1}$$

where N_p is the number of pulses, m_C is the carbon atomic mass, τ_p is the duration of plasma exposure, and A_p is the area over which erosion occurs. Simplifying assumptions are made, namely that the erosion flux is constant between pulses, throughout the duration of plasma exposure and over the entire specified area. The duration τ_p is defined for when the pinch current is above 20% of the peak current using measurements from Fig. 6.2(a), which is approximately 80 μs at each voltage setting. The area A_p is assumed to be the cross-section of the pinch with the characteristic radius of 3 mm from Ref. [1].

Some additional quantities are required to calculate the electrode erosion rate. The net mass loss measurement is divided by the number of pulses to obtain the mass loss per pulse. This also assumes that the erosion rate is constant between pulses. The total charge passed through the electrode during an individual pulse is calculated by integrating the pinch currents in Fig. 6.2(a). The ratio of these values gives the electrode erosion rate in mg/C units.

Useful quantities that characterize the plasma exposure are also calculated to facilitate comparison with other experiments. The peak current density is calculated by dividing the peak pinch current from each current trace in Fig. 6.2(a) by the area A_p used in Eq. 7.1. In addition, the hourly mass loss rate is calculated in the

same manner as Ref. [66], which assumes the 10 Hz repetition rate of a power plant. The ZaP-HD transferred charge per pulse is multiplied by 10 Hz, which gives the charge transferred per second. Converting this to the charge transferred per hour and multiplying by the ZaP-HD erosion rates gives the hourly mass loss rate.

Lastly, the total ion fluence is calculated to quantify the overall plasma exposure on each coupon. Using the raw spectra of C-III emission recorded for the S/XB measurements in Fig. 6.2(b), the ion temperature is extracted from Doppler broadened profiles using the basic method described in Ref. [74]. This ion temperature is used to calculate the particle flux of hydrogen. Like the analysis in Sec. 6.1, thermal equilibrium is assumed between ions and electrons. The peak density from Fig. 4.6(a) is assumed, which is the same assumption made in Sec. 6.3. The hydrogen ion flux is calculated with

$$\Gamma_H = nc_s \approx \frac{1}{2} n_0 [k_B(T_e + T_i)/m_H]^{1/2}, \tag{7.2}$$

where m_H is the mass of the hydrogen ion. Integration of this ion flux over the duration of the measurement provides the ion fluence for each pulse, which is multiplied by the number of pulses to obtain the total ion fluence for each coupon.

The results of these calculations are summarized in Table 7.1. The uncertainty of the mass measurement and the standard deviation of the pinch current are propagated through the calculations to provide the uncertainty of the erosion flux and the erosion rate. Each of the electrode coupons experienced a net mass loss. Calculating the net erosion fluxes with Eq. 7.1 gives values between $10^{27} - 10^{28}$ $\mathrm{m^{-2}s^{-1}}$. These values are significantly lower than the measured total erosion fluxes during peak pinch current given in Fig. 6.2(b). The net erosion fluxes are also lower than the theoretical sputtered flux by 1-2 orders of magnitude, but this theoretical value assumes a 100% sputtering yield and does not account for the reduced flux to a surface tangential to magnetic field lines described in Sec. 2.4. The coefficient for reduced flux f_B given in

Eq. 2.19 can be calculated assuming the characteristic length to be the diameter of the pinch, $L = 6$ mm, and calculating the Bohm diffusion coefficient from Eq. 2.20. The magnetic field $B = 0.2$ T, is obtained from the average magnetic field measured by probes at $z = 10$ cm in the assembly region. The resulting value for the coefficient $f_B = 0.14$, which is close to the expected reduction to 10% given by Ref. [54] and the value assumed in Ref. [66]. Further reduction of the sputtered flux results from the analysis of the ion Larmor radius presented in Sec. 6.3. Therefore, the theoretical sputtered flux is likely to be comparable to the net erosion fluxes. This result supports the assertion made in Sec. 6.3 that net erosion is primarily due to sputtering.

The erosion rates of the electrode coupons are between 0.01 and 0.1 mg/C. The lower end of this range is comparable to 0.016 mg/C for a carbon electrode operating in a 100 A vacuum arc discharge [67], while the upper end remains below the 0.250 mg/C value for a simulated 80 kA carbon arc furnace [68]. The erosion rates on ZaP-HD are also significantly lower than the 8 mg/C observed for a tungsten electrode in a 120 kA high-pressure discharge-current [100]. The current densities are within the range defined for cathodic arc discharges of $10^8 - 10^{13}$ A/m^2 given in Ref. [40] and on the same order calculated in Sec. 2.7.

The hourly mass loss rates calculated using the erosion rates from ZaP-HD are significantly lower than the ≈ 3 kg per hour estimated in Ref. [66], which assumes the 0.250 mg/C erosion rate from Ref. [68]. While this result is quite favorable, a power plant level device will operate at pinch currents over a thousand times larger than ZaP-HD [66] and will likely cause significantly greater erosion rates.

Notably, the net erosion does not appear to increase monotonically with the intensity of plasma exposure, since the highest erosion rate was observed for the intermediate conditions of Case II. This result may be explained by the presence of competing effects that contribute to net erosion. The analysis in Sec. 6.3 describes how sput-

tered carbon is primarily responsible for the net erosion. However, consideration of magnetic effects reveals how redeposition of sputtered carbon can still occur due to the large ion Larmor radius relative to the ionization mean free path. Analysis by Naujoks [53] shows that the fraction of prompt redeposition decreases sharply from near unity as the ratio of the ionization mean free path to the Larmor radius increases. A decrease in Larmor radius could be a result of stronger magnetic fields due to the increased current density of a smaller pinch radius. A decrease in the pinch radius with increased pinch current is also expected from the scaling relations described in Sec. 1.2. However, the high exposure conditions of Case I were in part produced by a higher capacitor bank voltage, which applies a larger bias voltage to the electrode. Assuming that this applied voltage is primarily dropped in the sheath, the ion impact energy increases to be on the order of several keV as shown in Sec. 6.3. At these impact energies, sputtering yields begin to decrease due to the ions penetrating deeper into the solid lattice [2]. This reduced physical sputtering yield, along with greater sublimation from elevated surface temperatures for higher pinch currents, could reverse the effects of stronger magnetization and reduced Larmor radius, resulting in the reduced net erosion at high voltage settings.

Finally, the total ion fluence over each experimental campaign is 1-2 orders of magnitude lower than those capable on LPDs described in Sec. 2.6. This limits the evaluation of PMI effects at comparably high particle fluence and long plasma exposures, albeit at the elevated particle and heat fluxes on ZaP-HD.

7.2 Electron Microscopy

SEM imaging of the graphite surface can reveal changes in the surface morphology that are indicative of certain PMI processes. For instance, surface modification in the form of pits or craters may indicate erosion by sputtering processes. Layers of

Table 7.1: Summary of mass measurements, erosion-related quantities and exposure-related quantities for each graphite electrode coupon. Total fluence values refer to the entire experimental campaign for each plasma exposure case.

Quantity	**I**	**II**	**III**
Measured mass change, Δm [mg]	-17 ± 1	-32 ± 1	-4 ± 1
Mass change per pulse [mg]	-0.085 ± 0.005	-0.64 ± 0.02	-0.10 ± 0.02
Charge transferred per pulse [C]	7.5 ± 0.9	6.2 ± 0.6	5.0 ± 0.5
Net erosion flux, Γ_{net} [$\times 10^{27}$ m^{-2}s^{-1}]	1.8 ± 0.1	13.1 ± 0.4	2.0 ± 0.5
Erosion rate [mg/C]	0.010 ± 0.001	0.10 ± 0.01	0.020 ± 0.005
Current density [$\times 10^9$ A/m^2]	4.8 ± 0.5	4.0 ± 0.5	3.5 ± 0.7
Mass loss per hour [kg]	0.003 ± 0.001	0.020 ± 0.003	0.003 ± 0.001
Total ion fluence [$\times 10^{26}$ m^{-2}]	4.4 ± 0.2	1.0 ± 0.6	0.5 ± 0.3

material deposited on the surface can result in distinctive textures or features that are characteristic of redeposition.

An SEM focuses a beam of electrons onto the sample surface, which then interact with the sample at various depths and through various processes. Multiple detectors record the scattered or emitted electron signals, which are used to create an image of the surface. The micrographs presented in this work were all obtained using the Everhart-Thornley Detector (ETD), which detects the secondary electron (SE) emission. SE emission originates from within a few nanometers of the surface of the sample. This smaller interaction volume leads to improved resolution of the surface structure and topography. Alternatively, back-scattered electrons originate from deeper within the sample and are used to detect the composition rather than the surface features. The ETD is often positioned at an angle to the surface. The contrast in micrographs obtained with the ETD comes from the difference in SE intensity. Increased scattering of the electron beam off of edges or discontinuities results in a stronger recorded signal on the ETD, leading to bright regions in the micrograph.

No sample preparation was required for the graphite coupons aside from the placement of adhesive tabs for mounting to the sample stage. Image magnifications range from 65x to 5000x. This corresponds to a scale length of 500 μm to 5 μm, or a total field of view of 2 mm down to 25 μm, respectively. A set of micrographs at these magnifications is provided in Fig. 7.2 comparing the graphite surface before and after plasma exposure under the three experimental cases. Magnification increases from left to right. The top row shows images before plasma exposure, and moving down the subsequent rows represents a decrease in plasma exposure conditions.

The surface prior to exposure, shown in Figs. 7.2(a)-(c), consists of distinct particles or closely packed groups of particles 5-100 μm in size that are scattered over the bulk graphite matrix. These particles are larger than the specified particle size

for this graphite grade, which is less than 5 μm [97]. These large particles were likely produced by fracturing of the matrix during machining. At the highest magnification, Fig. 7.2(c), the granular structure of the matrix is more apparent. Some porosity at the surface is observable, indicated by dark voids in between grains. These voids are consistent with the specified pore size of 0.8 μm [97].

After plasma exposure, there are clear changes to the surface morphology. The 65x magnification images, Figs. 7.2(d), (g), and (j), show that the large particles are almost completely removed. Increasing the magnification to 500x in Figs.7.2(e), (h) and (k) reveals consolidated surface structures that resemble flakes, scales, or ripples. At the 5000x magnification, greater detail of these structures is observed. Their shapes are irregular, ranging from ribbon-like striations in Fig. 7.2(f) to more rounded slabs in Figs. 7.2(i) and (l). Some areas, such as the darker region in the right-central portion of Fig. 7.2(i) appear to be relatively smooth. Lastly, cracking of the surface is also observed at 500x and 5000x magnification, which may be an indication of thermal fatigue from many heating cycles. This suggests a degree of importance of the surface temperature in creating this morphology.

Quantitative analysis of SEM micrographs is performed along the x and y axes established in Fig. 7.1. Two quantities are calculated: the first is the average area of the dark regions which indicates the presence of voids in the graphite matrix, and the second is the average eccentricity of these dark regions which characterizes their change in shape. A Python script converts raw micrograph images to grayscale and applies a 15% intensity threshold to isolate dark pixels. A filter is applied to remove detected regions smaller than 0.5 microns. The result is detection of the qualitative features described as voids, gaps, and cracks. For each contiguous region detected, the area and the eccentricity are calculated.

An example of the detected dark regions is given in Fig. 7.3 for micrographs taken

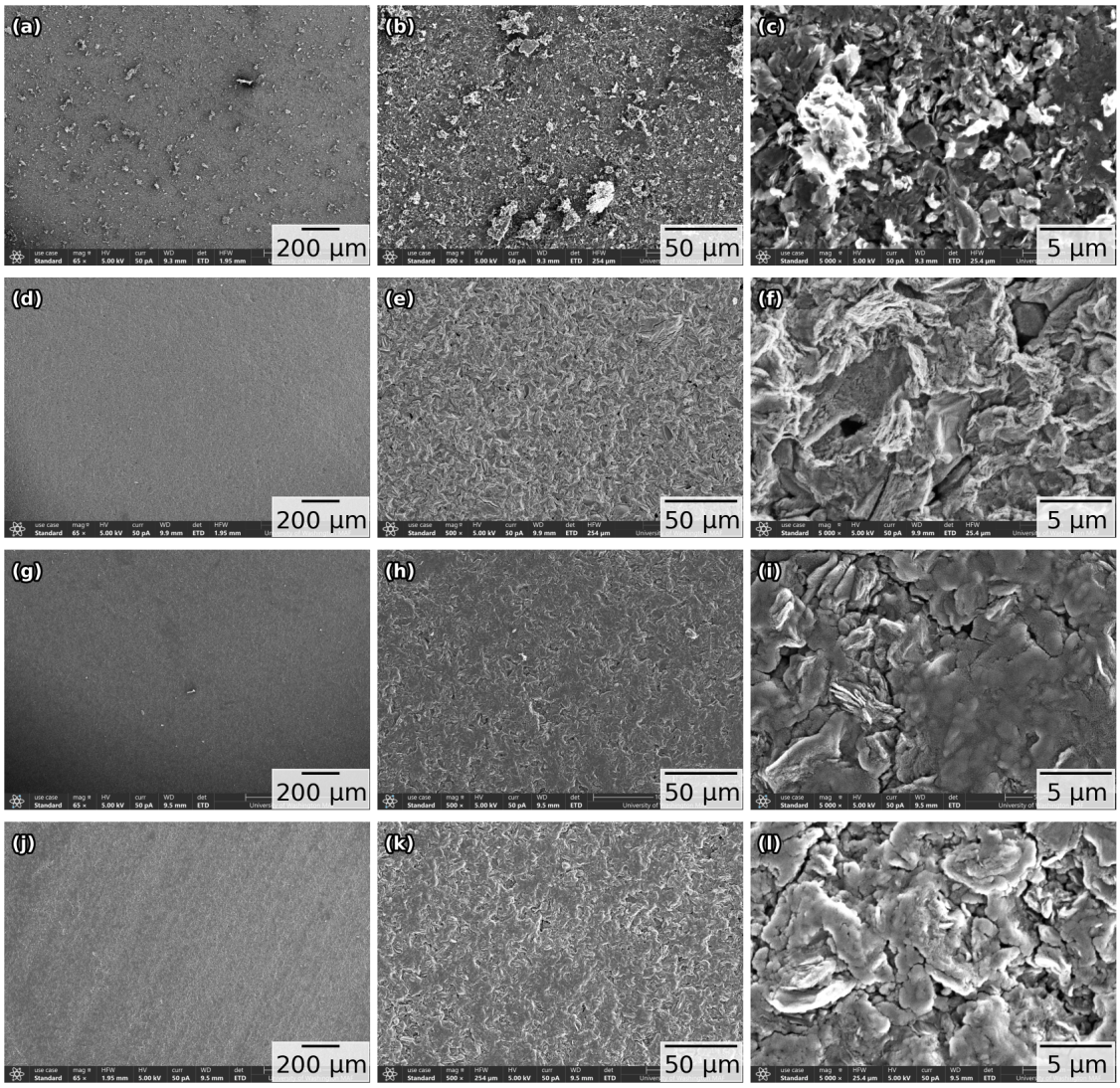

Figure 7.2: SEM micrographs of the graphite electrode coupon surface before plasma exposure (a), (b), (c), and after plasma exposure for Case I (d), (e), (f), Case II (g), (h), (i), and Case III (j), (k), (l). The intensity of plasma exposure on the coupon decreases from the second row downwards. From left to right, the magnification for each column is 65x, 500x, and 5000x. All plasma exposures resulted in removal of large particles scattered over the surface, and formation of irregular, consolidated features.

at 500x magnification. Before plasma exposure, in Fig. 7.3a, the dark regions are the voids within the graphite matrix. After plasma exposure, in Fig. 7.3b, the detected dark regions are primarily long, narrow gaps and cracks in between the consolidated ribbon-like structures. The spatial profiles of the average area and average eccentricity of dark regions detected at 500x magnification are plotted in Figs. 7.4 and 7.5 respectively. Error bars represent the standard deviation of the area or eccentricity of detected regions within a micrograph divided by the square root of the number of detected regions. It is evident that this change in morphology occurs throughout the 50 mm span of the SEM measurements, in perpendicular directions, and for all plasma exposure cases. This is a considerable portion of the coupon surface, which has a roughly 70 mm diameter as shown in Fig. 7.1. Notably, this effect is observed over areas much larger than the reported ZaP-HD Z-pinch radius of $2 - 5$ mm [5, 1]. This may be explained by wandering of the contact area or the expansion of the pinch column as it makes contact with the electrode, resulting in particle and heat flux over an extended area.

The observed morphological changes indicate some form of material rearrangement, which is consistent with the general process of carbon recycling posited in Sections 6.2 and 6.3. Attributing morphology changes to specific mechanisms such as sputtering, sublimation, or melting is not unequivocal, especially with possible redeposited layers obscuring initial surface modifications. However, some useful statements can still be made. For instance, there is a distinct lack of cavities or pitting of the surface, features which have been attributed to sputtering in graphite bombarded with energetic ions [101]. Sputtering processes likely eject not only individual atoms but clusters of atoms [102] and even hydrocarbons [43]. If sputtering were more dominant, similar morphology would be expected on the graphite coupons. In terms of carbon deposition, the observed morphology is also unlike that of the cathode deposits

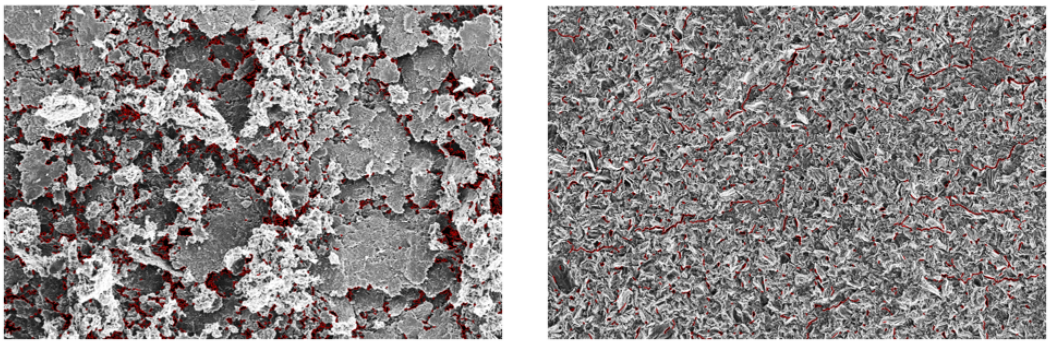

(a) Before plasma exposure (b) After plasma exposure

Figure 7.3: Dark region detection in a sample SEM micrograph of the graphite coupon surface before and after plasma exposure. These images were taken for the coupon in Case I at 500x magnification. In (a), the detected dark regions are the irregularly shaped voids in between graphite grains. In (b), the detected dark regions are the cracks and narrow gaps in between consolidated ribbon-like structures.

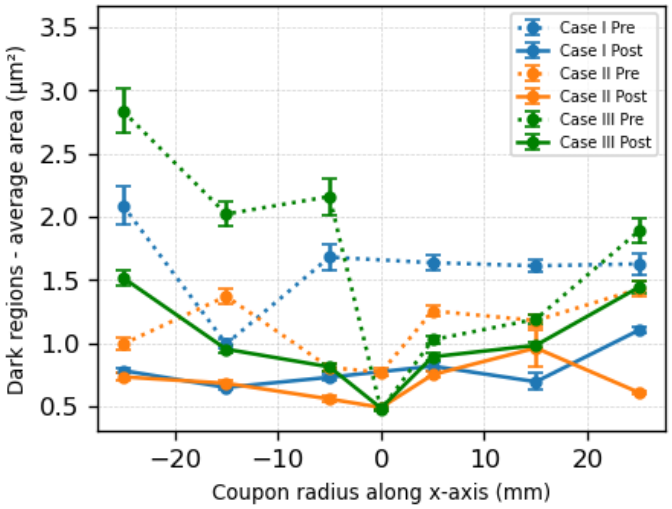

(a)

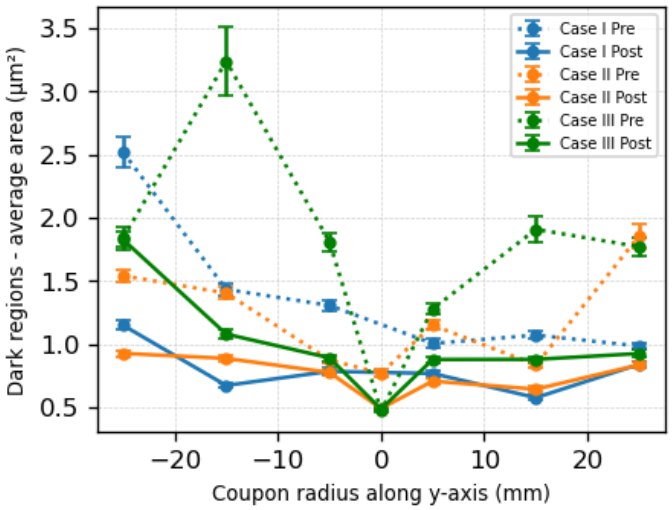

(b)

Figure 7.4: Changes in the average area of dark regions in SEM micrographs of the graphite coupon surface along the (a) x axis and (b) y axis defined in Fig. 7.1. Analysis is performed for micrographs at 500x magnification. For all three plasma exposure cases, the dark region area decreases along both axes. This represents the change in morphology of the surface from the porous graphite matrix to the irregular, consolidated structures observed in Fig. 7.2.

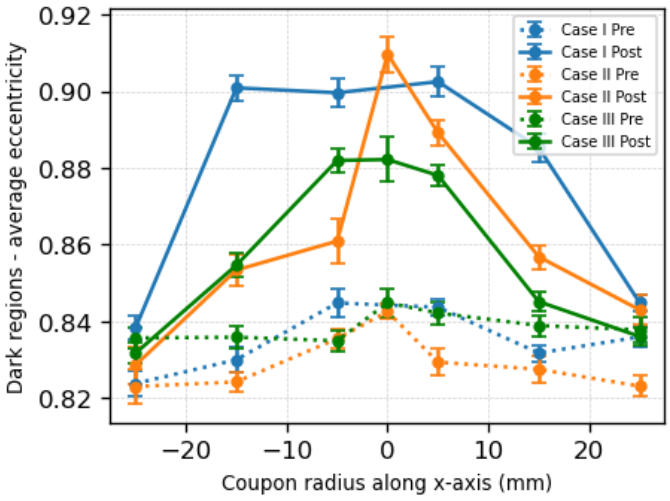

(a)

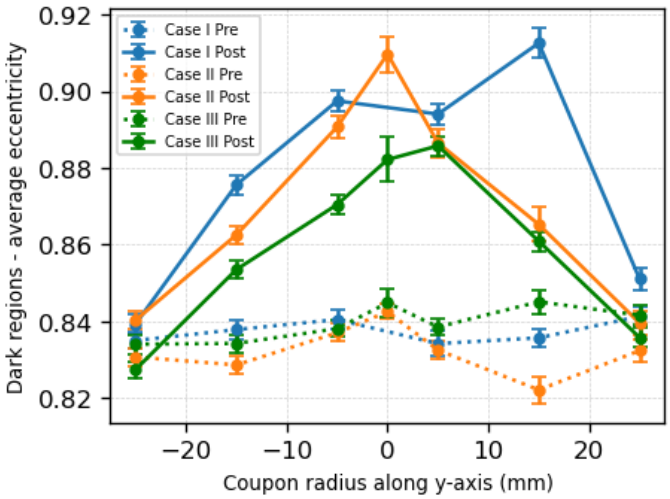

(b)

Figure 7.5: Changes in the average eccentricity of the detected dark regions in SEM micrographs of the graphite coupon surface along the (a) x axis and (b) y axis defined in Fig. 7.1. Analysis is performed for micrographs at 500x magnification. For all three plasma exposure cases, the eccentricity increases significantly, representing a change in morphology from the voids in the porous graphite matrix to the narrow gaps between the irregular, consolidated structures observed in Fig. 7.2. This analysis also detects the cracking of the surface observed after plasma exposure.

formed by carbon arcs for nanosynthesis [103], which feature highly spherical morphology for surface temperatures exceeding 3000 K, and ion temperatures of about 1 eV. For the carbon arc, carbon ions are produced through ablation of the anode that travel along the arc to the cathode. Due to the short ionization mean free path of sublimated neutrals calculated in Sec. 6.3, the redeposited layer on the graphite coupons is not expected to display such a preferential morphology, but would likely be more uniform or follow the contours of the surface.

While the discussion of thermal effects on the graphite surface has so far only addressed sublimation, previous work identified the possibility of graphite melting [72]. Melting of graphite can occur at 4000 K for sufficiently high pressures. However, a large degree of uncertainty applies to the necessary pressures, which range from 110 atm and 100,000 atm [104]. Calculation of the required plasma temperature using Eq. 1.2 to achieve the required pressures gives a range of 320 eV to 320 keV, assuming $n_e = 2 \times 10^{23}$ m^{-3}. Measured ion and electron temperatures on ZaP-HD either meet or exceed the low end of this range, [74, 1] lending some plausibility to graphite melting. The solidification of a melt layer on the surface of the graphite could explain the consolidated features observed in Fig. 7.2.

7.3 Profilometry

Profilometry measurements provide a three-dimensional picture of the surface topography. Although a sense of depth can be perceived by the contrast in certain SEM measurements, these images do not explicitly capture height information. Measuring the surface profile can be used to measure the extent of material deposition or erosion, and quantifying the surface roughness has important implications on PMI effects such as sputtering, where the local angle of incidence can significantly impact the yield.

In Figs. 7.6, 7.7, and 7.8, optical images of the graphite surface and the corre-

sponding height maps are shown at various magnifications. Each pair of 4×2 grids contains measurements for a single coupon. For each grid, the left hand column contains images before plasma exposure, and the right hand column contains images after plasma exposure. Images were taken at 5x, 20x, 50x, and 100x magnifications, increasing down the rows.

Before plasma exposure, the 5x magnification images for all cases show parallel striations on the graphite surface left behind from the fabrication process. In Fig. 7.6a for Case I, the striations have been completely removed after plasma exposure. In Figs. 7.7a and 7.8a, the striations remain visible for Cases II and III respectively, likely due to the lower ion fluence and overall exposure conditions listed in Table 7.1. At 50x and 100x magnification, the effect of plasma exposure is qualitatively similar across all three cases, with the appearance of bright regions with rounded, smooth edges. These are likely the same features visible at 500x magnification in the SEM images of Fig. 7.2.

For consideration of the height maps in Figs. 7.6b, 7.7b, and 7.8b, there are two points of note. Firstly, the highly reflective surface in the top left image of Fig. 7.6a likely caused saturation of the sensor, which results in the flat height profile seen in the corresponding profile shown in Fig. 7.6b. All other acquisitions were able to resolve the surface profile. Secondly, the reference point for zero height was not maintained between acquisitions, therefore absolute comparison of the heights measured is not possible. Consequently, only relative changes such as the roughness are calculated and compared.

A summary of the roughness calculations is provided in Tables 7.2 and 7.3, consisting of two roughness parameters, R_a and R_{RMS} at 5x and 100x magnifications. The parameter R_a is the arithmetic average of the absolute deviations from the mean surface height, which captures the overall roughness but is less sensitive to large irreg-

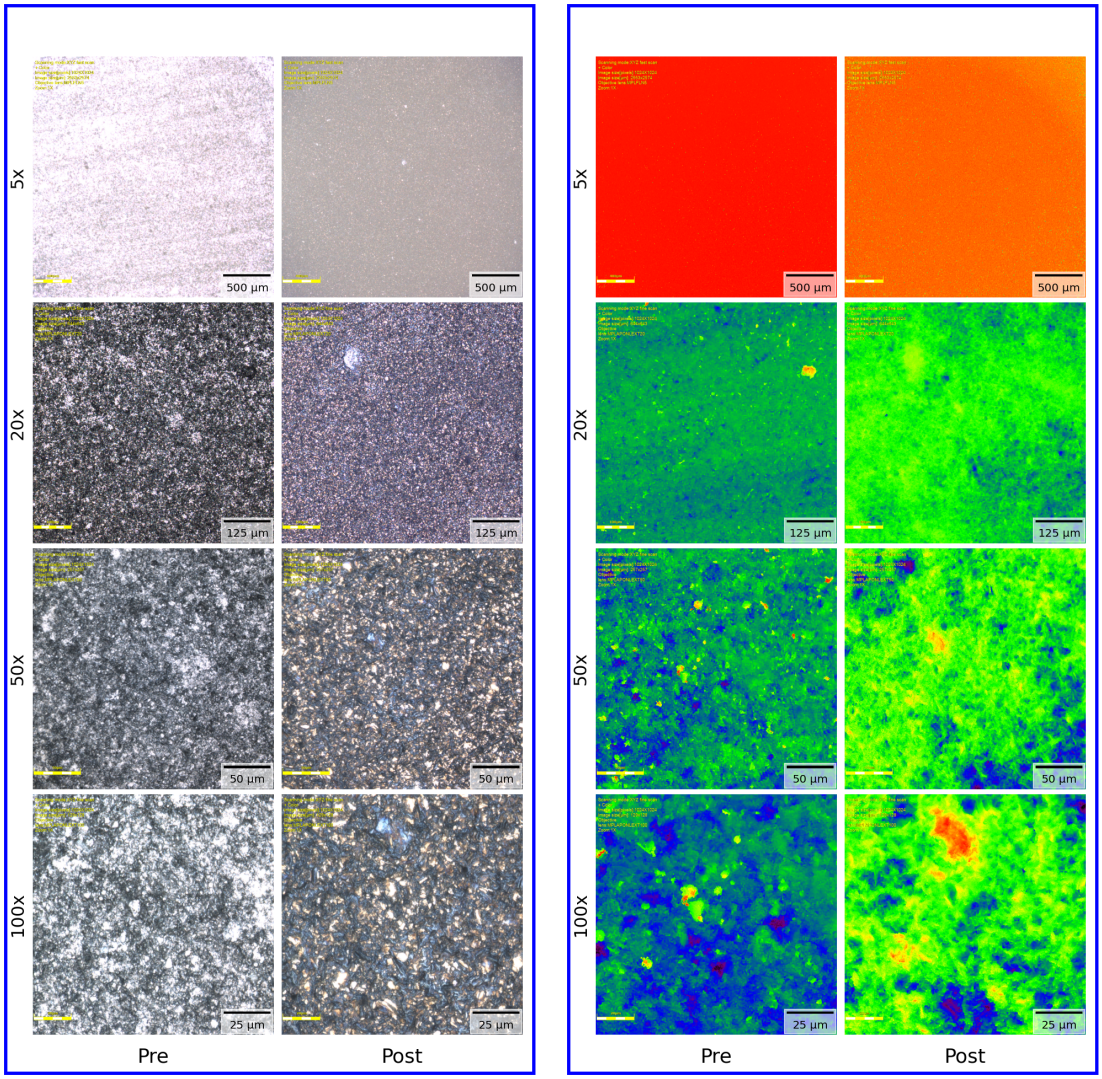

(a) (b)

Figure 7.6: (a) Optical images and (b) height profiles of the graphite coupon surface before and after plasma exposure for Case I. Height measurements of the surface before plasma exposure could not be resolved at 5x magnification due to issues with focusing the profilometer. Higher magnification images show smooth regions coincident with the consolidated surface structures observed after plasma exposure.

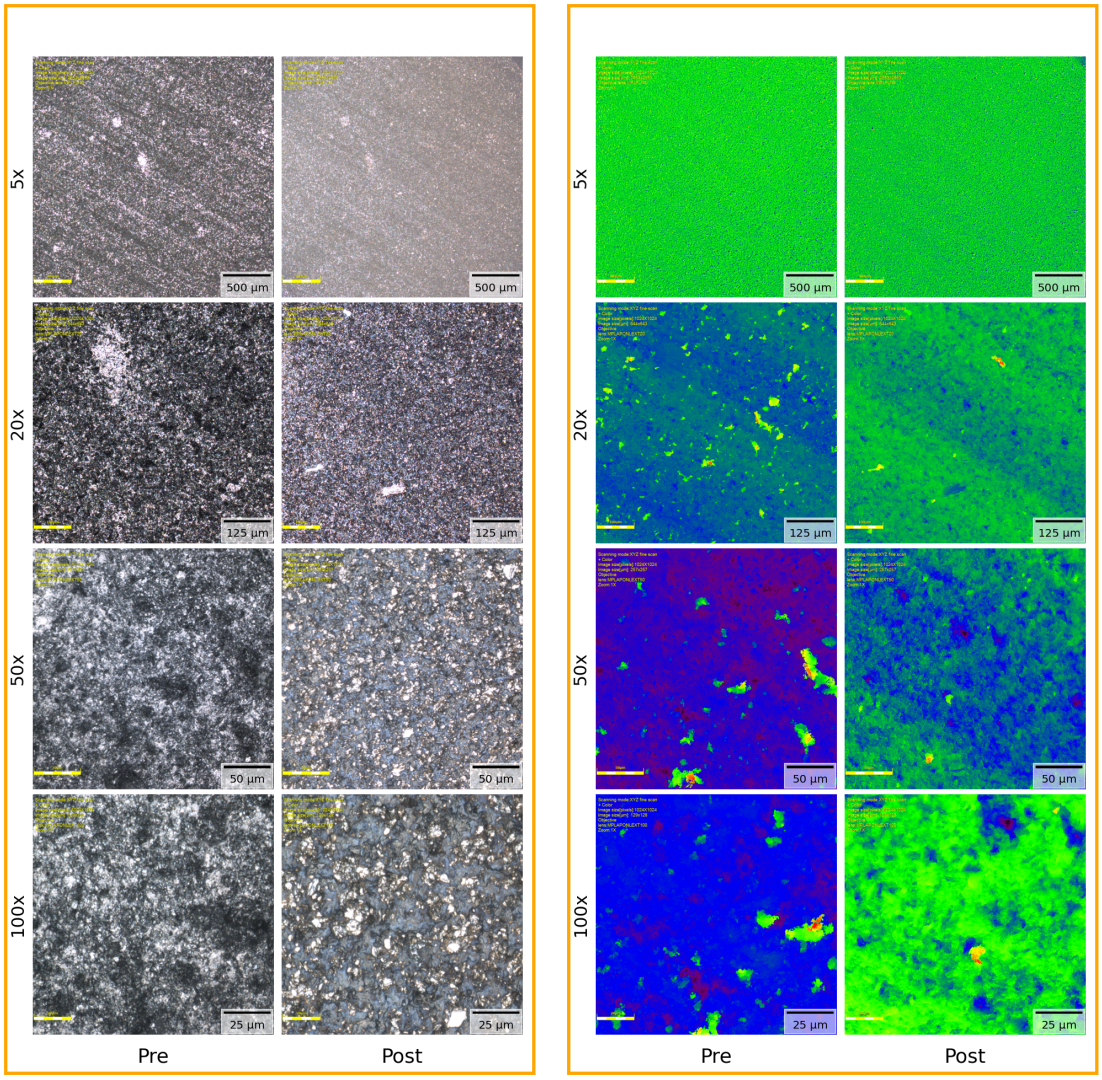

(a) (b)

Figure 7.7: (a) Optical images and (b) height profiles of the graphite coupon surface before and after plasma exposure for Case II. The parallel striations observed at 5x and 20x magnifications are machining artifacts that are mostly preserved after plasma exposure, which supports the conclusion of low net erosion from Chapter 6.

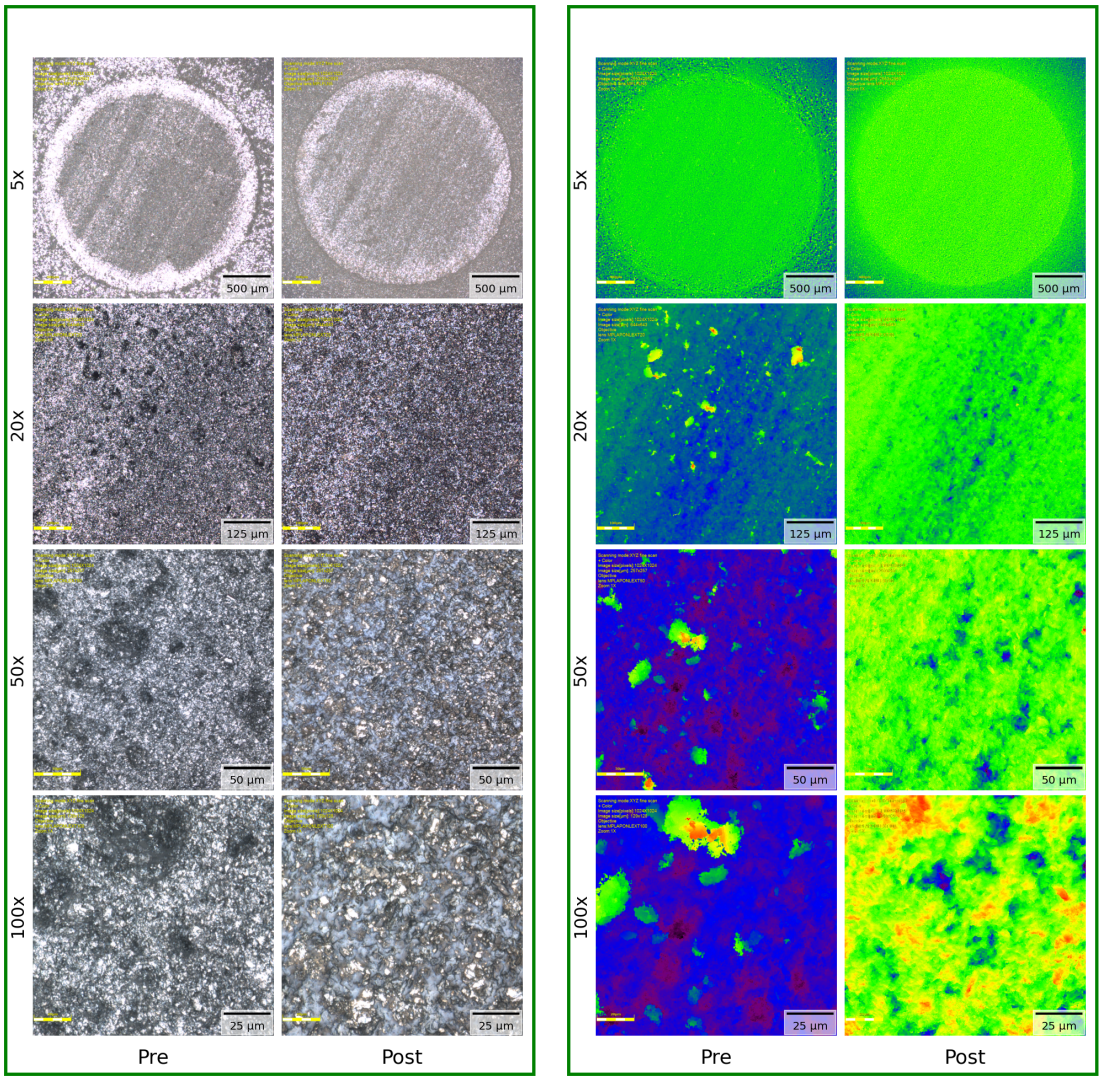

(a) (b)

Figure 7.8: (a) Optical images and (b) height profiles of the graphite coupon surface before and after plasma exposure for Case III. Machining artifacts are also preserved at 5x and 20x magnifications.

ularities. The parameter R_{RMS} is the root-mean-square (RMS) of the deviations from the mean surface height, which is more sensitive to irregularities. The values given are the average of the roughness parameter calculated along the vertical dimension of each image at 1024 sampling positions, i.e. at the pixel resolution of the profilometer height maps. The uncertainty provided is the standard deviation over these sampling locations. In general, both roughness parameters decrease after plasma exposure, and the variation across the sampled length also decreases. This is consistent with the removal of distinct particles and appearance of the consolidated features observed in SEM micrographs.

The exception to this behavior occurs for Case I, which has an increase in roughness calculated for both 5x and 100x magnifications. Since similar morphological changes appear to occur for all three cases, it is possible that the significantly larger particle fluence in Case I was enough to induce surface changes beyond the initial smoothing effect. The large increase in roughness in R_a for Case I in Table 7.2 is attributed to the high reflectivity observed at 5x magnification in Fig. 7.6a, therefore is not indicative of the true change in roughness. Profiles of R_{RMS} used to calculate the average values in Table 7.3 are plotted in Fig. 7.9 to illustrate the spatial variation of roughness. Again, smoothing of the surface occurs after plasma exposure with the exception of the coupon in Case I.

Smoothing of graphite electrode surfaces has been attributed to sublimation in certain applications. A 30 kA spark gap in a nitrogen environment resulted in extremely smooth sub-micron scale surfaces. This was attributed to sublimation on the basis of a lack of craters that would indicate sputtering of graphite particles, as well as the appearance of deposits of monatomic layers of amorphous carbon [105]. However, the effects of chemical reactions between carbon and nitrogen complicate a direct comparison. On the other hand, the importance of ion fluence and surface

Table 7.2: Summary of surface roughness measurements performed on the graphite electrode coupons before and after exposure to ZaP-HD Z-pinch plasmas. Profilometer measurements were made at 5x magnification.

Case #	R_a [μm]		R_{RMS} [μm]	
	Before	After	Before	After
I	8.8 ± 1.2	18.1 ± 4.5	51.2 ± 4.4	53.4 ± 12.2
II	14.8 ± 0.9	13.3 ± 0.8	20.0 ± 1.3	17.7 ± 1.0
III	19.0 ± 4.2	16.8 ± 1.9	26.4 ± 5.5	21.8 ± 2.3

temperature has been noted in the submicron-scale roughening of graphite under argon ion bombardment, [106] which aligns with the increased roughness observed for the graphite coupon in Case I.

7.4 Energy Dispersive X-ray Spectroscopy

EDS measures the elemental composition and their spatial distribution in a sample. X-rays are produced in the sample by interaction with an incident electron beam or X-rays. The resulting spectrum is measured by an energy dispersive spectrometer, which can resolve the number and energy of the emitted X-rays. Because the energies are characteristic of specific electronic transitions within an atomic structure, they can be used for elemental identification, and the intensity can be related to the abundance of each element. The Apreo-S SEM used in this study was equipped with the EDAX Octane Ultra EDS system.

Figure 7.10 illustrates the relative mass ratio of impurities detected on each of the three coupons after plasma exposure. In all cases, carbon makes up the remainder of detected elements. Before plasma exposure, each coupon had a trace amount ($< 1\%$)

Table 7.3: Summary of surface roughness measurements performed on the graphite electrode coupons before and after exposure to ZaP-HD Z-pinch plasmas. Profilometer measurements were made at 100x magnification.

Case #	R_a [μm]		R_{RMS} [μm]	
	Before	After	Before	After
I	0.6 ± 0.2	0.9 ± 0.3	0.8 ± 0.3	1.2 ± 0.3
II	0.8 ± 0.4	0.6 ± 0.2	1.3 ± 0.7	0.8 ± 0.2
III	2.2± 1.4	0.8 ± 0.2	3.1 ± 1.9	1.0 ± 0.2

of oxygen. After exposure, the oxygen content increased to a few percent over all three coupons. Oxygen likely comes from exposure to atmosphere due to the ex-situ measurement, as well as any water vapor in the ZaP-HD vacuum chamber. Oxygen may also come from the alumina insulators between the ZaP-HD electrodes.

Additional impurities are detected with known sources within the ZaP-HD vacuum chamber, which indicate migration and deposition to the electrode. Aluminum is the other main constituent of the alumina insulators, and is detected on all the coupons. However, aluminum content in the measured regions is relatively low, never exceeding 1%. Tungsten is also observed on all coupons. The inner electrode upstream of the nose cone is a tungsten-sprayed copper tube. The presence of tungsten on the coupons indicates tungsten erosion upstream of the Z pinch. The greatest percentage of tungsten was observed for Case I, which exposed the electrode to the largest particle fluence and the largest current density. Tungsten is almost entirely undetected for Case II, although it is slightly more prevalent in Case III.

Iron is detected for Case I and Case II, although notably more prevalent for Case II. Sources of iron include the internal vacuum chamber wall, the outer electrode, or the

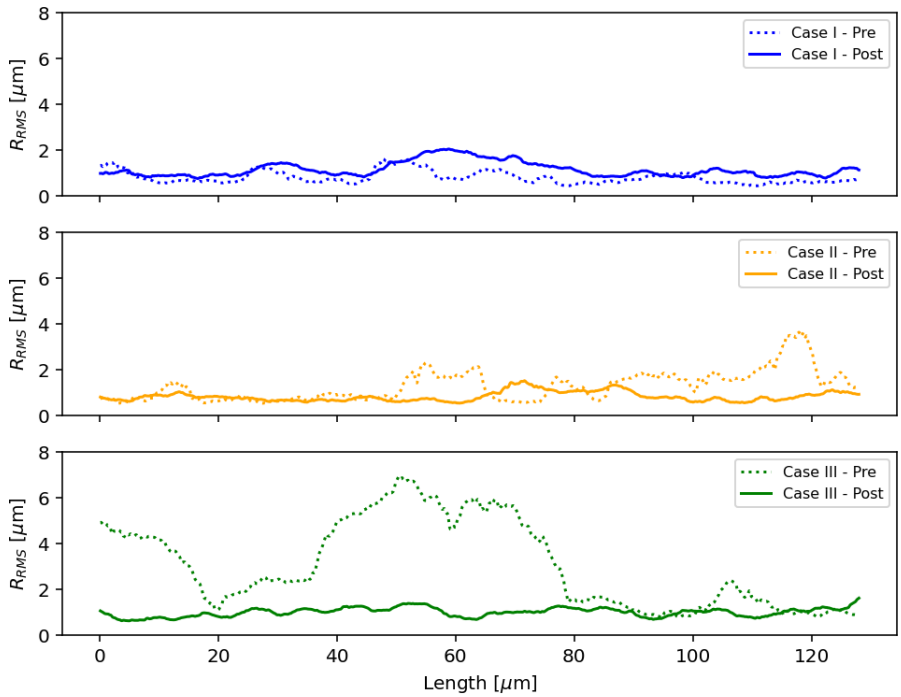

Figure 7.9: Changes in the roughness parameter R_{RMS} for each plasma exposure case. Smoothing of the surface occurs for the low fluence exposure in Cases II and III, while slight roughening occurs at the high particle fluence of Case I.

stainless steel fasteners for the electrode coupon assembly. While the exact source of the iron is unable to be determined from this data, possible scenarios of iron impurity production include arcing to the outer electrode or vacuum chamber, or erosion of the socket head screws that fasten the coupon due to contact with the plasma. However, it is unlikely for arcing to only be prevalent at a single voltage setting, and not at the higher voltage setting. This prevalence of iron for Case II does coincide with the larger net erosion experienced by the coupon for those conditions. However, further investigation into the source of iron impurity production and impurity migration is required to explain this result and any possible correlation.

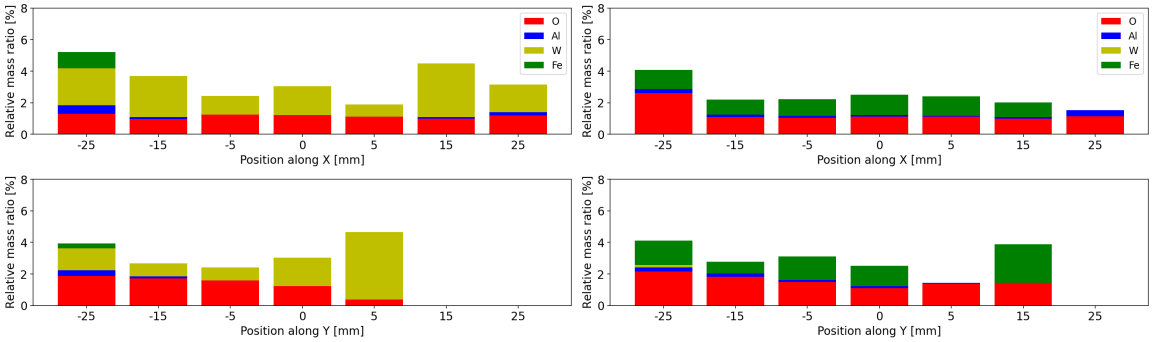

(a) Case I

(b) Case II

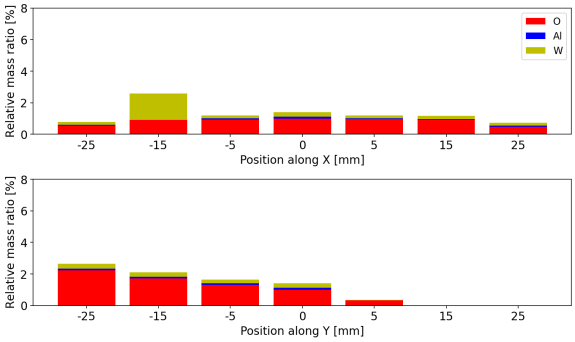

(c) Case III

Figure 7.10: Relative mass ratios of detected impurities on the graphite coupon surface after plasma exposure measured using EDS. EDS measurements were made at each SEM position described in Fig. 7.1. Prior to plasma exposure, each coupon was over 99.9% carbon, with trace amounts of oxygen detected. Aluminum, tungsten, and iron are all detected, which have known sources in the ZaP-HD vacuum chamber. Case II is noteworthy for having the most prevalent iron deposition to the electrode, which may point to increased erosion and redeposition of the outer electrode or fastener heads in the electrode assembly.

Chapter 8

CONCLUSION

The ZaP-HD flow Z-pinch device brings a high density, high temperature plasma into direct contact with a solid electrode, which also supplies the pinch current. These represent unique conditions to investigate fusion-relevant PMI effects occurring between the electrode and the plasma. This dissertation describes the results of experiments that study plasma-electrode interactions on the ZaP-HD SFS Z-pinch device. In-situ measurements of the gross carbon erosion flux were conducted with S/XB spectroscopy. Measurements show agreement with the expected sublimation flux, but are significantly larger than the expected physical sputtering flux. This suggests that total electrode erosion is dominated by sublimation. Assuming that the sublimated carbon neutral energy is comparable to the electrode surface temperature, electron impact ionization occurs within the electrode sheath, which causes redeposition of carbon back to the electrode. This is not the case for sputtered neutrals, which are ionized beyond the sheath region. This describes a physical mechanism for recycling of sublimated carbon and loss of sputtered carbon that results in significant reduction of net erosion.

A commercial two-color pyrometer was fielded to measure the change in graphite electrode surface temperature. The response time was limited to 2 ms, which prevented monitoring of the temperature during the pulse, but temperatures up to 1700 ^{o}C were observed 2 ms after the pulse was triggered. Simple one-dimensional analysis of the heat diffusion through a planar wall of graphite indicate that a thin layer of graphite can cool to within a few hundred degrees of this measured tem-

perature at this time scale. The reported temperatures are well below the expected sublimation or melting point for graphite, and consistent loss of signal was observed. A possible reason for this behavior could be the production of carbon vapor and changes in the surface morphology which affects the emissivity of the pyrometer channels. Further refinement of the pyrometry measurement is required before definitive values of the surface temperature can be reported. Although limited, these results do suggest that sublimation only occurs during the plasma pulse, during which the sheath permits the observed electrode recycling process. If sublimation temperatures were sustained beyond the duration of the plasma, there would be no mechanism for the return of sublimated carbon.

Ex-situ analysis of electrode material was enabled by redesigning the electrode with a removable coupon. Three coupons were tested for a range of capacitor bank voltage settings and total number of pulses. These parameters control the pinch current and total particle fluence. Net erosion fluxes calculated from mass-loss measurements are found to be significantly lower than spectroscopic measurements of the gross erosion, but are comparable to the expected sputtering flux. This supports the theory of high carbon recycling rates which reduce the net erosion. Under the tested conditions, ZaP-HD erosion rates ranged from $0.01 - 0.1$ mg/C, which are comparable to those for electrodes in various arc discharges. Notably, the largest net erosion was recorded for the intermediate plasma exposure conditions. This could be due to reduced sputtering yields at the elevated ion impact energies for the higher capacitor bank voltage, which counteracts the effects of a smaller pinch and higher current density that are expected to increase net erosion.

Distinct changes in the surface morphology and roughness indicate substantial rearrangement of electrode material. The most striking change in surface morphology is the appearance of consolidated, irregular structures over an area much larger than

the characteristic pinch radius of 3 mm. This is consistent with the assumption of plasma expansion when in contact with the electrode made in Chapter 4. There is a distinct lack of pits and craters that could be associated with sputtering processes, however a general smoothing of the surface profile is observed for the lower particle fluence cases that could be associated with redeposition. However, definitive attribution of these surface changes to sublimation, melting, and redeposition is difficult with the current data. Elemental analysis revealed deposition of various impurity species such as tungsten, aluminum, and iron, with some variation between the experimental conditions tested.

The results presented here indicate some alignment of plasma-electrode interactions on ZaP-HD with processes specific to electrodes in arc discharges. Namely, there is evidence for a material recycling process that reduces net erosion. This phenomenon has been observed for thermionic cathodes used in welding and plasma arc cutting tools, where evaporation and redeposition of the cathode material play a similar role [99]. In addition, it is encouraging that net erosion rates are comparable to or lower than those for various arc discharges, especially for the high plasma temperatures and current densities on ZaP-HD.

This recycling process represents an additional source of electrons to drive the large current densities on ZaP-HD. These electrons are liberated through the ionization of sublimated carbon neutrals. The carbon ions are subsequently redeposited to the cathode. This mechanism for electron emission avoids the damaging erosion that results from the enhanced thermionic and field emission typically required to sustain such large current densities as discussed in Sec. 2.7. It is also important to note that this recycling process occurs in the case of the negative sheath voltage found at the cathode, which sets up an electric field in the direction of the material surface. This causes acceleration and redeposition of carbon ions to the electrode. For the

large voltages applied on ZaP-HD, the cathode sheath takes up essentially all of the applied voltage, while the anode sheath voltage saturates but remains negative with respect to the plasma potential. It is theoretically possible, though perhaps unlikely, for a positive sheath voltage to occur at the anode, which would not permit the same recycling process. Therefore, the presence of a similar recycling process on other configurations requires consideration of the sheath potential at the particular plasma-electrode interface.

As has been identified in other work [19, 66], solutions for electrode erosion management in the SFS Z pinch benefit from the relatively small volume and mass in direct contact with plasma, and the simple geometry for component replacement. The research in this dissertation suggests that the wealth of knowledge in operating high-powered plasma arc discharges could also be relevant for the SFS Z pinch. This provides confidence that practical solutions to manage electrode erosion in fusion devices are possible.

Chapter 9
FUTURE WORK

The experimental investigation described in this dissertation has generated a wealth of data and new insights on the nature of plasma-electrode interactions on the ZaP-HD device. This work has also identified several avenues for future investigation, which are described in this chapter.

An important objective of future work is to obtain experimental verification of sublimation or melting of graphite. Evidence for sublimation or melting can be obtained from other surface analysis techniques. For instance, a Focused Ion Beam (FIB) SEM can be used to mill into a sample to expose a cross-section several microns deep. Redeposition of sublimated carbon or surface melting should produce layers that are distinct from the bulk material, such as those observed for metallic electrodes on cathodic arc plasmas [107]. Another approach could be to use an X-ray diffractometer to detect changes in crystal structure, since phase changes should induce deformations to the hexagonal crystal structure of graphite. Additionally, while the two-color pyrometer used in this study does not measure up to the 3900 K sublimation point, the consistent loss of signal at temperatures well below the sublimation point indicates potential challenges relevant to any application of pyrometry that should be addressed. In particular, characterization of graphite emissivity and the response of the two-color pyrometer could be investigated under controlled heating conditions with fiducial temperature measurements in a bench-top experiment.

While the erosion rates in this study are comparable to existing arc discharges, and there appears to be a mechanism for electrode material recycling, it is necessary

to evaluate erosion values at longer plasma exposures. As stated in Chapter 7, the ion fluences tested in this investigation did not reach the typical values for linear plasma devices. An extended experimental campaign on the order of 1000 pulses would begin to provide comparable ion fluences. Major PMI effects and material issues are known to become significant on longer time scales and for high cycle numbers [62], which motivates the exploration of longer overall plasma exposures. The roughening of the graphite surface for Case I, in contrast to the smoothing effect seen at the lower plasma exposures, may suggest the presence of these effects.

In addition to the ion fluence, it is crucial to investigate electrode erosion at much higher current densities and plasma temperatures. Approximate parameters for an SFS Z-pinch power plant given in Refs. [19] and [66] are $\approx$ 1 MA pinch currents, $\approx$ 1 keV plasma temperatures, and $\approx$ 0.1 mm pinch radii. These pinch currents and plasma temperatures are an order of magnitude larger than what is capable on ZaP-HD, and the pinch radii are an order of magnitude smaller. The current density is also an order of magnitude larger, at $\approx 10^{10}$ A/m^2. Electron densities are three orders of magnitude higher. These conditions will significantly increase the particle and heat flux to the electrode, and combined with high repetition rates will present a far more extreme environment for the electrode to withstand. This will also serve to shed light on the nature of possible competing effects for net erosion with increasing current density that are discussed in Chapter 7. Although these operating conditions are not yet available on existing devices, the intermediate parameter space may be accessed by upgrading the ZaP-HD capacitor bank to drive additional pinch current, or conducting similar experiments on existing higher-powered SFS Z-pinch devices.

Furthermore, many of the advantages of the electrode coupon apparatus have yet to be fully exploited, particularly the ability for rapid and frequent replacement. This study describes testing of a limited number of coupons. A more comprehensive test

matrix can serve to isolate the effects of the pinch current and the ion fluence in a similar manner to the PMI experiments by Forbes [72]. Preparation of the coupons themselves can be improved by polishing of the surface to control the initial roughness and remove machining artifacts. This would help to isolate effects only from plasma exposure and not from initial surface roughness. Further experimentation can also incorporate witness plates to characterize material deposition on the electrode, and testing of various candidate plasma-facing materials.

A number of assumptions were made in the application of the S/XB measurements for inferring the erosion flux. The influence of the line-integrated measurement in particular has a large effect on the recorded emission intensity. Characterization of the radial variation in C-III emission would provide a more accurate model of the background plasma that must be subtracted, instead of assuming a constant emission. Absolute intensity calibration of a PMT array would provide improved spatial and temporal resolution of the erosion flux, enabling closer correlation to changes in the pinch current and the behavior of the plasma measured by other diagnostics. In addition, diagnosing the local plasma parameters at the spectroscopic chord locations would allow more accurate calculation of the erosion fluxes. This can be achieved by placing interferometric chords just in front of the electrode nose cone.

Finally, modeling efforts of plasma-electrode interactions should be expanded to compare with the experimental results. Calculation of expected sputtering yields with SRIM/TRIM codes can be used to refine the theoretical estimates of the sputtered flux. Evaluation of PMI codes such as ERO [108], which can model surface morphology evolution, should be conducted. Additionally, thermal analysis using finite element methods can be used to model electrode heating for the electrode nose cone geometry that can provide information on the spatial extent of the heating, and to evaluate temperature distributions for different areas of plasma contact.

BIBLIOGRAPHY

[1] U. Shumlak, B. A. Nelson, E. L. Claveau, E. G. Forbes, R. P. Golingo, M. C. Hughes, R. J. Oberto, M. P. Ross, and T. R. Weber. Increasing plasma parameters using sheared flow stabilization of a z-pinch. *Physics of Plasmas*, 24(5):055702, 2017.

[2] P. C. Stangeby. *The plasma boundary of magnetic fusion devices*. Institute of Physics Pub., 2000.

[3] Roland Chodura. *Plasma Flow in the Sheath and the Presheath of a Scrape-Off Layer*, pages 99–134. Springer US, Boston, MA, 1986.

[4] Michael P. Ross. *Exploring plasma stability and confinement with high resolution density measurements on the ZaP-HD Flow Z-Pinch*. PhD thesis, University of Washington, 2016.

[5] M. P. Ross and U. Shumlak. Digital holographic interferometry employing Fresnel transform reconstruction for the study of flow shear stabilized Z-pinch plasmas. *Review of Scientific Instruments*, 87(10):103502, 2016.

[6] M. Whelan. Arc Lamps - The First Form of Electric Light. `https://edisontechcenter.org/ArcLamps.html/`, 2016. [Online; accessed 8-November-2023].

[7] Charles F. Brush. The "Brush" system of electric lighting. *Scientific American Supplement*, XI(274):4359–4364, 1881.

[8] National Research Council. *Plasma Processing of Materials: Scientific Opportunities and Technological Challenges*. The National Academies Press, Washington, DC, 1991.

[9] Sumio Iijima. Helical microtubules of graphitic carbon. *Nature*, 354:56–58, 1991.

[10] Jonathan Ng and Y. Raitses. Self-organisation processes in the carbon arc for nanosynthesis. *Journal of Applied Physics*, 117:063303, 2015.

[11] Nathan P. Brown and Mitchell L. R. Walker. Review of plasma-induced hall thruster erosion. *Applied Sciences*, 10(11), 2020.

[12] Edgar O'Hair, L. Hatfield, M. Kristiansen, Anthony Donaldson, and William Harris. *Arcjet cathode erosion studies*. AIAA, 1989.

[13] U. Shumlak, R. P. Golingo, B. A. Nelson, and D. J. Den Hartog. Evidence of stabilization in the Z-pinch. *Physical Review Letters*, 87:205005, 2001.

[14] R. P. Golingo, U. Shumlak, and B. A. Nelson. Formation of a sheared flow z pinch. *Physics of Plasmas*, 12(6):062505, 2005.

[15] U. Shumlak, C.S. Adams, J.M. Blakely, B.-J. Chan, R.P. Golingo, S.D. Knecht, B.A. Nelson, R.J. Oberto, M.R. Sybouts, and G.V. Vogman. Equilibrium, flow shear and stability measurements in the z-pinch. *Nuclear Fusion*, 49(7):075039, 2009.

[16] U. Shumlak, J. Chadney, R.P. Golingo, D.J. Den Hartog, M.C. Hughes, S.D. Knecht, W. Lowrie, V.S. Lukin, B.A. Nelson, R.J. Oberto, J.L. Rohrbach, M.P. Ross, and G.V. Vogman. The sheared-flow stabilized z-pinch. *Fusion Science and Technology*, 61(1T):119–124, 2012.

[17] B. Levitt, E. T. Meier, R. Umstattd, J. R. Barhydt, I. A. M. Datta, C. Liekhus-Schmaltz, D. A. Sutherland, and B. A. Nelson. The Zap Energy approach to commercial fusion. *Physics of Plasmas*, 30(9):090603, 2023.

[18] U. Shumlak. Z-pinch fusion. *Journal of Applied Physics*, 127(20):200901, 2020.

[19] B. A. Nelson M. C. Thompson, B. Levitt and U. Shumlak. Engineering paradigms for sheared-flow-stabilized z-pinch fusion energy. *Fusion Science and Technology*, 79(8):1051–1058, 2023.

[20] Marcus Laurence Elwin Oliphant and Ernest Rutherford. Experiments on the transmutation of elements by protons. *Proceedings of the Royal Society of London. Series A, Containing Papers of a Mathematical and Physical Character*, 141(843):259–281, 1933.

[21] A. S. Eddington. The internal constitution of the stars. *Nature*, 106(2653):14–20, 1920.

[22] M. G. Haines. Fifty years of controlled fusion research. *Plasma Physics and Controlled Fusion*, 38(5):643–656, 1996.

[23] James Arthur Pollock and Samuel Henry Egerton Barraclough. Note on a hollow lightning conductor crushed by the discharge. *Journal and proceedings of the Royal Society of New South Wales*, 39:131–138, 1905.

[24] George Thomson. Thermonuclear fusion: The task and the triumph. *New Scientist*, 3(63):10–12, 1958.

[25] James A. Phillips. Magnetic fusion. *Los Alamos Science*, 4(7):64–67, 1983.

[26] L. A. Artsimovich, S. V. Mirnov, and V. S. Strelkov. Investigation of the ohmic heating of a plasma in the 'tokamak-3' toroidal apparatus. *Journal of Nuclear Energy. Part C, Plasma Physics, Accelerators, Thermonuclear Research*, 7(3):305, 1965.

[27] M. G. Haines, S. V. Lebedev, J. P. Chittenden, F. N. Beg, S. N. Bland, and A. E. Dangor. The past, present, and future of Z pinches. *Physics of Plasmas*, 7(5):1672–1680, 2000.

[28] Willard H. Bennett. Magnetically self-focussing streams. *Physical Review*, 45:890–897, 1934.

[29] William A Newcomb. Hydromagnetic stability of a diffuse linear pinch. *Annals of Physics*, 10(2):232–267, 1960.

[30] V. D. Shafranov. The stability of a cylindrical gaseous conductor in a magnetic field. *The Soviet Journal of Atomic Energy*, 1(5):709–713, 1956.

[31] B. B. Kadomtsev. Hydromagnetic stability of a plasma. *Reviews of Plasma Physics*, 2:153–199, 1966.

[32] Sean D. Knecht, Weston Lowrie, and Uri Shumlak. Effects of a conducting wall on z-pinch stability. *IEEE Transactions on Plasma Science*, 42(6):1531–1543, 2014.

[33] U. Shumlak and C. W. Hartman. Sheared flow stabilization of the $m = 1$ kink mode in Z pinches. *Physical Review Letters*, 75:3285–3288, 1995.

[34] Eleanor G. Forbes, Uri Shumlak, Harry S. McLean, Brian A. Nelson, Elliot L. Claveau, Raymond P. Golingo, Drew P. Higginson, James M. Mitrani, Anton D. Stepanov, Kurt K. Tummel, Tobin R. Weber, and Yue Zhang. Progress toward a compact fusion reactor using the sheared-flow-stabilized z-pinch. *Fusion Science and Technology*, 75(7):599–607, 2019.

[35] Y. Zhang, U. Shumlak, B. A. Nelson, R. P. Golingo, T. R. Weber, A. D. Stepanov, E. L. Claveau, E. G. Forbes, Z. T. Draper, J. M. Mitrani, H. S. McLean, K. K. Tummel, D. P. Higginson, and C. M. Cooper. Sustained neutron production from a sheared-flow stabilized z pinch. *Physical Review Letters*, 122:135001, 2019.

[36] James M. Mitrani, Joshua A. Brown, Bethany L. Goldblum, Thibault A. Laplace, Elliot L. Claveau, Zack T. Draper, Eleanor G. Forbes, Ray P. Golingo, Harry S. McLean, Brian A. Nelson, Uri Shumlak, Anton Stepanov, Tobin R. Weber, Yue Zhang, and Drew P. Higginson. Thermonuclear neutron emission from a sheared-flow stabilized Z-pinch. *Physics of Plasmas*, 28(11):112509, 2021.

[37] Samuel E. Wurzel and Scott C. Hsu. Progress toward fusion energy breakeven and gain as measured against the Lawson criterion. *Physics of Plasmas*, 29(6):062103, 2022.

[38] Irving Langmuir. The interaction of electron and positive ion space charges in cathode sheaths. *Physical Review*, 33:954–989, 1929.

[39] D. Bohm. *The Characteristics of Electrical Discharges in Magnetic Fields*. A Guthrie and R K Wakerling (New York: McGraw-Hill), New York, 5 edition, 1949.

[40] André Anders. Glows, arcs, ohmic discharges: An electrode-centered review on discharge modes and the transitions between them. *Applied Physics Reviews*, 11(3):031310, 2024.

[41] A. Kirschner. Erosion and deposition mechanisms in fusion plasmas. *Fusion Science and Technology*, 53(2T):259–277, 2008.

[42] M.J. Baldwin and R.P. Doerner. Formation of helium induced nanostructure 'fuzz' on various tungsten grades. *Journal of Nuclear Materials*, 404(3):165–173, 2010.

[43] J.W. Davis, A.A. Haasz, and P.C. Stangeby. Hydrocarbon formation due to combined H + ion and H0 atom impact on pyrolytic graphite. *Journal of Nuclear Materials*, 155-157:234–240, 1988.

[44] D. Naujoks. Criterion for zero net erosion at divertor plates in fusion experiments. *Nuclear Fusion*, 37(9):1193, 1997.

[45] A.A. Haasz and J.W. Davis. *Hydrogen Retention in and Release from Carbon Materials*, pages 225–248. Springer Berlin Heidelberg, Berlin, Heidelberg, 2005.

[46] Jochen Linke, Juan Du, Thorsten Loewenhoff, Gerald Pintsuk, Benjamin Spilker, Isabel Steudel, and Marius Wirtz. Challenges for plasma-facing components in nuclear fusion. *Matter and Radiation at Extremes*, 4(5):056201, 2019.

[47] Yugo Ashida, Alexander Flick, Peter L. Andresen, and Gary S. Was. The key factors affecting crack growth behavior of neutron-irradiated austenitic alloys. In *Proceedings of the 15th International Conference on Environmental Degradation of Materials in Nuclear Power Systems — Water Reactors*, pages 1241–1255. Springer International Publishing, 2016.

[48] Steven J. Zinkle. Challenges in developing materials for fusion technology - past, present and future. *Fusion Science and Technology*, 64(2):65–75, 2013.

[49] W. W. Heidbrink and R. B. White. Mechanisms of energetic-particle transport in magnetically confined plasmas. *Physics of Plasmas*, 27(3):030901, 2020.

[50] J.W. Connor and R.J. Hastie. Relativistic limitations on runaway electrons. *Nuclear Fusion*, 15(3):415, 1975.

[51] M.N. Rosenbluth and S.V. Putvinski. Theory for avalanche of runaway electrons in tokamaks. *Nuclear Fusion*, 37(10):1355, 1997.

[52] J.P. Gunn, S. Carpentier-Chouchana, F. Escourbiac, T. Hirai, S. Panayotis, R.A. Pitts, Y. Corre, R. Dejarnac, M. Firdaouss, M. Kočan, M. Komm, A. Kukushkin, P. Languille, M. Missirlian, W. Zhao, and G. Zhong. Surface heat loads on the ITER divertor vertical targets. *Nuclear Fusion*, 57(4):046025, 2017.

[53] D. Naujoks, K. Asmussen, M. Bessenrodt-Weberpals, S. Deschka, R. Dux, W. Engelhardt, A.R. Field, G. Fussmann, J.C. Fuchs, C. Garcia-Rosales, S. Hirsch, P. Ignacz, G. Lieder, K.F. Mast, R. Neu, R. Radtke, J. Roth, and U. Wenzel. Tungsten as target material in fusion devices. *Nuclear Fusion*, 36(6):671, 1996.

[54] P.C. Stangeby, C.S. Pitcher, and J.D. Elder. The nature of plasma fluxes to surfaces nearly tangential to the magnetic field. *Nuclear Fusion*, 32(12):2079, 1992.

[55] A. S. Richardson. *NRL Plasma Formulary*. Naval Research Laboratory, 2019.

[56] Ch. Linsmeier, M. Rieth, J. Aktaa, T. Chikada, A. Hoffmann, J. Hoffmann, A. Houben, H. Kurishita, X. Jin, M. Li, A. Litnovsky, S. Matsuo, A. von Müller, V. Nikolic, T. Palacios, R. Pippan, D. Qu, J. Reiser, J. Riesch, T. Shikama, R. Stieglitz, T. Weber, S. Wurster, J.-H. You, and Z. Zhou. Development of advanced high heat flux and plasma-facing materials. *Nuclear Fusion*, 57(9):092007, 2017.

[57] K. Ikeda. Progress in the ITER physics basis. *Nuclear Fusion*, 47(6):E01, 2007.

[58] A. W. Leonard. Edge-localized-modes in tokamaks. *Physics of Plasmas*, 21(9):090501, 2014.

[59] J. W. Coenen, G. F. Matthews, K. Krieger, D. Iglesias, P. Bunting, Y. Corre, S. Silburn, I. Balboa, B. Bazylev, N. Conway, I. Coffey, R. Dejarnac, E. Gauthier, J. Gaspar, S. Jachmich, I. Jepu, C. Makepeace, R. Scannell, M. Stamp, P. Petersson, R. A. Pitts, S. Wiesen, A. Widdowson, K. Heinola, A. Baron-Wiechec, and JET Contributors. Transient induced tungsten melting at the joint european torus (JET). *Physica Scripta*, 2017(T170):014013, 2017.

[60] D. L. Rudakov, C. P. C. Wong, A. Litnovsky, W. R. Wampler, J. A. Boedo, N. H. Brooks, M. E. Fenstermacher, M. Groth, E. M. Hollmann, W. Jacob, S. I. Krasheninnikov, K. Krieger, C. J. Lasnier, A. W. Leonard, A. G. McLean, M. Marot, R. A. Moyer, T. W. Petrie, V. Philipps, R. D. Smirnov, P. C. Stangeby, J. G. Watkins, W. P. West, and J. H. Yu. Overview of the recent DiMES and MiMES experiments in DIII-D. *Physica Scripta*, 2009(T138):014007, 2009.

[61] D.L. Rudakov, T. Abrams, R. Ding, H.Y. Guo, P.C. Stangeby, W.R. Wampler, J.A. Boedo, A. Briesemeister, J.N. Brooks, D.A. Buchenauer, I. Bykov, C. Chrobak, R.P. Doerner, D. Donovan, J.D. Elder, M.E. Fenstermacher, J. Guterl, E. Hinson, E.M. Hollmann, C.J. Lasnier, A.W. Leonard, A.G. McLean, R.A. Moyer, R.E. Nygren, D.M. Thomas, E.A. Unterberg, J.G. Watkins, and C.P.C. Wong. DiMES PMI research at DIII-D in support of ITER and beyond. *Fusion Engineering and Design*, 124:196–201, 2017. Proceedings of the 29th Symposium on Fusion Technology (SOFT-29) Prague, Czech Republic, September 5-9, 2016.

[62] Ch. Linsmeier, B. Unterberg, J.W. Coenen, R.P. Doerner, H. Greuner, A. Kreter, J. Linke, and H. Maier. Material testing facilities and programs for plasma-facing component testing. *Nuclear Fusion*, 57(9):092012, 2017.

[63] A. Kreter, C. Brandt, A. Huber, S. Kraus, S. MÖller, M. Reinhart, B. Schweer, G. Sergienko, and B. Unterberg. Linear plasma device psi-2 for plasma-material interaction studies. *Fusion Science and Technology*, 68(1):8–14, 2015.

[64] H.J.N. van Eck, G.R.A. Akkermans, S. Alonso van der Westen, D.U.B. Aussems, M. van Berkel, S. Brons, I.G.J. Classen, H.J. van der Meiden, T.W. Morgan, M.J. van de Pol, J. Scholten, J.W.M. Vernimmen, E.G.P. Vos, and M.R. de Baar. High-fluence and high-flux performance characteristics of the superconducting magnum-psi linear plasma facility. *Fusion Engineering and Design*, 142:26–32, 2019.

[65] B. Unterberg, R. Jaspers, R. Koch, V. Massaut, J. Rapp, D. Reiter, S. Kraus, A. Kreter, V. Philipps, H. Reimer, U. Samm, L. Scheibl, B. Schweer, J. Schuurmans, I. Uytdenhouwen, R. Al, M.A. van den Berg, S. Brons, H.J.N. van Eck, W.J. Goedheer, M.F. Graswinckel, T. van der Grift, A. Kleyn, W.R. Koppers, O. Kruyt, A. Lof, H.J. van der Meiden, W. Melissen, M. van de Pol, G.J. van Rooij, P. Smeets, J. Scholten, D.C. Schram, G. De Temmerman, W. Vijvers, P.A. Zeijlmans van Emmichoven, and J.J. Zielinski. New linear plasma devices in the trilateral euregio cluster for an integrated approach to plasma surface interactions in fusion reactors. *Fusion Engineering and Design*, 86(9):1797–1800, 2011. Proceedings of the 26th Symposium of Fusion Technology (SOFT-26).

[66] M. C. Thompson, S. C. Simpson, C. J. Beers, J. Dadras, E. T. Meier, and P. H. Stoltz. Electrode durability and sheared-flow-stabilized Z-pinch fusion energy. *Physics of Plasmas*, 30(10):100601, 2023.

[67] C. W. Kimblin. Cathode spot erosion and ionization phenomena in the transition from vacuum to atmospheric pressure arcs. *Journal of Applied Physics*, 45(12):5235–5244, 1974.

[68] Gudrun Sævarsdóttir, Halldor Pálsson, Magnus Jónsson, and Jon Arne Bakken. Electrode erosion due to high-current electric arcs in silicon and ferrosilicon furnaces. *Steel Research International*, 77(6):385–391, 2006.

[69] *The London, Edinburgh and Dublin philosophical magazine and journal of science*, volume ser.4:v.6 (1853:July-Dec.), page 456. London, Taylor Francis, [1840-1944], 1853. https://www.biodiversitylibrary.org/bibliography/58679.

[70] Ralph Howard Fowler and L. Nordheim. Electron emission in intense electric fields. *Proceedings of the Royal Society of London. Series A, Containing Papers of a Mathematical and Physical Character*, 119(781):173–181, 1928.

[71] Irving Langmuir. The effect of space charge and initial velocities on the potential distribution and thermionic current between parallel plane electrodes. *Physical Review*, 21:419–435, 1923.

[72] Eleanor G. Forbes. *Diagnostic development and plasma-material interaction studies on the ZaP-HD device*. PhD thesis, University of Washington, 2020.

[73] R. P. Golingo and U. Shumlak. Spatial deconvolution technique to obtain velocity profiles from chord integrated spectra. *Review of Scientific Instruments*, 74(4):2332–2337, 2003.

[74] E. G. Forbes and U. Shumlak. Spatio-temporal ion temperature and velocity measurements in a z pinch using fast-framing spectroscopy. *Review of Scientific Instruments*, 91(8):083104, 2020.

[75] I. H. Hutchinson. Principles of plasma diagnostics: Second edition. *Plasma Physics and Controlled Fusion*, 44(12):2603–2603, 2002.

[76] D. J. Den Hartog and R. P. Golingo. Telecentric viewing system for light collection from a z-pinch plasma. *Review of Scientific Instruments*, 72(4):2224–2225, 2001.

[77] S. L. Jackson and U. Shumlak. Abel inversion of a holographic interferogram for determination of the density profile of a sheared-flow z pinch. *Review of Scientific Instruments*, 77(8):083502, 2006.

[78] Sean D. Knecht, Raymond P. Golingo, Brian A. Nelson, and Uri Shumlak. Calculation of the equilibrium evolution of the zap flow z -pinch using a four-chord interferometer. *IEEE Transactions on Plasma Science*, 43(8):2469–2479, 2015.

[79] Raymond P. Golingo. *Formation of a sheared flow Z-pinch.* PhD thesis, University of Washington, 2003.

[80] Amierul Aqil bin Khairi. Graphite electrode characterization on the ZaP-HD sheared-flow-stabilized z-pinch device. Master's thesis, University of Washington, 2021.

[81] C. De Michelis and M. Mattioli. Spectroscopy and impurity behaviour in fusion plasmas. *Reports on Progress in Physics*, 47(10):1233, 1984.

[82] P. D. Morgan, K. H. Behringer, P. G. Carolan, M. J. Forrest, N. J. Peacock, and M. F. Stamp. Spectroscopic measurements on the joint european torus using optical fibers to relay visible radiation. *Review of Scientific Instruments*, 56(5):862–864, 1985.

[83] K. Behringer. Spectroscopic diagnostics on JET (invited). *Review of Scientific Instruments*, 57(8):2000–2005, 1986.

[84] E. Hintz and P. Bogen. Plasma edge diagnostics by optical methods. *Journal of Nuclear Materials*, 128-129:229–239, 1984.

[85] G. Fussmann, U. Ditte, W. Eckstein, T. Grave, M. Keilhacker, K. McCormick, H. Murmann, H. Röhr, M. Elshaer, K.-H. Steuer, Z. Szymanski, F. Wagner, G. Becker, K. Bernhardi, A. Eberhagen, O. Gehre, J. Gernhardt, G.V. Gierke, E. Glock, O. Gruber, G. Haas, M. Hesse, G. Janeschitz, F. Karger, S. Kissel, O. Klüber, M. Kornherr, G. Lisitano, H.M. Mayer, D. Meisel, E.R. Müller, W. Poschenrieder, F. Ryter, H. Rapp, F. Schneider, G. Siller, P. Smeulders, F. Söldner, E. Speth, A. Stäbler, and O. Vollmer. Divertor parameters and divertor operation in asdex. *Journal of Nuclear Materials*, 128-129:350–358, 1984.

[86] T. Abrams, S. Bringuier, D.M. Thomas, G. Sinclair, S. Gonderman, L. Holland, D.L. Rudakov, R.S. Wilcox, E.A. Unterberg, and F. Scotti. Evaluation of silicon carbide as a divertor armor material in DIII-D H-mode discharges. *Nuclear Fusion*, 61(6):066005, 2021.

[87] A. N. James, D. Brunner, B. Labombard, C. Lau, B. Lipschultz, D. Miller, M. L. Reinke, J. L. Terry, C. Theiler, G. M. Wallace, D. G. Whyte, S. Wukitch, and V. Soukhanovskii. Imaging of molybdenum erosion and thermography at visible wavelengths in Alcator C-Mod ICRH and LHCD discharges. *Plasma Physics and Controlled Fusion*, 55(12):125010, 2013.

[88] P. Bogen and E. Hintz. *Plasma Edge Diagnostics Using Optical Methods*, pages 211–280. Springer US, Boston, MA, 1986.

[89] K Behringer, H P Summers, B Denne, M Forrest, and M Stamp. Spectroscopic determination of impurity influx from localized surfaces. *Plasma Physics and Controlled Fusion*, 31(14):2059–2099, 1989.

[90] D. J. Den Hartog and R. P. Golingo. Telecentric viewing system for light collection from a z-pinch plasma. *Review of Scientific Instruments*, 72(4):2224–2225, 2001.

[91] H. P. Summers and M. G. O'Mullane. Atomic Data and Modelling for Fusion: the ADAS Project. *AIP Conference Proceedings*, 1344(1):179–187, 2011.

[92] J. Abrahamson. Graphite sublimation temperatures, carbon arcs and crystallite erosion. *Carbon*, 12(2):111–141, 1974.

[93] B. Müller and U. Renz. Development of a fast fiber-optic two-color pyrometer for the temperature measurement of surfaces with varying emissivities. *Review of Scientific Instruments*, 72(8):3366–3374, 2001.

[94] P. B. Coates. Multi-wavelength pyrometry. *Metrologia*, 17(3):103, 1981.

[95] R. J. Thorn and O. C. Simpson. Spectral emissivities of graphite and carbon. *Journal of Applied Physics*, 24(5):633–639, 1953.

[96] Yuzhong Zhang, Fucheng Lu, Tao Deng, Shuangbao Shu, Yan Zhang, Tengda Zhang, and Xianli Lang. Normal spectral emissivity measurement of graphite in the temperature range between 200°c and 500°c. *Fusion Engineering and Design*, 175:112998, 2022.

[97] Entegris. Typical properties of industrial graphite grades. Available at `https://poco.entegris.com/en/home/products/premium-graphite/industrial-grades/axf5q.html` (2025/10/3).

[98] W.E. Dasent. *Inorganic Energetics: An Introduction*. Cambridge Texts in Chemistry and Biochemistry. Cambridge University Press, 1982.

[99] Valerian Nemchinsky. Erosion of thermionic cathodes in welding and plasma arc cutting systems. *IEEE Transactions on Plasma Science*, 42(1):199–215, 2014.

[100] A. A. Bogomaz, A. V. Budin, V. A. Kolikov, M. É. Pinchuk, A. A. Pozubenkov, and Ph. G. Rutberg. Features of the electrode erosion for discharge-current amplitudes above 105 A. *Doklady Physics*, 48(1):1–4, 2003.

[101] MirMohammadreza Seyedhabashi, Maryam Ebrahimi, Ehsanollah Noori, and Mehdi Janbazi. Investigating graphite surface and structural modifications induced by hydrogen ion bombardment in a plasma focus device. *Results in Materials*, 26:100698, 2025.

[102] E. Oyarzabal, R. P. Doerner, M. Shimada, and G. R. Tynan. Carbon atom and cluster sputtering under low-energy noble gas plasma bombardment. *Journal of Applied Physics*, 104(4):043305, 2008.

[103] J. Ng and Y. Raitses. Role of the cathode deposit in the carbon arc for the synthesis of nanomaterials. *Carbon*, 77:80–88, 2014.

[104] Francis P. Bundy. The P, T phase and reaction diagram for elemental carbon, 1979. *Journal of Geophysical Research: Solid Earth*, 85(B12):6930–6936, 1980.

[105] L. B. Gordon, M. Kristiansen, M. O. Hagler, H. C. Kirbie, R. M. Ness, L. L. Hatfield, and J. N. Marx. Material studies in a high energy spark gap. *IEEE Transactions on Plasma Science*, 10(4):286–293, 1982.

[106] Elliott A. Eklund, R. Bruinsma, J. Rudnick, and R. Stanley Williams. Submicron-scale surface roughening induced by ion bombardment. *Physical Review Letters*, 67:1759–1762, 1991.

[107] Johann Peter Mogeritsch, Robert Franz, Mehran Golizadeh, Christian Mitterer, and Abdellah Kharicha. Determination of cooling rate and temperature gradient during formation of cathode spot craters in a vacuum arc. *Crystals*, 12(10), 2022.

[108] G. Alberti, M. Sala, J. Romazanov, A. Uccello, D. Dellasega, and M. Passoni. ERO2.0 modelling of nanoscale surface morphology evolution. *Nuclear Fusion*, 61(6):066039, 2021.

[109] G. D. Hobbs and J. A. Wesson. Heat flow through a langmuir sheath in the presence of electron emission. *Plasma Physics*, 9(1):85, 1967.

[110] T. Abrams, E. A. Unterberg, D. L. Rudakov, A. W. Leonard, O. Schmitz, D. Shiraki, L. R. Baylor, P. C. Stangeby, D. M. Thomas, and H. Q. Wang. Impact of ELM control techniques on tungsten sputtering in the DIII-D divertor and extrapolations to ITER. *Physics of Plasmas*, 26(6):062504, 2019.

[111] Amierul Aqil Khairi, Elyse Lian, and Uri Shumlak. Spectroscopic measurements of graphite electrode erosion on the ZaP-HD sheared-flow-stabilized z-pinch device. Manuscript submitted for publication, available on arXiv: `https://doi.org/10.48550/arXiv.2510.03414`, 2025.

[112] Amierul Aqil Khairi and Uri Shumlak. Experimental investigation of plasma-electrode interactions on the ZaP-HD sheared-flow-stabilized z-pinch device. Manuscript submitted for publication, available on arXiv: `https://doi.org/10.48550/arXiv.2511.00354`, 2025.

VITA

Amierul Aqil bin Khairi was born in Kuala Lumpur, Malaysia in 1996. Part of a diplomatic family, he also spent formative years in Washington, D.C. and Ho Chi Minh City, Vietnam, and later summers in Havana, Cuba. His childhood travels and an early love of science fiction led to an interest in human space exploration, and an emphasis on STEM coursework while attending high school at the International School of Kuala Lumpur. After graduating in 2015, he moved to Seattle to begin his degree in Aeronautical and Astronautical Engineering at the University of Washington. Much of his time as an undergraduate was spent with the Society for Advanced Rocket Propulsion (SARP) student rocketry group, eventually leading the thermal protection and combustion chamber teams. In 2018, he joined the ZaP Flow Z-Pinch Lab in the Aerospace and Energetics Research Program as a rising senior. In 2019, he earned a Bachelor of Science and was part of the SARP team that won the Spaceport America Cup. He continued with the ZaP lab in graduate school, working initially on the FuZE device and subsequently on ZaP-HD. He earned a Master of Science in 2021, and a Doctor of Philosophy from the William E. Boeing Department of Aeronautics & Astronautics in 2025.